



Universidade de Brasília

Instituto de Geociências

A raiz do Sistema IOCG de Carajás: alterações hidrotermais e mineralização niquelífera neoarqueana no depósito GT-34

Dissertação de Mestrado Nº 406

Victor Botelho Perez Garcia

Brasília – DF, 2018



Universidade de Brasília

Instituto de Geociências

A raiz do Sistema IOCG de Carajás: alterações hidrotermais e mineralização niquelífera neoarqueana no depósito GT-34

Dissertação de Mestrado

Victor Botelho Perez Garcia

Área de Concentração: Prospecção e Geologia Econômica

Banca Examinadora:

Maria Emília Schutesky Della Giustina (Orientadora)

Roberto Ventura Santos (UnB)

Lena Viginia Soares Monteiro (USP)

Nilson Francisquini Botelho (UnB/Suplente)

Brasília, 2018

"If at first the idea is not absurd, then there is no hope for it."

-Albert Einstein

AGRADECIMENTOS

Gostaria, em primeiro lugar, de agradecer aos leitores desse trabalho: obrigado por disporem seu tempo para ler as divagações das páginas seguintes.

Agradeço aos meus pais, Eurico e Alice, e irmãos, Fernando e Igor, por, mesmo sem acreditar que mestrado seja um trabalho de verdade, me apoiaram e me questionaram quando necessário.

Agradeço a senhora Emilia Nazaré Della Giustina pela incrível oportunidade de participar de seus projetos, pelas conversas, piadas e pela liberdade que me foi dada. Você é muito mais que uma simples orientadora! Também sou grato ao professor Claudinei pelas ideias, conversas, críticas e incentivos.

Agradeço também a minha parceira Crau Tharis Augustin por suportar grande parte das minhas ideias e conversas, se irritando apenas um pouco mais que o necessário.

Também sou grato aos meus amigos extra-geologia (Gaucho, Fabão, Japa, Índio etc), que mesmo sem saber o que é um quartzo, forneceram a distração necessária para manter meus pés no chão e preservar o que ainda resta da minha sanidade.

Agradeço também aos meus amigos e colegas geólogos que de alguma forma contribuíram para o desenvolvimento desse trabalho, em especial aos trabalhadores áridos da microsonda que possibilitaram que o esqueleto desse trabalho fosse construído.

Muito obrigado, sem vocês esse trabalho não existiria.

RESUMO

O depósito GT-34, localizado a 12 km a SW da mina Sequerinho, Carajás, norte do Brasil, representa uma ocorrência incomum de Ni relacionado ao sistema *Iron-Oxide-Copper-Gold* (IOCG) regional. Ocorre ao longo de uma zona de cisalhamento subvertical de orientação NE-SW marcado por zonas de alteração alcáli-Fe encaixado em granitos a tonalitos. A alteração inicial Na-Mg e alteração Ca pervasiva formam, respectivamente, marialite-ortopiroxênio e hornblenda-plagioclásio-clinopiroxênio. A mineralização de Ni ocorre na forma de brechas com a matriz rica em pentlandita-pirrotita-apatita e fragmentos arredondados compostos predominantemente por fragmentos da alteração Ca. Veios tardios de alteração K-Fe com magnetita ou hematita (alteração K-Fe (Mt) e alteração K-Fe (Hem), respectivamente) remobilizam parcialmente a mineralização, reprecipitando-a como calcopirita-pirrotita-magnetita (alteração K-Fe (Mt)) e como milerita-pirita-apatita (alteração K-Fe (Hem)). A alteração K-Fe (Mt) ocorre como veios irregulares ricos em flogopita-talco, enquanto a alteração K-Fe (Hem) ocorre como veios bem delimitados com K-feldspato-albita-quartzo-clorita-calcita-epidoto. As características iniciais do fluido associado a alteração Na-Mg precisam ser anidras para a estabilização do ortopiroxênio e de elevada salinidade para formação da marialita. Um fluido imiscível composto por CO₂-NaCl é sugerido para a atingir tais características. A presença do ortopiroxênio indica temperaturas >700°C. Estudos experimentais indicam que marialita não se forma a partir de fluidos ricos em NaCl a pressões >7 kbar a temperatura >700°C. A ausência de quartzo pode ocorrer devido a sua dissolução causada por fluidos ricos em NaCl sob pressões >5 kbar e temperaturas similares, também determinado experimentalmente. Cristais de zircão foram recuperados da alteração Na-Mg inicial e da alteração tardia K-Fe (Mt) fornecendo uma idade concordante de 2.724±4 Ga, corroborando a formação Neoarqueana do depósito GT-34, similar aos demais depósitos IOCG em Carajás. A temperatura >700°C e pressão entre 5–7 kbar, eventuais fluidos evaporíticos não podem estar presentes, sendo necessário uma fonte magmática. As idades obtidas nesse estudo se sobrepõe a idade do magmatismo bimodal Neoarqueano (2.75-2.70 Ga), suportando uma origem magmática-hidrotermal. As condições determinadas para o depósito GT-34 elevam a temperatura inicial do sistema IOCG de Carajás em pelo menos 200°C com pressões podendo chegar até 7 kbar, tornando-o a mais profunda ocorrência associada ao sistema IOCG de Carajás conhecida até então.

Palavra-chave: Iron-Oxide-Copper-Gold (IOCG), Carajás, Neoarqueano, Ortopiroxênio

ABSTRACT

The GT-34 deposit, which is located 12 km SW of the Sequerinho copper-gold mine, Carajás Province, northern Brazil, represents an unusual Ni occurrence related to a regional Iron-Oxide-Copper-Gold (IOCG) system. It occurs along a NE-SW-trending sub-vertical shear zone marked by progressive alkali-Fe alteration zones hosted in tonalite to granite intrusions. Initial Na-Mg and pervasive Ca alteration forms the unique marialite-orthopyroxene and hornblende-plagioclase-clinopyroxene associations, respectively. Nickel mineralization occurs as breccias in a pentlandite-pyrrhotite-apatite-rich matrix with rounded fragments chiefly of Ca-alteration parageneses. Late-stage veins of K-Fe magnetite and hematite (K-Fe (Mt) and K-Fe (Hem)) alterations partially remobilize the mineralization, reprecipitating as chalcopyrite-pyrrhotite-magnetite and millerite-pyrite-apatite, respectively. Potassium-Fe (Mt) occurs as irregular phlogopite-talc-rich veins, while K-Fe (Hem) occurs as sharp K-feldspar-albite-quartz-chlorite-calcite-epidote veins. Initial fluid characteristics associated with Na-Mg alteration require anhydrous conditions for orthopyroxene stability and high salinity for marialite formation. An immiscible CO₂-NaCl fluid is therefore associated with such conditions. The presence of orthopyroxene indicates temperatures >700°C. Experimental studies indicate that marialite does not form with NaCl-rich fluid at pressures >7 kbar under such temperatures. The absence of quartz might be caused by NaCl dissolution at pressures >5 kbar, as determined experimentally with the same temperature conditions. Zircon crystals were recovered from the initial Na-Mg alteration and late-stage K-Fe (Mt) alteration yielding a concordant 2.724±4 Ga age, corroborating the GT-34 Neoproterozoic formation similar to other IOCG deposits in Carajás. At >700°C and 5–7 kbar, an eventual evaporitic fluid source would not be present, making a magmatic fluid source necessary. The age constrains obtained in this study overlaps the bimodal Neoproterozoic magmatism (2.75–2.70 Ga), supporting a magmatic-hydrothermal origin. Determination of such conditions raises the initial temperature of the Carajás IOCG system at least 200°C and pressure up to 7 kbar, making GT-34 the deepest IOCG-related occurrence known to date for this province.

Key words: Iron-Oxide-Copper-Gold (IOCG); Carajás, Neoproterozoic, Orthopyroxene

Sumário

AGRADECIMENTOS.....	i
RESUMO	ii
ABSTRACT	iii
Capítulo 1: <i>Introdução</i>	1
1.1 Estrutura da dissertação.....	1
1.2 Justificativa e Objetivo	1
1.3 Localização da área de estudo.....	2
Capítulo 2: <i>Contextos geológicos</i>	3
2.1 Depósitos do tipo IOCG-IOA.....	3
2.2 Geologia Regional do Domínio Carajás	6
2.2.1 Sistema mineralizante Óxido de Fe-Cu-Au-Polímetais em Carajás	10
Capítulo 3: <i>The Ni-rich GT-34 deposit: A view into the deep alteration zones of the Carajás Neoproterozoic IOCG system, Brazil</i>	14
3.1 Abstract.....	14
3.2 Introduction.....	14
3.3 Carajás Regional Geology	16
3.4 Carajás IOCG deposits.....	17
3.5 GT-34 deposit	17
3.5.1 Host Rocks	19
3.5.2 Na-Mg alteration	19
3.5.3 Ca alteration	22
3.5.4 Ni mineralization.....	23
3.5.5 K-Fe (Mt) alteration and first sulfide remobilization	24
3.5.6 K-Fe (Hem) alteration and second sulfide remobilization.....	26
3.6 Mineral Chemistry	28
3.7 Geochronology.....	32
3.8 Discussion.....	34
3.8.1 Orthopyroxene formation.....	34
3.8.2 Proximal charnockites	36
3.8.3 Different amphibole-bearing alterations.....	37
3.8.4 Fluid source.....	38
3.8.5 GT-34 and the IOCG system.....	Erro! Indicador não definido.
3.9 Conclusions	39
3.10 Acknowledgements.....	40
3.11 Reference.....	40

Capítulo 4: Conclusão	45
Referências	46
ANEXO I – supplementary EPMA analyses.	51
ANEXO II– supplementary U-Pb analyses.	78

Capítulo 1: *Introdução*

1.1 Estrutura da dissertação

Esta dissertação foi organizada em quatro capítulos. São eles respectivamente: *Introdução*, *Contextos Geológicos*, “*The Ni-rich GT-34 deposit: A view into the deep alteration zones of the Carajás Neoproterozoic IOCG system, Brazil*” e *Conclusões*. Referências e Anexo se encontram ao final do volume. O capítulo inicial aborda os aspectos gerais sobre a dissertação, como sua estrutura, justificativa, objetivo e localização da área de estudo. O segundo capítulo aborda os contextos geológicos no qual o trabalho está inserido, considerando o atual histórico do sistema mineralizante IOCG na literatura. No mesmo capítulo também é descrita a geologia regional do Domínio Carajás, assim como os depósitos do sistema IOCG atualmente conhecidos para esse domínio. O terceiro capítulo está exposto o artigo elaborado para obtenção do grau de mestre, a ser submetido para periódico internacional. O quarto capítulo apresenta as conclusões atingidas com esse trabalho. As referências estão disponíveis ao final do volume. O anexo contém os dados de EPMA e Geocronologia obtidos durante esse estudo.

1.2 Justificativa e Objetivo

O Domínio Carajás é mundialmente conhecido pela maior concentração de alta tonelagem de depósitos do sistema IOCG, sendo os únicos representantes de idade arqueana (Hitzman 2000; Groves et al. 2010; Xavier et al. 2012). Destacam-se os depósitos Salobo, Sossego-Sequeirinho, Cristalino, Igarapé-Bahia e Alvo 118 além de uma série de depósitos satélites associados.

Recentemente, foi reconhecido que associado ao sistema IOCG podem ocorrer uma série de depósitos polimetálicos, além da clássica associação com Cu e Au (Corriveau et al. 2016). Metais, tais como Ni, Co, U, REE, Pd, Ag, Zn, V, Th e outros podem aparecer associados ao sistema IOCG, revelando a complexidade desse sistema. Ligado ao sistema IOCG observam uma série de características que definem esse sistema tais como as alterações hidrotermais álcali-férricas, o forte controle estrutural e a presença de óxido de Fe.

Com os avanços recentes nos estudos sobre o sistema IOCG no Domínio Carajás, foi possível aprimorar o conhecimento e a compreensão desse sistema (Moreto et al. 2015a, 2015b; Xavier et al. 2017; Giustina et al. comunicação pessoal). Uma sucessão de

estágios de alteração hidrotermal é observada, progredindo de Na, Na-Ca, K, Chl-Cc e silicificação (Monteiro et al. 2008a). A fonte dos fluidos mineralizantes é considerada mista, derivada de um sistema magmático hidrotermal e de fluidos superficiais, evidentes principalmente a partir de dados isotópicos.

Motivado pelo contexto atual, o depósito GT-34, situado na porção sul do Domínio Carajás, representa uma ocorrência de Ni considerada inicialmente como parte do sistema IOCG de Carajás (Siepierski 2008). A característica polimetálica do sistema IOCG (Corriveau et al. 2016) é realçada nesse depósito, o que permite um estudo de caso que contribua para compreensão desse sistema.

Dessa forma, esse projeto visa compreender e caracterizar as alterações hidrotermais e mineralização do depósito GT-34 com base no atual conceito do sistema IOCG. Para isso, foram realizados estudos petrográficos, química mineral e geocronologia U-Pb. O intuito desse trabalho é contribuir com novos dados e auxiliar no entendimento do sistema IOCG.

1.3 Localização da área de estudo

A área estudada está localizada na região norte do Brasil, na porção sudeste do estado do Pará. O alvo estudado insere-se dentro de um raio de 12 km ao redor da mina do Sossego (Figure 1.1). A cidade mais próxima é Canaã dos Carajás, distante cerca de 25 km em linha reta da mina Sossego. O acesso a região é feito através de estradas pavimentadas com afloramentos escassos devido a extensa cobertura de solo.

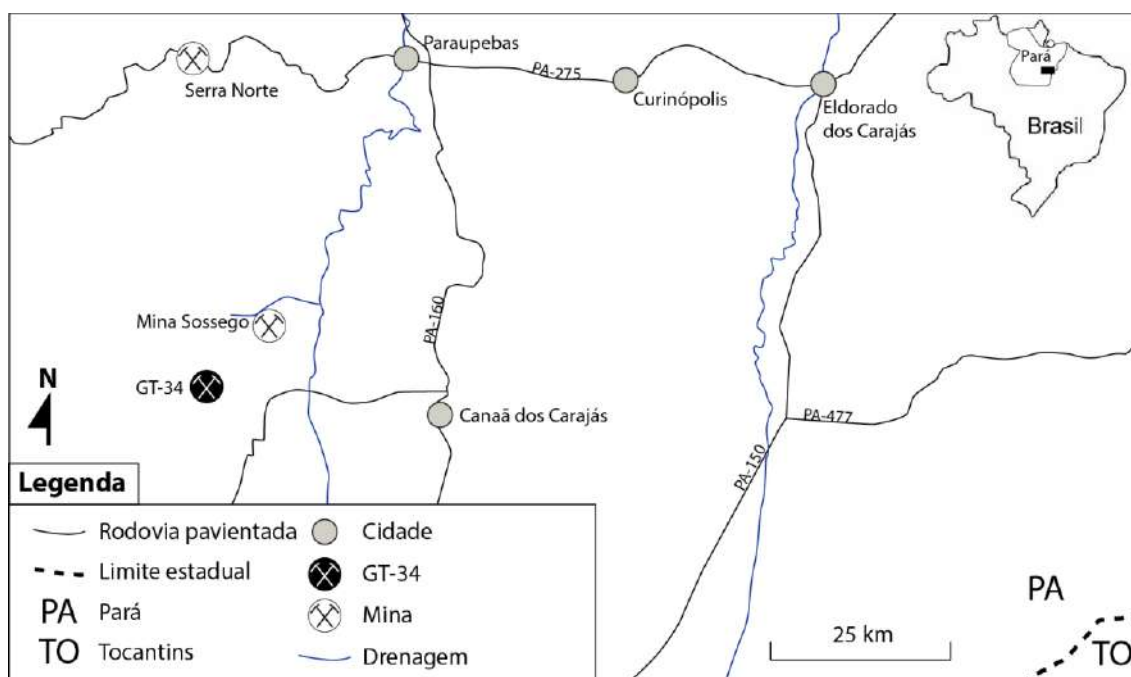


Figure 1.1 Localização do depósito GT-34 e principais vias de acesso.

Capítulo 2: *Contextos geológicos*

2.1 Depósitos do tipo IOCG-IOA

Depósitos ricos em óxido de ferro, cobre, ouro e metais associados são conhecidos e explorados a séculos. Contudo, suas características principais só foram definidas no final dos anos 80 e início dos anos 90 (Meyer 1988; Hauck 1990; Hitzman et al. 1992) baseado principalmente em depósitos proterozóicos. Os estudos foram feitos em regiões como Olympic Dam (Austrália, Robert e Hudson 1983), Kiruna (Suécia, Parak 1985) e Missouri (Estados Unidos da América, Panno e Hood 1983)

Hitzman et al. (1992) observou as principais características dessa classe distinta de depósito, denominando-as de óxido de ferro cobre-ouro. Tipicamente, apresentam rochas ricas em óxido de ferro com baixo conteúdo de titânio, constituídos por hematita em níveis mais rasos e magnetita e níveis mais profundos. A mineralização ocorre ao longo de zonas de falha na forma de brechas hidrotermais, e está associada a ambientes predominantemente extensionais.

Uma alteração hidrotermal pervasiva é marcante em todos depósitos estudados. Alteração sódica é associada a níveis mais profundos, seguida por alteração potássica em níveis intermediários (Hitzman et al. 1992). O desenvolvimento de alteração sericítica/silicificação só foi observada em níveis mais rasos. Os fluidos associados com as alterações hidrotermais e mineralização geralmente apresentam elevada salinidade.

O uso da abreviação IOCG (iron oxide copper gold), assim como IOA (iron oxide apatite), só foram introduzidas nos anos 2000 (Porter 2000). A abreviação foi feita usando os três principais metais desse sistema: Ferro (óxido de ferro), Cobre e Ouro. Desde então, os depósitos dessa classe são referidos como IOCG.

Apesar das características empíricas inicialmente definidas, a definição do processo geológico gerador desses depósitos ainda é amplamente discutida nos dias atuais sem apresentar consenso na literatura. Inicialmente, fluidos de origem predominantemente magmática hidrotermal (Figure 2.1) foram descritos como possíveis geradores dessa classe de depósito (Hitzman et al. 1992). A sugestão de que fluidos magmáticos seriam responsáveis pela mineralização foi baseada no extensivo magmatismo ligado a ambientes extensionais em que grande parte dos depósitos está inserido.

Questionando a origem magmático hidrotermal dos fluidos, foi proposto (Barton and Johnson 1996) que a origem poderia ocorrer associado a águas superficiais e/ou conatas. As águas superficiais salinas, ligadas a evaporitos, circulariam transportando e depositando metais (Figure 2.1). O magmatismo seria uma fonte de calor que promoveria a circulação desses fluidos exercendo um papel secundário na formação desses depósitos.

De forma alternativa aos processos citados, foi também proposto uma origem metamórfica (Hunt et al. 2007) para a região de Wernecke, Canada. Especificamente para essa região, foi observado que a formação da mineralização ocorreu em ambiente compressivo. Evaporitos situados a baixo das rochas encaixantes forneceram a salinidade necessária para os fluidos gerados durante a compressão/metamorfismo formarem o depósito (Figure 2.1).

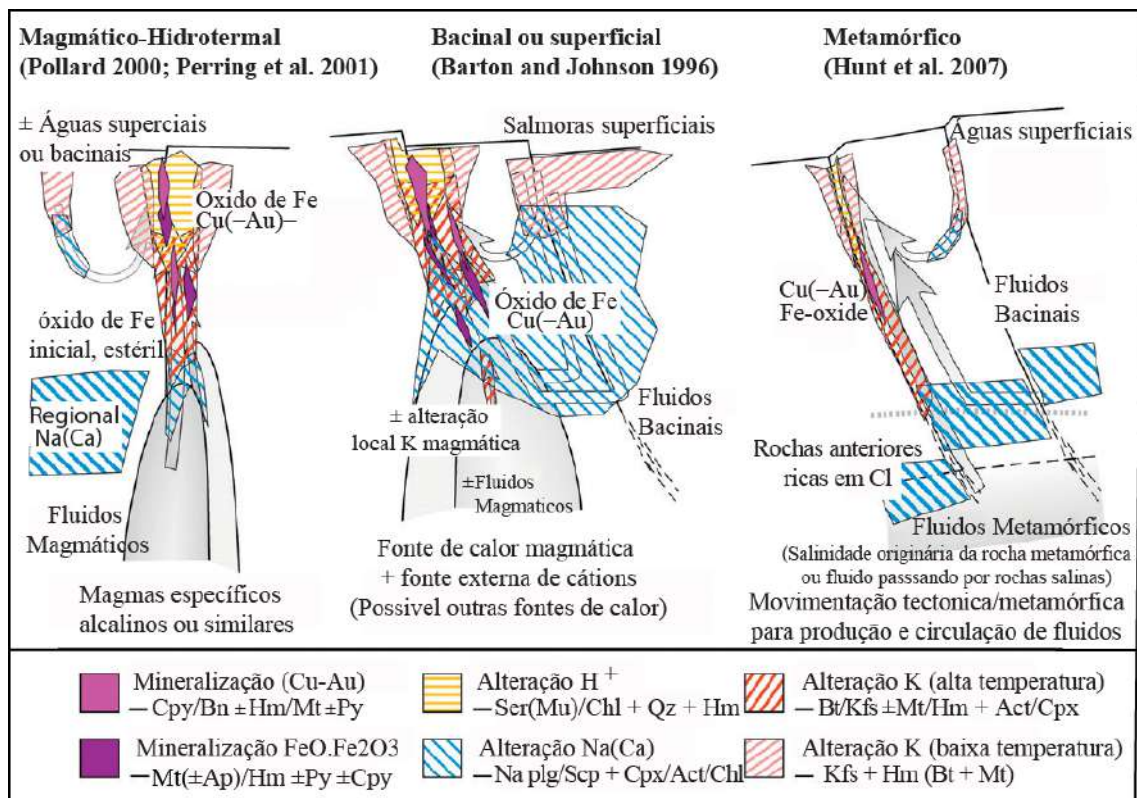


Figure 2.1 Principais modelos de formação para depósitos do tipo IOCG. Cpy= calcopirita. Bn= bornita. Hm = hematita. Mt= magnetita. Py = pirita. Ap= apatita. Ser= sericita. Chl= clorita. Qz = quartzo. Na plg = plagioclásio sódico. Scp = escapolita. Cpx = clinopiroxênio. Act = actinolita. Bt = biotita. Kfs= Felpato potássico. Modificado de Williams et al. 2005 e Barton 2014.

Além das três propostas anteriores, uma origem alternativa a partir de uma imiscibilidade magmática foi sugerida (Park 1961; Frutos e Oyarzun 1975). Essa proposta consiste de uma origem puramente magmática por meio de líquidos imiscíveis ricos em óxido de ferro e voláteis que seriam responsáveis pela mineralização.

Devido a série de processos geológicos possíveis para geração de depósitos do tipo IOCG, diversas subdivisões e reclassificações foram sugeridas (Williams et al. 2005; Hunt et al. 2007; Groves et al. 2010). Williams et al. (2005) propõe uma classificação empírica com base em cinco aspectos: (1) Presença de Cu e Au como metais econômicos; (2) Brechas hidrotermais controladas estruturalmente; (3) Óxido de Fe abundante; (4) Baixo conteúdo de Ti nos óxidos de Fe quando comparado aos de origem magmática; (5) Não apresentam relação clara com intrusões como no caso dos depósitos do tipo pórfiro.

Groves et al. (2010) sugere uma subdivisão em cinco subgrupos, sendo eles: (1) IOCG strictu sensu; (2) Óxido de Fe rico em P; (3) Depósitos carbonatito-óxido de Fe e elementos litófilos; (4) Cu-Au pórfiro e Fe-skarn; (5) Substituição de alto grau de magnetita Au-Cu. As propostas (Williams et al. 2005; Groves et al. 2010), no entanto, se baseiam em critérios que podem refletir um enfoque socioeconômico ao invés de processos geológicos (Barton 2014).

Hunt et al. (2007) propõe uma subdivisão em depósitos IOCG magmáticos, não magmáticos ou depósitos híbridos. Essa subdivisão é baseada na fonte de fluídos formadores dos depósitos, tema que atualmente ainda é amplamente discutido na literatura. Os metais associados também foram utilizados como distinção, porém devido a ampla variedade de metais presentes no sistema a classificação se tornou inefetiva.

Atualmente, os depósitos são reconhecidos pela ampla variedade de fatores que podem levar a sua formação. A individualização de zonas de alteração hidrotermais foi feita de forma sistemática aproveitando as exposições contínuas da região do *Great Bear Magmatic Zone* (Corriveau et al. 2016). As principais zonas individualizadas foram, respectivamente, sódica (Na) em zonas mais profundas e cálcica ferrosa de alta temperatura (HT Ca-Fe), ambas ocorrendo de forma pervasiva. De forma mais localizada ocorrem a potássica ferrosa de alta temperatura (HT K-Fe) e potássica férrica de baixa temperatura (LT K-Fe). Ressalta-se que nem sempre todas as zonas de alteração estão presentes e que apresentam domínios transicionais.

Associado às zonas de alteração hidrotermal, foi proposto um zoneamento de metais (Corriveau et al. 2017). Cobre aparece na forma de sulfetos tipicamente associado a alteração K tanto de alta quanto de baixa temperatura e em veios tardios. Níquel e Co estão presentes na forma de sulfetos associados a alteração cálcica de alta temperatura e também ligados a veios tardios. Sulfetos de Fe podem ser encontrados em todos os estágios exceto durante a alteração sódica. Chumbo e Zn aparecem apenas nos estágios mais tardios. Independente dos sulfetos, os metais podem ser encontrados como óxidos,

fosfatos ou na forma nativa. Ouro e prata podem estar associados e geralmente estão ligados as alterações potássicas e a veios tardios. Elementos Terras Raras aparecem tanto na alteração cálcica de alta temperatura, onde predominam os HREE, ou na alteração K de baixa temperatura, onde predominam os LREE. Urânio ocorre difundido ao longo de todas as alterações, aparecendo principalmente em zonas de alteração K.

Associado aos depósitos IOCG podem ocorrer os depósitos do tipo IOA (tipo Kiruna). Inicialmente, foi descrito (Hitzman et al. 1992) que ambos seriam parte de um contínuo onde os IOA representariam a zona mais profunda dos depósitos IOCG. Níveis ricos em magnetita apatita (IOA) podem também ser encontrados associados a alterações HT Ca-Fe dentro de um contínuo de evolução do sistema IOCG (Corriveau et al. 2016).

Contudo, depósitos do tipo IOA também podem ocorrer de forma independente do sistema IOCG, formados a poucos km de distância. Aparecem tipicamente como *pipes* de magnetita-apatita descritos como formados a partir de uma imiscibilidade magmática (Tornos et al 2016 e referências contidas) observados em lugares como Chile, México, Irã e China. Apresentam texturas típicas similares às encontradas em derrames basálticos como vesículas e tubos de degaseificação. Ademais, as porções ricas em magnetita não se restringem a zonas de alteração hidrotermal.

Por fim, pode-se concluir que depósitos da família IOCG-IOA apresentam diversas características distintas. A variedade de metais, alteração hidrotermal, idade e ambiente de formação é notória e deve ser levada em conta para cada região específica. Definir um modelo único baseado nas feições conhecidas não parece razoável pois, de forma separada, não se consegue abranger todos os processos geológicos que podem influenciar a origem desses depósitos. Assim, depósitos IOCG-IOA permanecem descritos por meio de características empíricas como inicialmente sugeridas (Hitzman et al. 1992), sem apresentar conotações genéticas associadas.

2.2 Geologia Regional do Domínio Carajás

O Domínio Carajás localiza-se na região norte do Brasil, na porção sudeste do Cráton Amazônico (Figure 2.2) e representa a porção norte da Província Carajás. Está limitado à norte pelo Domínio Bacajá, de idade paleoproterozóica (2,26-1,95 Ga); a leste pelo cinturão Araguaia, de idade neoproterozóica. A sul, o limite é marcado pelas rochas do Domínio Rio Maria, onde prevalecem idades Mesoarqueanas (3,0 – 2,86 Ga); a oeste pelas coberturas vulcânicas-plutônicas do Domínio Paleoproterozoico do Iriri-Xingu (Santos 2003; Vasquez et al. 2008). O Domínio Carajás é marcado pelo formato sigmoidal

marcado por estruturas leste-oeste e oeste-noroeste – leste-sudeste observados nas falhas Cinzento, Carajás e Canaã (Figure 2.2).

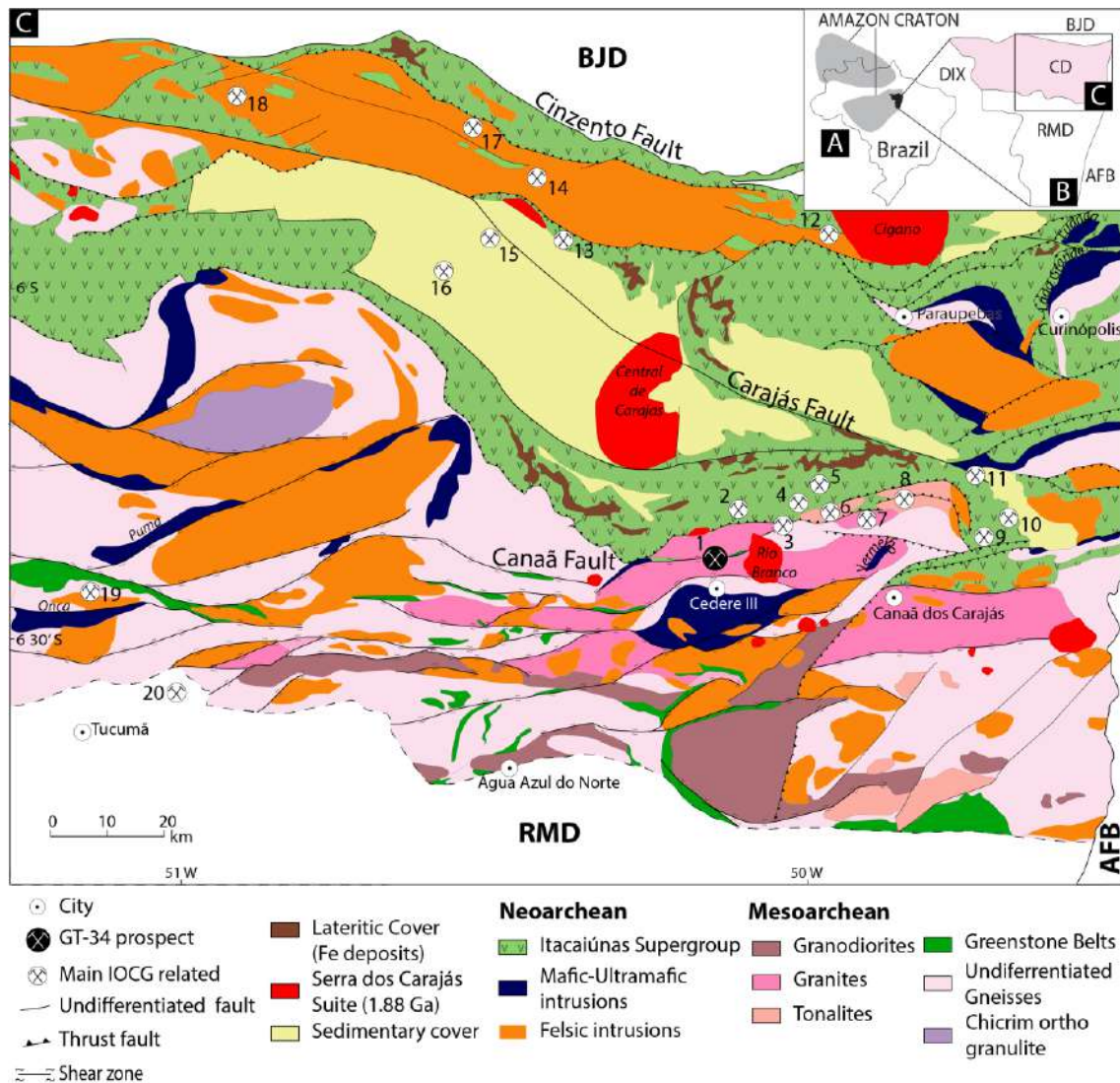


Figure 2.2 Mapa geológico do Domínio Carajás. A- Localização do Domínio Carajás relativo ao Cráton Amazônico. B- Limites do Domínio Carajás evidenciando os diferentes domínios tectônicos individualizados. C- Principais litologias e estruturas encontradas no Domínio Carajás. Os principais depósitos IOCG encontram-se numerados de 1 a 20: 1 – GT-34; 2 – Alvo 118; 3 – Sossego-Sequerinho; 4 – Jatobá; 5 – Castanha; 6 – Bacaba; 7 – Visconde; 8 – Bacurí; 9 – Borrachudos; 10 – Cristalino; 11 – Estrela; 12 – Furnas; 13 – Gameleira; 14 – Paulo Afonso; 15 – Pojuca; 16 – Igarapé Bahia/Alemão; 17 – Salobo; 18 – Igarapé Cinzento/GT-46; 19 – Jaguar; 20 – Pantera. RMD – Rio Maria Domain; AFB – Araguaia Fold Belt; BJD – Bacajá Domain; DIX – Domain Iriri-Xingu. Modified from Costa et al. (2016).

O Domínio Carajás contém as principais mineralizações do tipo IOCG até então conhecidas para região (exceto o depósito Pantera, situado no Domínio Rio Maria), que ocorrem tanto em rochas do embasamento quanto em rochas supracrustais. O embasamento é representado por rochas Mesoarqueanas do Complexo Xingu formados por trondjhemito-tonalito-granodiorito (TTG) (Machado et al. 1991), ortogranulito Chicrim (Pidgeon et al. 2000) e o *greenstone belt* Sapucaia. Intrusivo no embasamento, pode ser individualizado uma série de corpos de idade Neoarqueana de composição

bimodal e formação sin-tectônica. As rochas supracrustais são constituídas por uma série de terrenos do tipo *greenstone* (Wirth et al. 1986; DOCEGEO 1988) atribuídas ao Supergrupo Itacaiúnas. Granitos paleoproterozoicos ocorrem ao longo do domínio intrusivos tanto no embasamento quanto nas sequências supracrustais (Dall’Agnol et al. 1994).

O Complexo Xingu, representante do embasamento mesoarqueano, possui idades de cristalização entre 3,0 Ga e 2,83 Ga (Machado et al. 1991). São representados predominantemente por tonalitos a trondhjemitos e migmatitos com corpos locais de granitos. Algumas dessas intrusões foram individualizadas localmente, como o tonalito Bacaba (Moreto et al. 2011), trondhjemito Rio Verde e granito Canaã dos Carajás (Feio et al. 2013) simplificados em mapa (Figure 2.2) como granitos, granodioritos e tonalitos. O ortogranulito Chicrim, também individualizado localmente, é constituído por charnockitos com idade de 3,0 Ga (Pidgeon et al. 2000; Vasquez et al. 2008). Ainda associado ao embasamento, uma série de terrenos do tipo *greenstone belt* de idade mesoarqueana foram individualizados (Araújo e Maia 1991) e atribuídos ao grupo Sapucaia, tipicamente composto por komatiitos com textura *spinifex* e a formação de *pillow lavas*.

Intrusivo no embasamento, são observados uma série de intrusões neoarqueanas, bimodais e alongadas subparalelas às principais zonas de cisalhamento. Essas intrusões ocorrem de forma restrita ao Domínio Carajás, apresentando um magmatismo félsico mais expressivo que o magmatismo máfico-ultramáfico (Machado et al. 1991; Feio et al. 2013). Os plútons graníticos são tipicamente alcalinos, metaluminosos e sin-tectônicos ao desenvolvimento de zonas de cisalhamento (Araújo e Maia 1991). A individualização de corpos graníticos foi realizada ao longo de áreas tipos, dentre os quais se destacam os granitos Estrela (Barros et al. 2001), Planalto e Cristalino (Huhn et al. 1999a, 1999b), Serra do Rabo (Sardinha et al. 2001), Plaquê (Araújo e Maia 1991), Igarapé Gelado (Barbosa 2004) e Sossego (Moreto et al. 2015a). Devido a ampla individualização, esse magmatismo félsico foi simplificado na Figure 2.2 como magmatismo félsico neoarqueano (idade entre 2,75 – 2,70 Ga). Pontualmente, granitos com idade de cristalização em torno de 2,57 Ga, marcados por texturas miloníticas a protomiloníticas, são descritos ao longo do lineamento Cinzento (Machado et al. 1991), denominados granito Velho Salobo.

As intrusões máfico-ultramáfico ocorrem alongadas subparalelas a zonas de cisalhamento. De forma geral, são compostos por peridotitos, gabros e noritos associados

à suite intrusiva Cateté (Macambira e Ferreira Filho 2002) e a suíte magmática Serra leste (Ferreira Filho et al. 2007). Complexos acamadados são representados pelo complexo Luanga (Machado et al. 1991; Mansur e Ferreira Filho 2016), Lago Grande (Teixeira et al. 2015), Serra do Onça e Serra do Puma (Macambira e Ferreira Filho 2002, 2005) e Vermelho (Siepierski 2016). Corpos máficos, como o dipsídio norito Pium (Feio et al. 2012) e gabro Santa Inês (DOCEGEO 1988) também fazem parte das intrusões sin-tectônicas. Idades para o magmatismo máfico-ultramáfico ainda não são bem definidas na literatura, porém os dados disponíveis sugerem que seja coeva à volumosa granitogênese neoarqueana no Domínio Carajás (2,76 – 2,70 Ga).

Rochas metavulcano-sedimentares ocorrem recobrando tectonicamente o embasamento (Pinheiro e Holdsworth 1997) e são de forma geral atribuídas ao Supergrupo Itacaiúnas (Hirata et al. 1982; DOCEGEO 1988; Machado et al. 1991; Wirth et al. 1996;). São constituídas por vulcânicas bimodais predominantemente basálticas a intermediárias, formações ferríferas bandadas, ritmitos e rochas vulcanoclasticas metamorfisadas de anquimetamorfismo a facies xisto verde. O Supergrupo Itacaiúnas é subdividido em série grupos (Vasquez et al. 2008) ao longo de áreas tipo, contendo feições similares as descritas a cima. Destacam-se os grupos Igarapé Salobo (Machado et al. 1991), Grão Pará (Machado et al. 1991), Igarapé Bahia (Galarza e Macambira 2002) e Igarapé Pojuca (Machado et al. 1991)

De forma simplificada, as rochas metavulcano-sedimentares foram representadas como Supergrupo Itacaiúnas (Figure 2.2) independente de qual grupo pertencem. A simplificação se baseia na geocronologia similar encontrada ao longo dos diversos grupos, com idades recorrentes entre 2,77 – 2,73 Ga e pontualmente 2,70 Ga (Galarza e Macambira 2002; Galarza et al. 2003). Recobrando o Supergrupo Itacaiúnas de forma parcial, ocorrem as rochas metassedimentares da Formação Águas Claras (Nogueira et al. 1995) com sedimentos fluviais a marinhos rasos metamorfisados em baixo grau, representados como cobertura sedimentar (Figure 2.2).

Intrusivos tanto em rochas do embasamento quanto em rochas supracrustais ocorrem granitos Paleoproterozóicos. Tipicamente do tipo A, alcalinos a subalcalinos, esses granitos podem formar plútons com mais de 10 km de extensão, dos quais se destacam, no Domínio Carajás, os granitos Cigano, Central de Carajás e Rio Branco (Dall’Agnol et al. 1994, 2005) representantes da suíte Serra dos Carajás.

A evolução do Domínio Carajás ocorreu de forma complexa. Inicialmente é esperado um clássico modelo de terrenos do tipo TTG-*greenstone belts* formados em 3.0

a 2.9 Ga. Evidências de subducção e retrabalhamento em ~2.87 Ga podem ser observados pelo magmatismo marcante. Para o Neoarqueno, uma série de modelos evolutivos são propostos, onde é sugerido uma evolução transtensiva-transpressiva (Araújo et al. 1988) com a formação de uma estrutura em flor positiva no sistema de cisalhamento de Carajás. Também são propostos um modelo baseado na reativação de estruturas (Pinheiro e Holdsworth 1997; Domingos 2009), um modelo segundo um rift continental (Gibbs et al. 1986; Wirth et al. 1986; DOCEGEO 1988) e alternativamente um modelo baseado na formação de arcos vulcânicos (Dardenne et al. 1988; Teixeira 1994).

Durante o paleoproterozóico é observado uma ampla granitogênese associada a suíte Serra dos Carajás. Essa granitogênese é recorrente e pode ser observada ao longo de diversos domínios do Cráton Amazônico. Um retrabalhamento tardio ocorreu durante o neoproterozóico quando a formação e colocação tectônica da Faixa Araguaia se deu sobre o Cráton Amazônico (Alvarenga et al. 2000).

2.2.1 Sistema mineralizante Óxido de Fe-Cu-Au-Polimetais em Carajás

A exploração de metais base no Brasil, hoje predominantemente associada a depósitos IOCG, foi inicialmente feita com uso de dados aeromagnéticos e anomalias geoquímicas de solo realizada pela Rio Doce Geologia e Mineração S.A. (DOCEGEO). Os depósitos hoje classificados como IOCG são conhecidos desde 1978, ano da descoberta do depósito Salobo contendo 789 Mt @ 0.96% Cu, 0.52 g/t Au e 55g/t Ag previstos na época (Vieira et al. 1988). O depósito de Cu-Au Igarapé-Bahia seria descoberto logo em seguida (1986-88) durante o mesmo programa de exploração, obtendo 3.36 g/t Au (Tavaza e Oliveira 2000). Atualmente, mais de 20 depósitos classificados como IOCG são conhecidos no Domínio Carajás onde existem duas minas ativas: Salobo e Sossego. Recentemente uma ocorrência foi reportada no Domínio Rio Maria (depósito Pantera, Lopes et al. 2017) sendo a única registrada até então fora do Domínio Carajás.

Revisões abordando os aspectos gerais dos depósitos cupríferos em Carajás (Grainger et al. 2008; Xavier et al. 2012) e compilações de dados geocronológicos (Moreto et al. 2015a, 2015b; Melo et al., 2016) fornecem um escopo geral sobre a metalogênese de Cu-Au no Domínio Carajás. Os depósitos do tipo IOCG (Co-Ni-U-REE) estão dispostos, em sua maioria, ao longo das duas zonas principais denominadas de Cinturões Cupríferos Norte (Cinzento Fault, Figure 2.2) e Sul (Canaã Fault, Figure 2.2) (Moreto et al. 2015a, 2015b; Melo et al., 2016). Idades das mineralizações situam-se em torno de 2.57 Ga e 2.72-2.68 Ga, respectivamente. Um terceiro episódio metalogenético,

representado pelos depósitos de Breves (Botelho et al. 2005) e Santa Lucia (Hunger 2015), está associado ao magmatismo granítico Paleoproterozóico no Domínio Carajás (1.90 – 1.88 Ga) e foi recentemente referido na literatura como representante do tipo Cu-Au-polimetálico (W, Sn, Mo, Bi, Li, Be; Xavier et al. 2017).

Tendo em vista a atual concepção sobre o sistema IOCG (Corriveau et al. 2016; Giustina et al. in prep.), os depósitos podem apresentar uma ampla variação metalífera além do Cu e Au. Com base na conjuntura contemporânea, apenas os depósitos de idade neoarqueana (2.57 Ga e 2.72 – 2.68 Ga) sujeitos ao metassomatismo álcali-Fe devem ser referidos como parte do sistema IOCG de Carajás.



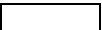


Independente do cinturão cuprífero no qual se localizam, os depósitos IOCG de Carajás ocorrem associados a zonas de cisalhamento de escala regional (e.g. Cinzento, Canaã e Carajás; Figure 2.2) formando corpos subparalelos com característicos mergulhos de alto ângulo. São marcados em geral pela alta tonelagem (>100 Mt), dos quais se destacam (Tabela 2.1) Salobo (1.112 Gt @ 0.69 % Cu e 0.43 g/t Au; VALE 2016), Igarapé Bahia (219 Mt; Tallarico et al. 2005), Sossego (245 Mt; Lancaster Oliveira et al. 2000; Monteiro et al., 2008), Cristalino (500 Mt; Huhn et al. 1999b) e Alvo 118 (170 Mt; Rigon et al. 2000).

Associados aos depósitos de alta tonelagem ocorrem diversos corpos satélites, dentre eles: Visconde (Craveiro et al. 2011), Bacaba (Augusto et al. 2008), Jatobá (Veloso et al. 2016), Bacuri (Melo et al. 2014) e Castanha (Pestilho 2011), no cinturão sul; e GT-46/Igarapé Cinzento (Silva et al. 2005) Furnas (Jesus et al. 2016) e Grota Funda (Hunger et al. 2017), no cinturão norte.

Um fator comum aos depósitos do tipo IOCG são as marcantes zonas de alteração hidrotermal. Inicialmente desenvolve-se uma alteração sódica pervasiva, constituída por escapolita (marialita) e/ou albita, geralmente de tonalidade avermelhada devido à presença de micro inclusões de hematita (Monteiro et al. 2008a, 2008b). Localmente, tal alteração pode atingir temperaturas acima de 700°C, formando a associação de marialita e ortopiroxênio (Garcia et al. 2017; este trabalho). As alterações sódicas tendem a ser mais expressivas no cinturão cuprífero sul.

Table 2.1 – Principais alterações descritas para os depósitos IOCG de Carajás. A representatividade de cada alteração de acordo com cada depósito está dividida em: traço, comum e dominante. Quando a representatividade da alteração não foi descrita está aparece como indiscriminado.

Alterações	Na	Na-Ca	Ca-Fe-Mg	K-Fe (Mt)	Chl-cc	Sulfetos Principais	Ref.
Cinturão Norte							
Antas Norte							
Furnas	Indiscriminado		Indiscriminado	Indiscriminado	Indiscriminado	Cpy + Bn + Cc	Jesus et al. 2015
Grota Funda		Indiscriminado	Indiscriminado	Indiscriminado	Indiscriminado	Cpy + Po + Pn	Hunger et al. 2017
GT-46		Indiscriminado	Indiscriminado	Indiscriminado		Cpy+Bn	Silva et al. 2005
Igarapé Bahia		Indiscriminado		Indiscriminado	Indiscriminado	Cpy+Bn+Py	Tallarico et al. 2005
Paulo Afonso							
Salobo		Indiscriminado	Dominante	Indiscriminado		Bn + Cc + cpy	Melo et al. 2016
Cinturão Sul							
Alvo 118	Indiscriminado			Indiscriminado	Indiscriminado	Cpy+Bn	Torresi et al. 2012
Bacaba	Indiscriminado	Indiscriminado		Indiscriminado	Indiscriminado	Cpy + Py + Bn	Pestilho 2011
Bacurí				Indiscriminado	Indiscriminado	Cpy	Melo et al. 2014
Borrachudos		Indiscriminado	Indiscriminado	Indiscriminado	Indiscriminado	Cpy + Py	Previato 2016
Castanha				Indiscriminado	Indiscriminado	Cpy + Po	Pestilho 2011
Cristalino	Indiscriminado		Indiscriminado	Indiscriminado	Indiscriminado	Cpy+Py	Huhn et al. 1999b
Gt-34	Indiscriminado		Dominante	Indiscriminado	Indiscriminado	Pn+Po	Garcia et al. 2017; este trabalho
Jaguar			Indiscriminado	Indiscriminado	Indiscriminado	Mill	Ferraz et al. 2016
Jatobá		Indiscriminado	Indiscriminado	Indiscriminado	Indiscriminado	Cpy + Po + Pn	Veloso 2017
Sequerinho	Indiscriminado	Dominante		Indiscriminado	Indiscriminado	Cpy+Py	Monteiro et al. 2008a
Sossego	Indiscriminado	Indiscriminado		Dominante	Indiscriminado	Cpy+Py	Monteiro et al. 2008a
Visconde		Dominante	Indiscriminado	Indiscriminado	Indiscriminado	Cpy + Bn	Craveiro et al. 2011

 Traço	 Comum	 Não reportado ou inexistente
 Indiscriminado	 Dominante	

A sequência de alterações é marcada por uma fase sódico-cálcica, descrita em ambos os cinturões, caracterizada essencialmente pelo desenvolvimento de anfibólios cálcicos, além de albita, escapolita, epidoto, alanita, titanita e clinopiroxênio. Nesse estágio pode ocorrer ainda a formação de magnetita (Monteiro et al. 2008a), demonstrando um enriquecimento de ferro associado a essa alteração que por vezes pode ser individualizado como uma alteração ferrosa.

A alteração potássica-ferrosa apresenta evidente relação de corte com as previamente descritas. Aparece na forma de veios constituídos essencialmente por biotita e/ou de feldspato potássico associados a anfibólio e magnetita. Geralmente, alterações com biotita-magnetita formam veios difusos e irregulares, enquanto que feldspato potássico, com microinclusões de hematita conferindo a coloração avermelhada, aparece associado a veios de limites bem marcados (Monteiro et al. 2008a). Essa alteração ocorre de forma variada ao longo dos depósitos, podendo ser dominante (Sossego) a pouco expressiva (Sequerinho), de acordo com a profundidade de formação do depósito (Hitzman 2000). O enriquecimento de ferro pode localmente levar a formação de grunerita e almandina com ocorrência restrita de faialita no depósito Salobo.

De forma tardia e cortando todas alterações anteriores são comuns associações essencialmente hidratadas, de baixa temperatura (inferiores a 300°C), e compostas predominantemente por clorita e/ou calcita. Essa alteração ocorre na forma de veios bem definidos com quartzo, albita e epidoto comumente associados. O desenvolvimento dessa alteração ocorre essencialmente a partir da hidratação de alterações anteriores, sem necessariamente adicionar álcalis-Fe no sistema. Similar a alteração potássica, observa-se uma relação evidente com o nível crustal no qual o depósito se formou, podendo representar uma transformação dominante (Alvo 118, Torresi et al. 2012; Jaguar, Ferraz 2016) a pouco expressiva (Sequerinho, Monteiro et al 2008a).

A mineralização ocorre predominantemente na forma de brechas cimentadas por sulfetos e magnetita com apatita associada. Podem ocorrer associadas tanto em estágios iniciais (sódico-cálcico) quanto em estágios tardios (hidratação) de alteração hidrotermal. Mineralizações iniciais apresentam fragmentos arredondados, tipicamente associados ao domínio dúctil-rúptil de temperaturas mais elevadas. Mineralizações tardias apresentam fragmentos angulosos, típicos do domínio rúptil e temperaturas mais baixas

A mineralogia da mineralização é composta de forma dominante por calcopirita. Bornita e calcocita podem ocorrer localmente em depósitos associados com fluidos mais oxidantes. Pirrotita e pentlandita ocorrem associados a fluidos mais reduzidos. Piritita ocorre em grande parte dos depósitos estudados. Além dos sulfetos principais, uma ampla gama de sulfetos e sulfosais comumente são descritos como traços, a exemplo de covelita, molibdenita, cobaltita, safflorita, bravoita, vaesita, esfalerita, galena e millerita, por exemplo. Tendo em vista a característica polimetálica desses depósitos, alguns podem apresentar elevado enriquecimento em níquel, observado principalmente nos depósitos do cinturão cuprífero sul (e.g. Jaguar – Ferraz 2016; Castanha – Pestilho 2011; Jatobá – Veloso et al. 2016; GT-34 – Garcia et al. 2017; este trabalho) nos quais pentlandita e/ou millerita representam a fase sulfetada principal.

Capítulo 3: *The Ni-rich GT-34 deposit: A view into the deep alteration zones of the Carajás Neoproterozoic IOCG system, Brazil*

3.1 Abstract

The GT-34 deposit, which is located 12 km SW of the Sequerinho copper-gold mine, Carajás Province, northern Brazil, represents an unusual Ni occurrence related to a regional Iron-Oxide-Copper-Gold (IOCG) system. It occurs along a NE-SW-trending sub-vertical shear zone marked by progressive alkali-Fe alteration zones hosted in tonalite to granite intrusions. Initial Na-Mg and pervasive Ca alteration forms the unique marialite-orthopyroxene and hornblende-plagioclase-clinopyroxene associations, respectively. Nickel mineralization occurs as breccias in a pentlandite-pyrrhotite-apatite-rich matrix with rounded fragments chiefly of Ca-alteration parageneses. Late-stage veins of K-Fe magnetite and hematite (K-Fe (Mt) and K-Fe (Hem)) alterations partially remobilize the mineralization, reprecipitating as chalcopyrite-pyrrhotite-magnetite and as millerite-pyrite-apatite, respectively. Potassium-Fe (Mt) occurs as irregular phlogopite-talc-rich veins, while K-Fe (Hem) occurs as sharp K-feldspar-albite-quartz-chlorite-calcite-epidote veins. Initial fluid characteristics associated with Na-Mg alteration require anhydrous conditions for orthopyroxene stability and high salinity for marialite formation. An immiscible CO₂-NaCl fluid is therefore associated with such conditions. The presence of orthopyroxene indicates temperatures >700°C. Experimental studies indicate that marialite does not form with NaCl-rich fluid at pressures >7 kbar under such temperatures. The absence of quartz might be caused by NaCl dissolution at pressures >5 kbar, as determined experimentally with the same temperature conditions. Zircon crystal were recovered from the initial Na-Mg alteration and late-stage K-Fe (Mt) alteration yielding a concordant 2.724±4 Ga age, corroborating the GT-34 Neoproterozoic formation similar to other IOCG deposits in Carajás. At >700°C and 5–7 kbar, an eventual evaporitic fluid source would not be present, making a magmatic fluid source necessary. The age constrains obtained in this study overlaps the bimodal Neoproterozoic magmatism (2.75–2.70 Ga), supporting a magmatic-hydrothermal origin. Determination of such conditions raises the initial temperature of the Carajás IOCG system at least 200°C and pressure up to 7 kbar, making GT-34 the deepest IOCG-related occurrence known to date for this province.

3.2 Introduction

The Carajás Domain, northern Brazil, in the southeastern portion of the Amazon craton, represents a Mesoproterozoic crust world-famous for its well-endowed (Fe-Mn-W-Cr-Ni-PGE-Au-Cu) deposits (Dardenne and Schobbenhaus, 2001; Vasquez et al., 2008). Iron-Oxide-Copper-Gold (IOCG) occurrences are chiefly associated with this domain and controlled by the regional E-W to WNW-ESE Carajás and Cinzento strike-slip system (Pinheiro et al., 2013).

The IOCG deposits from the Carajás Domain account for more than 2 billion tons (Xavier et al., 2012) of measured reserves at 0.69–1.4% Cu and 0.28–0.86 g/t Au. Mining operations started in 2004 at Sossego (355 Mt at 1.1% Cu and 0.28 g/t Au; Lancaster Oliveira et al., 2000) and recently, in 2011, at Salobo (1,112 Mt at 0.69% Cu and 0.43 g/t Au; Vale 2016).

Ore deposits in Carajás Domain IOCG deposits are believed to have been emplaced from shallow (Sossego, Alvo 118) to middle (Sequerinho, Cristalino, Salobo) crustal levels and at temperatures above 500°C (Huhn et al., 1999; Lindenmayer, 2003; Réquia et al., 2003; Monteiro et al., 2008a, 2008b; Torresi et al., 2012). Deposits emplaced in middle crustal level display dominantly Na to Na-Ca alterations with pervasive albite to albite-actinolite formation at

Sequerinho and Cristalino. Garnet-grunerite with local fayalite is observed in the Salobo alteration zone.

The GT-34 deposit, situated 12 km SW from the Sequerinho copper-gold mine (Figure 3.1), is a brecciated Ni deposit associated with the deep Carajás regional IOCG system (Siepierski, 2008). Unlike other typical IOCG occurrences, it consists of a brecciated pentlandite-pyrrhotite-apatite-rich nickel mineralization. Siepierski (2008) first described GT-34 as a deeper part of the regional IOCG system, suggesting a two-phase formation: first, an initial deep high-temperature magnesium alteration and second, the nickel mineralization. The unique orthopyroxene presence as a metasomatic alteration product displays low Ti, Cr, Al and Ca contents (This study) when compared to typical igneous and/or metamorphic orthopyroxene, making GT-34 an unique example for considering regional IOCG formation conditions. However, the proper characterization of alteration zones in GT-34 and the association with classic IOCG processes were not made during the initial study by Siepierski (2008).

In this work, alteration zones, mineralization and respective geochronology are characterized and detailed within typical alkali-Fe alteration zones. Possible fluid sources and the development of classic IOCG processes are also discussed for GT-34 deposit. Our estimated initial P-T conditions based on the observed parageneses, together with available experimental studies from the literature, define GT-34 as the deepest occurrence discovered to date for the Carajás Domain Neoproterozoic IOCG systems.

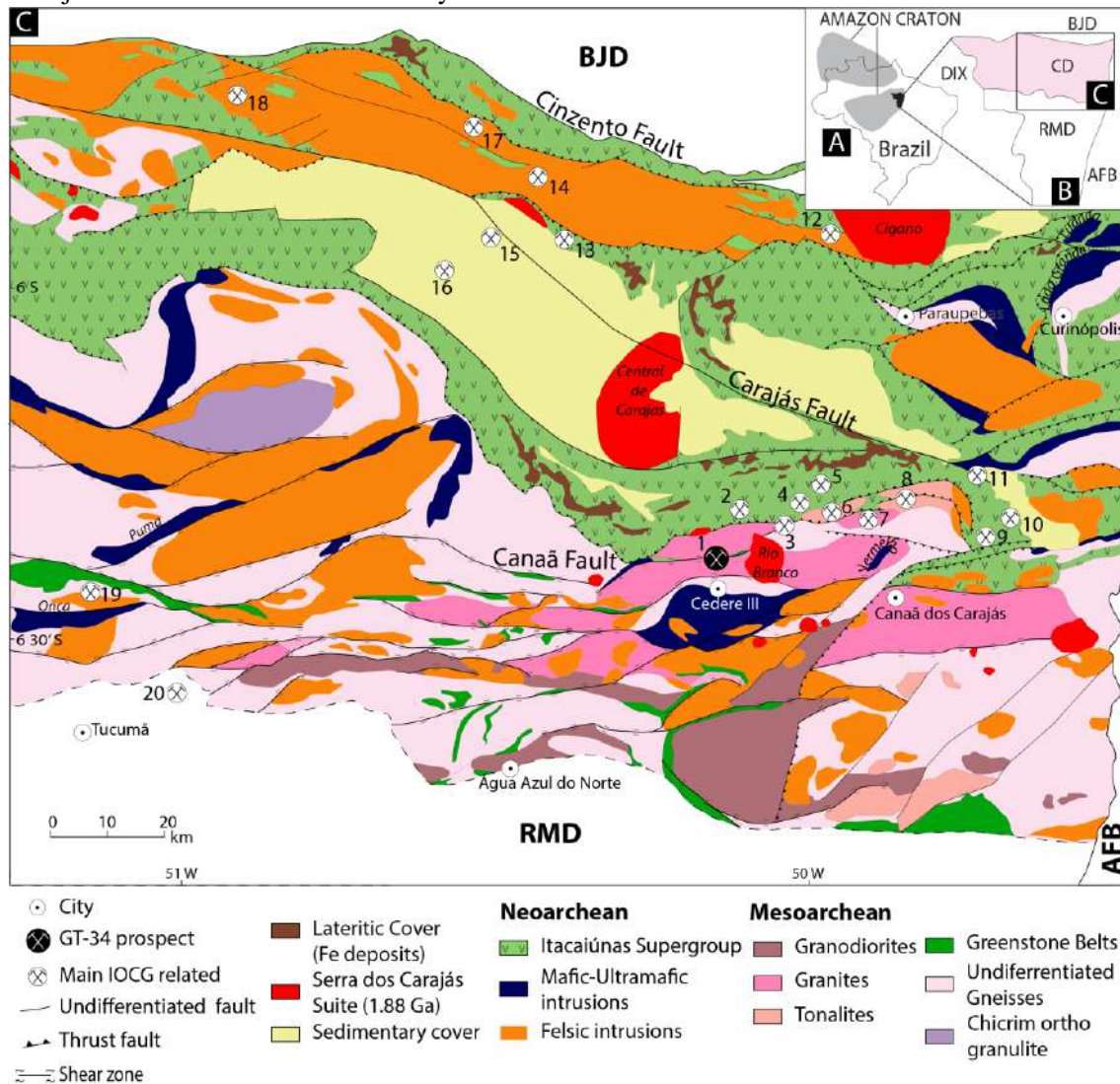


Figure 3.1 – Geological map of Carajás Domain. A – Location of Carajás Domain in the Amazon craton. B – Carajás Domain limits with other individualized tectonic domains. C – Detailed main lithologies and structures in Carajás

Domain. Main IOCG-associated deposits are numbered 1 to 20: 1 – GT-34; 2 – Alvo 118; 3 – Sossego-Sequerinho; 4 – Jatobá; 5 – Castanha; 6 – Bacaba; 7 – Visconde; 8 – Bacurí; 9 – Borrachudos; 10 – Cristalino; 11 – Estrela; 12 – Furnas; 13 – Gameleira; 14 – Paulo Afonso; 15 – Pojuca; 16 – Igarapé Bahia/Alemão; 17 – Salobo; 18 – Igarapé Cinzento/GT-46; 19 – Jaguar; 20 – Pantera; RMD – Rio Maria Domain; AFB – Araguaia Fold Belt; BJD – Bacajá Domain; DIX – Domain Irixi-Xingu. Modified from Costa et al. (2016).

3.3 Carajás Regional Geology

The Carajás Domain is situated in northern Brazil at the southeastern border of the Amazon Craton (Santos, 2003; Vasquez et al., 2008). The province is limited in the north by the Paleoproterozoic Bacajá Domain (BJD) separated by the Cinzento Fault and in the east by the Neoproterozoic Araguaia fold belt (AFB). The NW-SE-trending Paleoproterozoic Irixi-Xingu (DIX) marks the western limit, while the Mesoarchean Rio Maria Domain (RMD) (Figure 3.1) marks the southern limit.

The main Archean terranes of the Amazon Craton are the Carajás Domain and the RMD. The Rio Maria Domain is a classic granite-greenstone terrane (DOCEGEO, 1988; Pimentel and Machado, 1994) containing only one IOCG occurrence recently reported (Lopes et al., 2017). In the Carajás Domain, the main basement units are 3.0- to 2.83 Ga Mesoarchean orthogneisses and migmatites of the Xingu Complex with individualized tonalite, granite, granodiorite and trondhjemitic bodies (Machado et al., 1991; Moreto et al., 2011; Feio et al., 2013). Locally, the basement appears as the 3.0 Ga Chicrim orthogranulite (Araújo and Maia, 1991; Pidgeon et al., 2000). Greenstone belts fragments displaying pillow lavas and spinifex texture are associated with the Sapucaia Group and also constitutes the Mesoarchean basement (Araújo and Maia 1991; Siepierski 2016).

Intruding into the basement there are differentiated syn-tectonic Neoproterozoic bimodal magmatic rocks. These differentiated rocks are ubiquitously lenticular and highly deformed, with compositions ranging from tonalite to granite (e.g., Plaqué, Estrela, Serra do Rabo, Planalto – Hirata et al., 1982; Araújo et al., 1988; Huhn et al., 1999b; Sardinha et al., 2006). Mafic-ultramafic Neoproterozoic complexes (e.g., Luanga, Puma, Onça – Machado et al., 1991; Lafon et al., 2000; Macambira and Ferreira Filho, 2002; Ferreira Filho et al., 2007) also occur, aligned with structural lineaments and accompanied by a few individual gabbros and norites bodies (e.g., Pium Diopside Norite – Feio et al., 2012). The age of these bodies vary from 2.75-2.70 Ga and define the Neoproterozoic magmatism, which represents the main difference between the Carajás Domain and the RMD.

Chronologically correlated with the Neoproterozoic magmatism there is a series of supracrustal units tectonically covering the basement (Pinheiro and Holdsworth, 1997). Supracrustal units range from anquimetamorphic to greenschist facies, are mainly basalt to intermediate volcanic composition and banded iron formations with local volcanoclastic, known as the Itacaiúnas Supergroup (Hirata et al., 1982; Wirth et al., 1986; DOCEGEO, 1988; Vasquez et al., 2008). The Itacaiúnas Supergroup is separated into several metavolcanic-sedimentary groups (e.g., Grão Pará, Igarapé Bahia, Pojuca and Salobo). Meta-siliciclastic sediments of the Águas Claras Formation (Nogueira et al., 1994) overlie the supracrustal units, forming fluvial to shallow marine sequences metamorphosed at low grades represented as sedimentary cover in Figure 3.1.

Paleoproterozoic 1.88 Ga granites intrude both the basement and the supracrustal cover. The composition is essentially A-type monzogranite with subordinate syenogranite (e.g., Rio Branco, Cigano, Central de Carajás – Machado et al., 1991). These rocks are widespread throughout the Amazon Craton and in the Carajás Domain are representative of the Carajás Suite (Dall’Agnol et al., 1994). Locally, the rocks may be associated with another mineralization style referred as Cu-polymetallic (Xavier et al., 2017)

The structural trend is E-W and ESE-WNW, dominated by two distinct strike-slip systems: the Cinzento and the Carajás strike-slip systems (Pinheiro and Holdsworth, 1997). The Cinzento system is present in northern Carajás Domain marking the limit with the BJD. The

Carajás system contains both the Carajás and Canaã faults forming the Carajás sigmoidal structure. The development of these structural systems is associated with different tectonic evolution models, which are still under discussion to the present day. Transtensive-transpressive evolution has been proposed (Araújo et al., 1988), followed by a reactivation model (Pinheiro and Holdsworth, 1997; Domingos, 2009). A continental rift setting (Gibbs et al., 1986; DOCEGEO 1988) is the most commonly accepted model. The formation of a volcanic arc model has also been considered (Dardenne et al., 1988).

3.4 Carajás IOCG deposits

Iron-Oxide-Copper-Gold mineralization from the Carajás Domain represents the world's largest known cluster of large-tonnage (100–1112 Mt at 0.69–1.4% Cu and 0.28–0.86 g/t Au) IOCG deposits (Monteiro et al., 2008b; Grainger et al., 2008; Xavier et al., 2012; deMelo et al., 2016). Recently, the Carajás Domain IOCG deposits were divided into two sectors: the northern copper belt and the southern copper belt.

The northern copper belt contains deposits situated along the Cinzento strike-slip system and at the northern end of the Carajás strike-slip system. Deposits hosted along this belt include Salobo, Igarapé-Bahia, Breves, Paulo Afonso, Furnas, Gameleira, Pojuca and GT-46/Igarapé-Cinzento (Figure 3.1). Orebodies of this sector are typically associated with magnetite bodies and garnet-grunerite-biotite-tourmaline with local fayalite. Pervasive chlorite alteration may also be observed at Igarapé-Bahia. Mineralization occurs as lenses concordant (Prado, 2017) with the foliation (chalcopyrite) or as discordant sulfide-rich veins (bornite-chalcocite).

In the southern copper belt (Moreto, 2013), the Canaã Fault is the main structural control of the mineralization. The Sossego-Sequerinho represent the best documented deposits with a series of satellite occurrences known as Jatobá, Castanha, Bacaba, Bacuri, Visconde and GT-34 (this study) (Figure 3.1). Alteration zones identified are ductile to brittle-ductile sodic (albite-scapolite), sodic-calcic (actinolite-albite) and magnetite-apatite, dominant at Sequerinho (Monteiro et al., 2008a, 2008b) and Cristalino (Huhn et al., 1999). Alteration zones in these two deposits represent the deeper part of the IOCG system (apart from this study) forming at approximately 500°C. Mineralizations occur as breccias with rounded fragments of the previous alterations in a chalcopyrite-rich matrix.

Brittle potassium alteration (biotite-potassium feldspar) with late-stage chloritization and hydrolytic alteration are dominant at shallower deposits such as Alvo 118 and Sossego. Initial sodic and sodic-calcic alterations are present but with restricted occurrence. Mineralization on these deposits appears as stockwork calcite-quartz-epidote-chlorite veins with associated chalcopyrite-pyrite. Variable contents of U-Ni-Co-Pd-Y-Sn-Bi-Be-Pb-Ag-Te-REE are recurrent in most IOCG-associated deposits, emphasizing the polymetallic characteristic of these deposits.

Geochronological differences between the northern and southern copper belts suggest distinct timings of mineralization. The former occur at 2535 ± 8.4 Ma (deMelo et al., 2016), while the latter occur at 2.71–2.68 Ga for deeper deposits (Sequerinho, Cristalino) and 1.90–1.88 Ga (Moreto et al., 2015a, 2015b) for shallower deposits (Sossego, Alvo 118). The identification of Paleoproterozoic mineralization in the southern deposits is coincident with the Rio Branco A-type granite that probably remobilized the previously mineralized system.

3.5 Methodology

This study was made using 21 samples of different textures and cross cutting relations obtained from one drill core section. The drill core that was selected for sampling displayed the most elevated metals content, although values not available for publication. From the 21 selected samples it was made 25 polished thin sections which were described at the microscopy laboratory at the University of Brasília. Selected spots were analysed for mineral chemistry using a JEOL JXA-8230 SuperProbe with five wavelength dispersive spectrometers (WDS) in the Electron

Probe Microanalyzer (EPMA) carried out at the University of Brasília (Brazil). Systematic analyses were obtained for Opx, Scp, Plg, Cpx, Phl and general amphibole and apatite types with a total of 217 analyses. Operating conditions for the WDS were an accelerating voltage of 15 kV and a beam current of 10 nA. The spot size was one μm with 10s counting times on peak and five seconds on background.

For geochronology analyses it was selected two samples (3A and 11B). The first sample (3A) displayed a dominant Na-Mg alteration with partially preserved host rocks domains. The second sample (11B) displayed a dominant K-Fe (Mt) alteration with fragments of the previous Ca-alteration. From both samples zircon crystals were recovered and selected for imaging and analyses. The analyses were performed using a secondary ion mass spectrometry (SIMS) (CAMECA IMS1280 large-geometry ion microprobe) at the NordSIMS facility, Swedish Museum of Natural History, Stockholm, Sweden. Procedures followed routine protocols described by Whitehouse et al. (1999) and Whitehouse and Kamber (2005). Zircon grains from the two samples were mounted together with the 91500 reference material in epoxy blocks; prior to U-Pb SIMS analyses, samples were cleaned in an ultrasonic bath, dried and coated with 30nm layer of Au. Data reduction was performed using an in-house spreadsheet and calculations used Isoplot v. 4.13 (Ludwig, 2012).

3.6 GT-34 deposit

The GT-34 deposit was first discovered in 1999 by VALE during an airborne EM survey. The abbreviation GT-34 stands for GEOTEM anomaly number 34, a nomenclature used to define highly magnetic targets defined using geophysical data. The follow-up exploration using soil geochemistry and ground geophysics resulted in brecciated sulfide-rich intersections. In 2003, detailed ground geophysics and systematic drilling defined a NE-trending irregular body approximately 1.5 km long and up to 500 meters deep (Siepierski, 2008). Resources and tenors are not available for publication.

The host rocks are dominantly tonalitic to granodiorite gneisses with biotite (Bt) and hornblende (Hbl), occurring along a NE-SW shear zone associated with the Canaã fault system. Local gabbro bodies have been described but not identified by drill core logging or in thin sections. The GT-34 deposit is located 12 km SW from Sossego mine and 3 km from Cedere III city (Figure 3.2).

This new study verifies that the GT-34 deposit actually displays four different alteration zones and one main mineralization stage based on crosscutting and stability relations. Alteration names are based on the major element enrichment of each phase. Initially, there is a sodic-magnesium (Na-Mg) alteration marked by scapolite (Scp) and orthopyroxene (Opx), followed by calcic (Ca) alteration with widespread hornblende (Hbl) associated with plagioclase (Plg) and local clinopyroxene (Cpx) (Garcia et al., 2017).

The main mineralization follows the Ca alteration and forms sulfide-apatite-rich breccias that are reworked, respectively, by potassium-magnetite (K-Fe (Mt)) and potassium-hematite (K-Fe (Hem)) alteration. Potassium-magnetite alteration forms mainly phlogopite (Phl), talc (Tlc) and magnetite (Mt) as irregular veins with fuzzy boundaries, while K-Fe (Hem) alteration forms quartz-albite veins with sharp boundaries and characteristic red potassium feldspar (Kf), albite (Ab) rich in Hem inclusions, chlorite (Chl), epidote (Ep) and calcite (Cc).

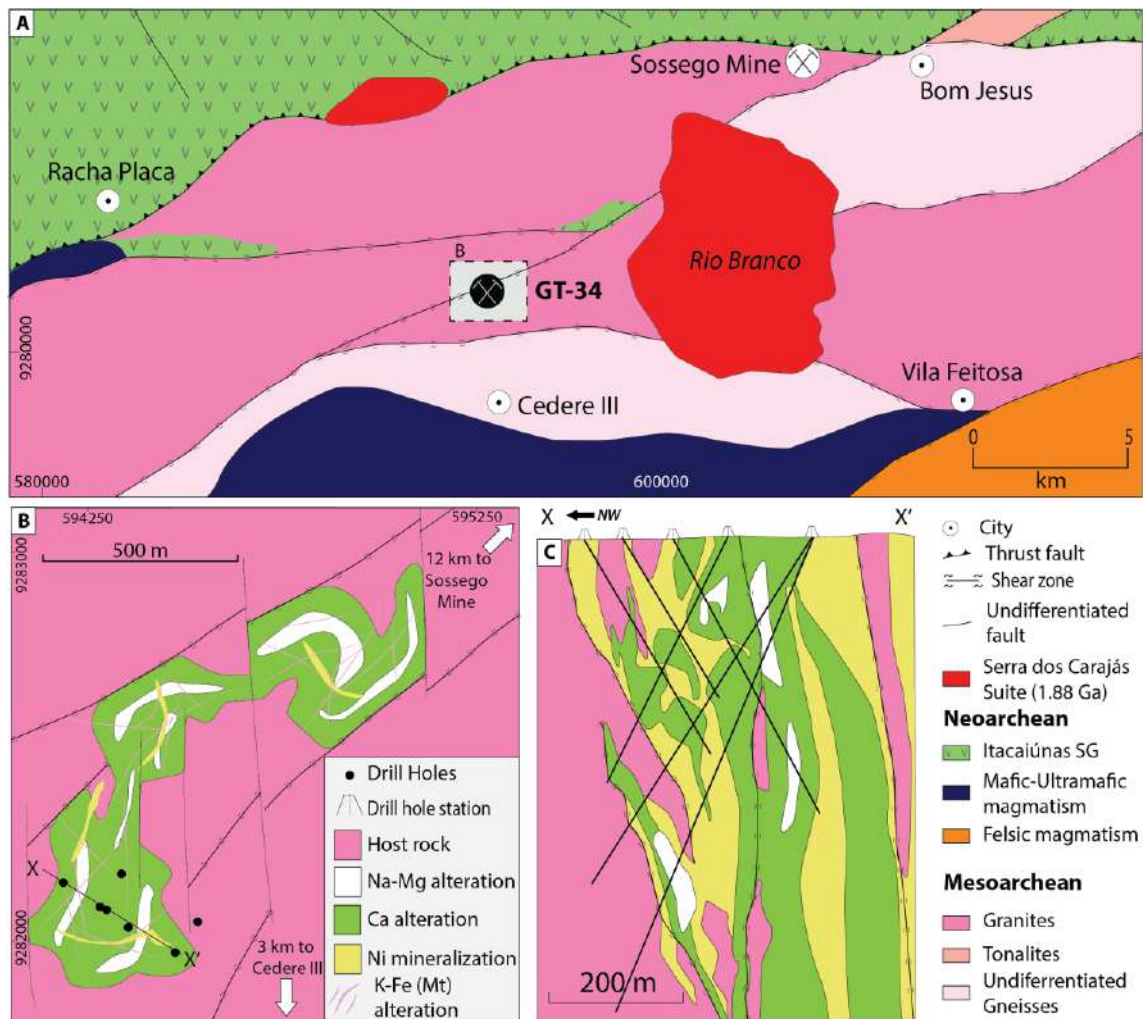


Figure 3.2 – GT-34 location, geological map and associated alteration zones. A – Local structures, main lithologies and location of the GT-34 deposit. B – GT-34 schematic alteration zones identified in map view. C – Cross-section of the alteration profile, mineralized zones and drill hole locations. SG – Supergroup. Modified after Sieperski (2008)

3.6.1 Host Rocks

Partially preserved host rocks are composed of tonalite to granodiorite associated with the Mesoarchean basement. The host rocks display an incipient foliation with subparallel alteration pods composed of variable amounts of Scp, Opx and Hbl (Figure 3.3 A) that may become pervasive towards increased deformation zones. Medium plagioclase (Plg) and quartz (Qtz) sigmoidal fenocrystals with typical undulose extinction are common and may appear limited by fine Qtz ribbons, with an alteration assemblage present in strain shadows. Igneous Bt and Hbl are present in minor amounts, although they have been described as common in these rocks (Vasquez et al., 2008). Although local gabbros have been described, these rocks were not observed during our studies.

3.6.2 Na-Mg alteration

The earliest alteration type (Na-Mg alteration) is present as partially preserved lenses of Scp and Opx within the subsequent alteration zones. In hand sample, Scp appear as light gray to white-colored fine crystals that envelop Opx grains (Figure 3.3 B, C). Orthopyroxenes appear as dark gray, fine to coarse euhedral crystals, forming aggregates that do not extend for more than a

meter. Typically, Scp-Opx are cut by Hbl veins (Figure 3.3 B.), Tlc veins and less commonly by Qtz-Chl veins.

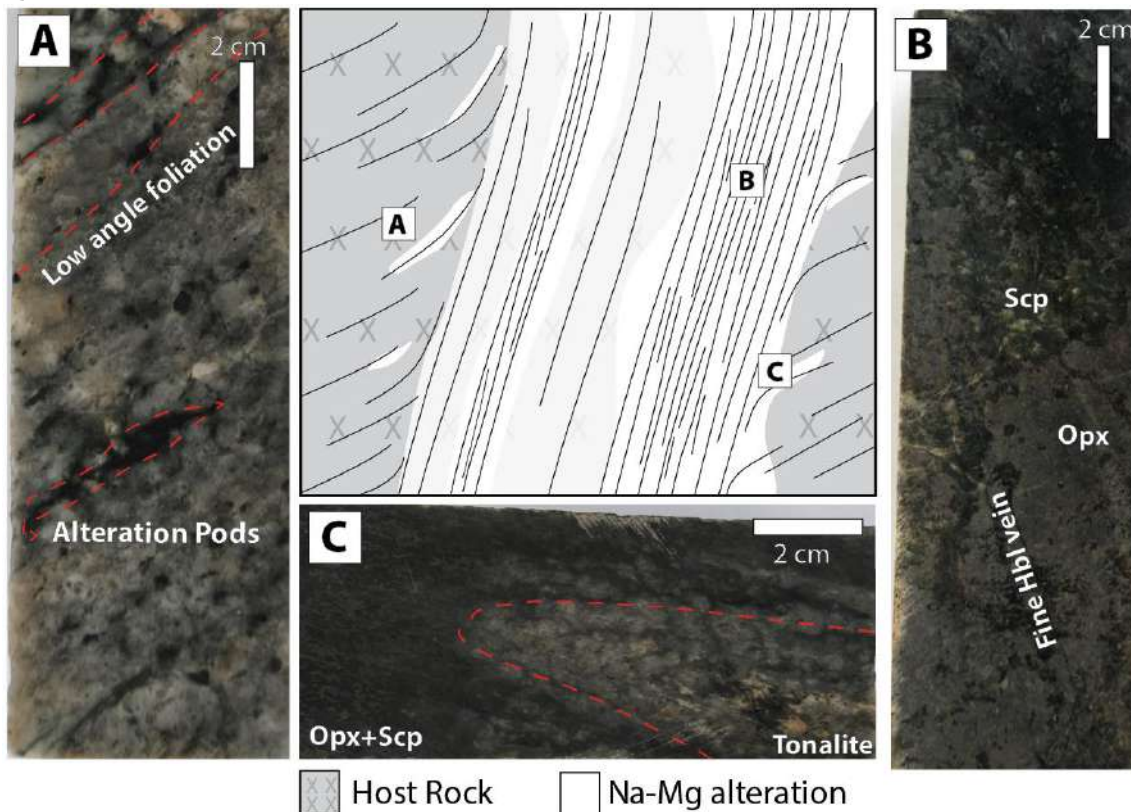


Figure 3.3 – Schematic representation of Na-Mg alteration. Samples are located within the scheme by the corresponding letters. A – partially preserved tonalite (host rock) and individual alteration pods. B – Well developed Na-Mg alteration with coarse Opx crystals and fine Scp cut by thin Hbl vein. C – Partially preserved tonalite enveloped by Na-Mg alteration.

In thin sections, Scp is present with two main textures: medium subhedral crystals typically having planar contacts with fine to medium euhedral Opx crystals (Figure 3.4 A) or fine granoblastic texture (Figure 3.4 C) with local domains showing undulose extinction that suggests recrystallization. The planar contact texture is associated with partially preserved deformation zones with undulose extinction, while the fine granoblastic texture with undulose extinction relates to increased deformation zones. The Scp formation may also develop over igneous Plg (Figure 3.4 B) forming localized Plg relicts.

Orthopyroxene appear as fine to coarse euhedral crystals (Figure 3.4 A, B, C; Figure 3.5 B, C) with very fine Mt inclusions. Coarse Opx crystals typically display recrystallization with subgrain formation along their borders (Figure 3.4 C) and may also develop local bends. Fine Opx appears forming local granoblastic textures or developing within the pressure shadows of relict igneous Plg altered to Scp (Figure 3.4 B). Relict Opx crystals with irregular borders are

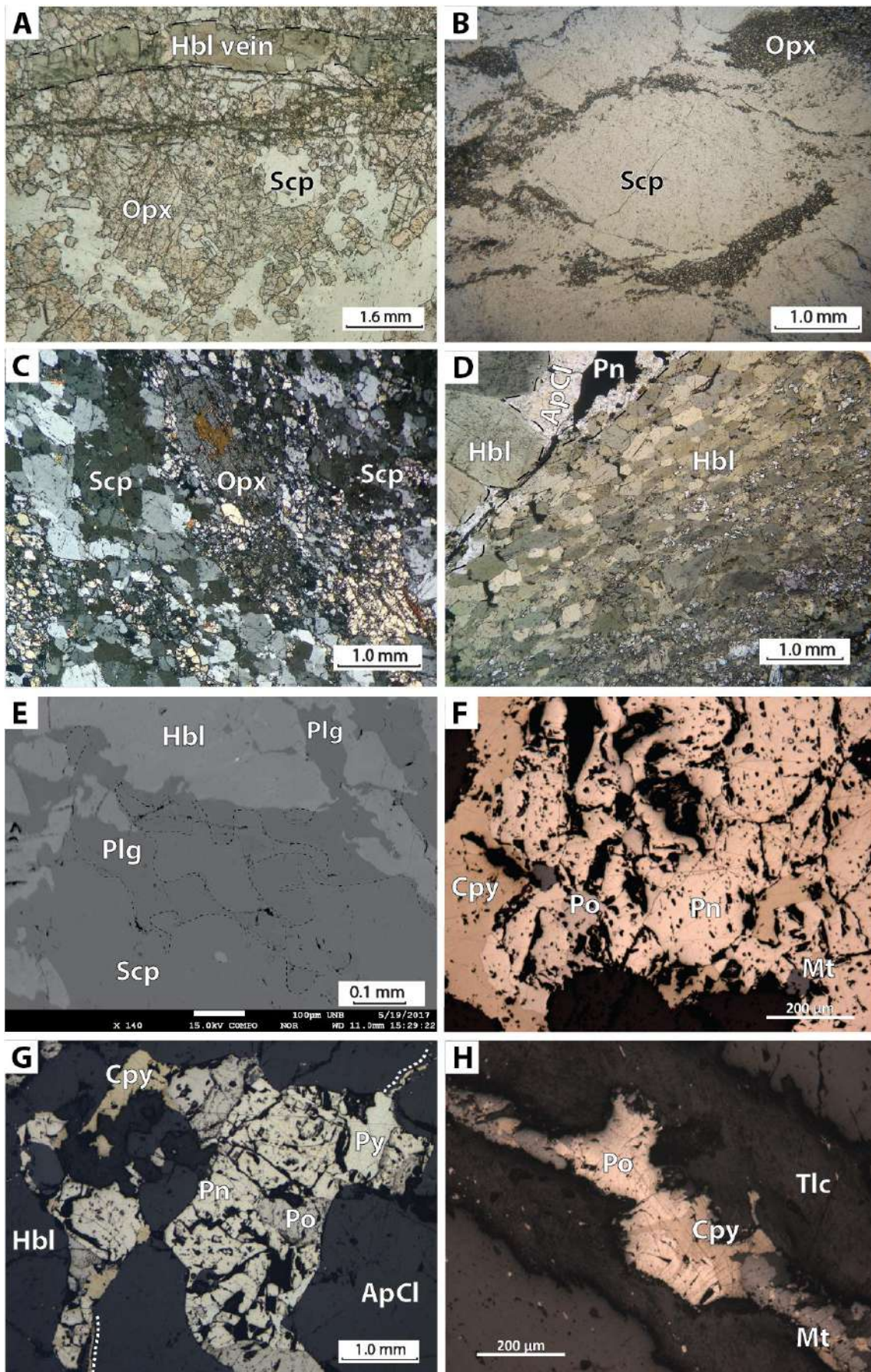


Figure 3.4 – Detailed observations of different alteration zones: A, B, C (Na-Mg alteration); D, E (Ca alteration); F, G (Ni mineralization); H (remobilization during K-Fe (Mt) alteration). A – Fine-grained Opx and Scp cut by Ca

alteration Hbl vein. B – Relict igneous Plg sigmoidal phenocryst altered to Scp with fine Opx developing in the pressure shadow. C – Granoblastic Scp with narrow fine Opx bands. Local coarser Opx crystals are found as porphyroblasts. D – Coarse Hbl associated with Ni mineralization at top left and nematoblastic Hbl within increased deformation bands. Fine Plg pods may be observed within nematoblastic domain. E – BSE image of Scp, Plg and Hbl relations. Scp is light gray while Plg is dark gray with irregular relationship highlighted by red dashed line. F – Nickel mineralization with Pn and Po. Chalcopyrite occurs at the borders typically in contact with Ca alteration with associated subhedral Mt crystals. G – Nickel mineralization partially remobilized forming very fine veins (white dashed line). Note Py formation associated with the remobilization. H – Detail of first remobilization and reprecipitation of sulfides and magnetite during K-Fe (Mt) alteration.

commonly found within Hbl, verifying that Opx formation occurred prior to that of Hbl. Trace zircon crystals were identified associated with this alteration stage. The zircon crystals were handpicked and dated.

3.6.3 Ca alteration

The second alteration (Ca alteration) also occurs during brittle-ductile deformation, is pervasive and may be locally present as irregular veins infilling. This alteration is constantly present and represents the best-developed alteration type. In hand sample, the Ca alteration is most commonly identified as hornblendites with fine to coarse adiablastic Hbl crystals (Figure 3.5 A) or may also be locally present as millimetric regular Hbl veins (Figure 3.3 B) to centimetric irregular Hbl veins (Figure 3.5 B, C) cutting the initial Na-Mg alteration. Hornblende is the main mineral formed during this alteration, with Plg occurring locally and altering the previous Scp (Figure 3.4 Figure 3.3 E).

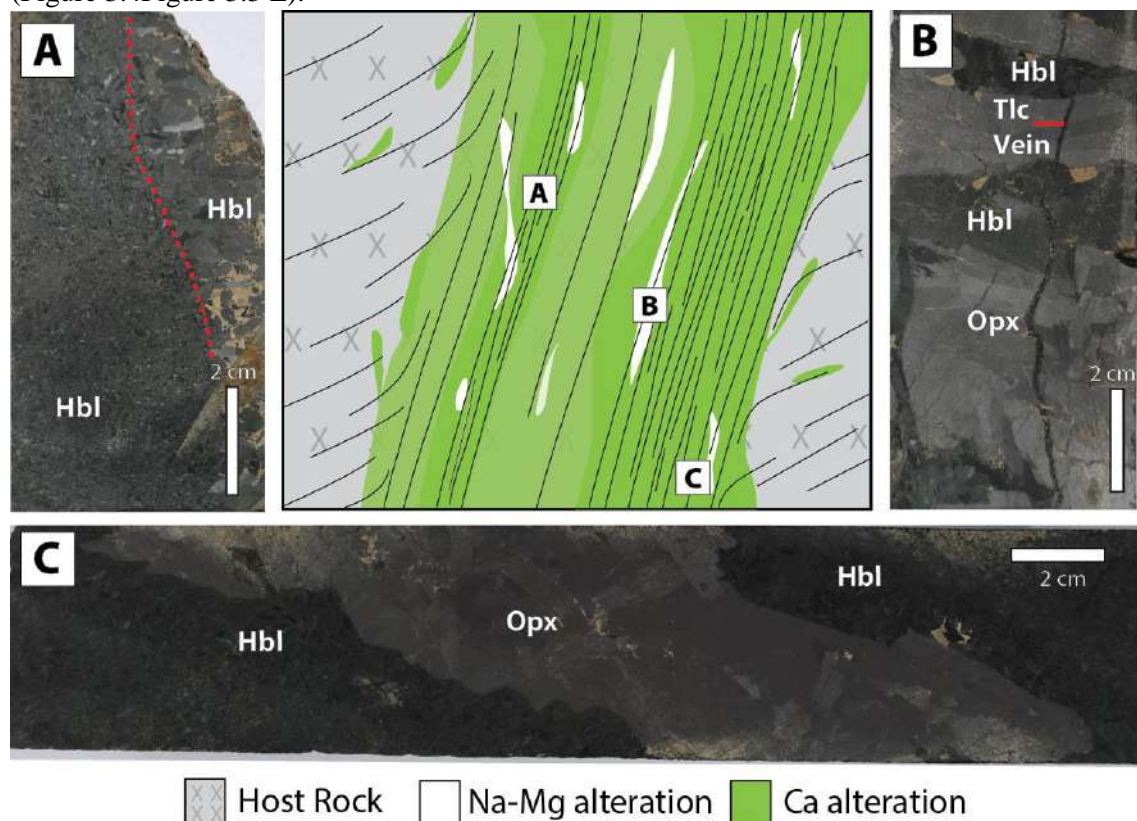


Figure 3.5 – Schematic representation of Ca alteration. Samples are located within the scheme by the corresponding letters. A – Fine nematoblastic Hbl separated by a dashed line from the medium- to coarse-grained Hbl. Larger crystals are associated with sulfide formation. B – Sodic alteration Opx cut by irregular Ca alteration Hbl. Fine millimetric late-stage Tlc vein (red line) cuts and partially remobilizes the previous stages. C – Calcic alteration Hbl displaying Na-Mg alteration Opx.

Under the microscope, it is possible to identify bands with Hbl forming a nematoblastic texture (Figure 3.4 D) associated with increased deformation zones. Coarse Hbl grains are normally found near mineralized zones but can also be present as porphyroblasts within nematoblastic bands. Plagioclase appears locally forming fine to medium anhedral pods, preferentially over partially preserved Scp fragments enclosed by Hbl (Figure 3.4 D). A scapolite-Plg reaction may form local irregular rims with Scp nuclei and Plg at the borders confined by Hbl (Figure 3.4 E). Clinopyroxene is of restricted occurrence and identified in one sample. It appears associated within fine deformation bands where the host rock is still partially preserved and alteration zones are not well developed.

3.6.4 Ni mineralization

Nickel mineralization comprises the main ore-forming stage, forming nickel sulfide breccias chiefly represented by pentlandite (Pn) with concomitant chlorapatite (ApCl). The mineralization is typically emplaced where the Ca alteration is dominant. However, the mineralization is not restricted to its development and may form cutting the initial Na-Mg alteration and, less commonly, on partially preserved tonalities to granodiorites. Associated with Pn, pyrrhotite (Po) is the second most common sulfide formed during this stage. Subhedral pyrite (Py) may appear associated with Po at marginal portions, while chalcopyrite (Cpy) forms dominantly at the contact of the main mineralization and the directly adjacent rock (Figure 3.4 F).

Typically, the mineralization appears as discordant centimetric to metric breccias (Figure 3.6 A, B) with a matrix mainly composed of Pn, Po and ApCl. Breccia fragments are rounded and dominated by Hbl, with rounded fragments of Scp and Opx locally present. Breccias may appear as matrix-rich (sulfide is dominant), or as matrix-poor (fragments are dominant), both types with no apparent spatial control. Chlorapatite forms fine to coarse rounded crystals similar to fragments at first glance but may also grow as a marginal corona over the fragments (Figure 3.6 B). The ApCl growth over the borders of the fragments suggests that it formed concomitant with the main sulfide mineralization.

Apart from breccias, nickel mineralization also appears as fine irregular veins to net-textured sulfidation (Figure 3.6 C). This mineralization is proximal to the breccia type and forms centimetric, discontinuous marginal sulfide zones. Within vein to net-textured sections, Cpy is relatively more common than it is in the breccia type.

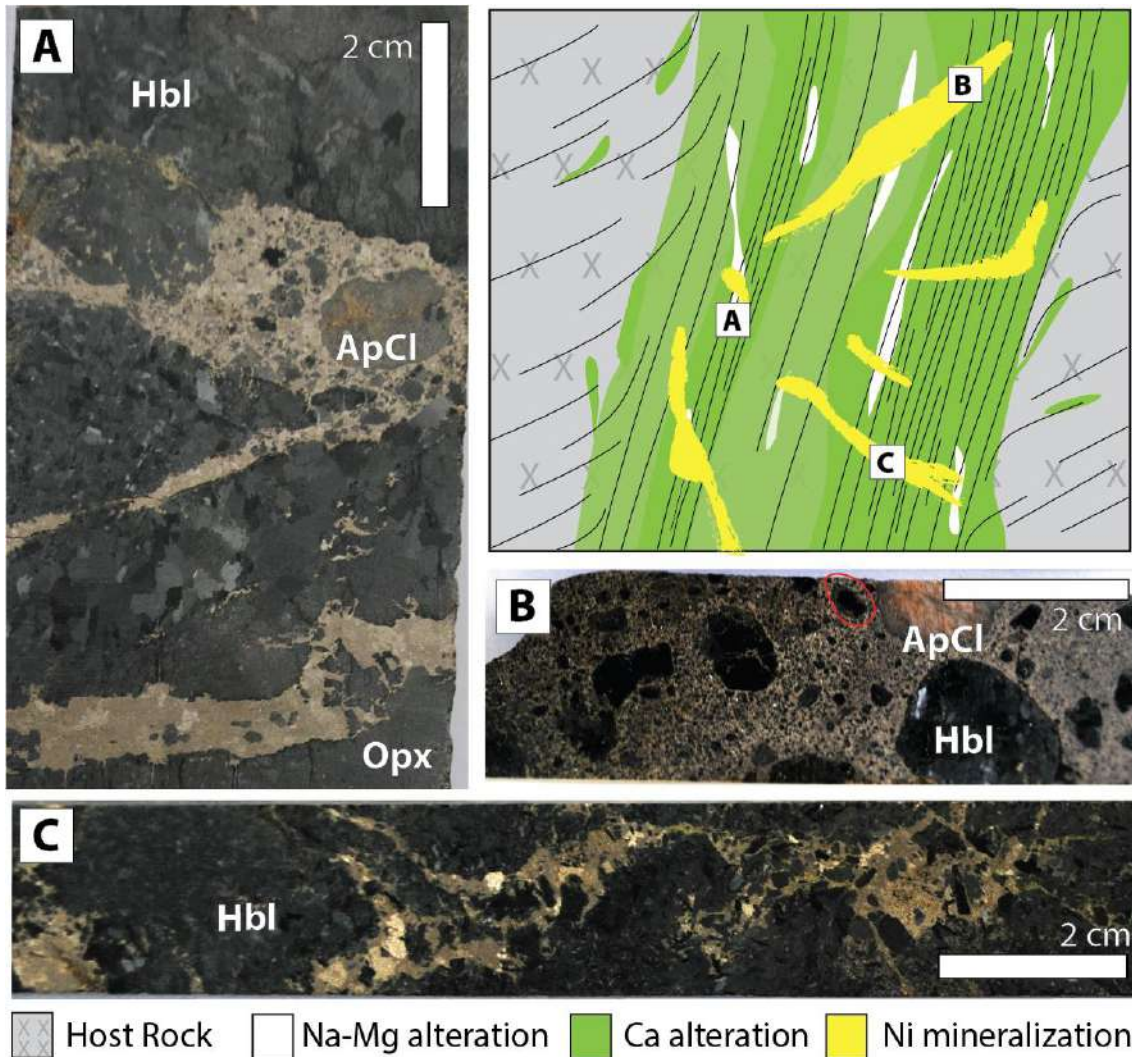


Figure 3.6 – Schematic representation of Ni mineralization. Samples are located within the scheme by the corresponding letters. A – Veins forming breccias with sulfide-rich matrix, angular to rounded fragments with coarse ApCl formation cutting the Na-Mg and Ca alteration. B – Breccia with sulfide-rich matrix and rounded Hbl fragments. Red circle highlights ApCl overgrowing Hbl fragments. C – Irregular to net-textured veins associated with the Ca alteration.

Under the microscope with reflected light, Pn forms euhedral crystals with marked octahedral partition. The Pn size varies from fine to medium, and it appears on the borders of fine Po (Figure 3.4 F, G). Pyrrhotite distinctly displays considerable inclusions and locally may form small Pn flames. Trace amounts of melonite, thorite and monazite appear at the contacts with ApCl. Calchopyrite is present as very fine millimetric veinlets, most commonly present along Hbl cleavages. Magnetite occurs as fine euhedral to subhedral crystals typically associated with Po and Cpy. Under the microscope with transmitted light, ApCl shows distinct irregular zonation with variable monazite, Mt and fluid inclusions.

3.6.5 K-Fe (Mt) alteration and first sulfide remobilization

This stage appears as veins with fuzzy borders forming a restricted scale alteration developed in association with brittle deformation. Phlogopite, Tlc and Mt are the main distinctive minerals of this stage. When compared to other Carajás IOCG deposits, K-Fe (Mt) alteration from the GT-34 deposit develops in a very similar way in terms of mineral assemblage. The main

difference is that at the GT-34 deposit, this alteration is poorly developed, while at the other IOCG deposits, it is one of the main alteration stages (e.g., Sossego).

Phlogopite is easily identified in hand sample (Figure 3.7 A), forming medium to coarse lamellae that overwrite any previous alteration stages. No evident texture associated with deformation zones forming lepidoblastic domains is observed. Talc occurs in a way similar to Phl but as narrower and less fuzzy veins forming a series of subparallel veining (Figure 3.7 B). Where Tlc veins cut the Ca alteration, fine actinolite (Act) needles may appear over previous Hbl fragments borders or completely replace it. In addition to the vein-like formation, Tlc may also appear as alteration patches (Figure 3.7 C) partially filled with Act.

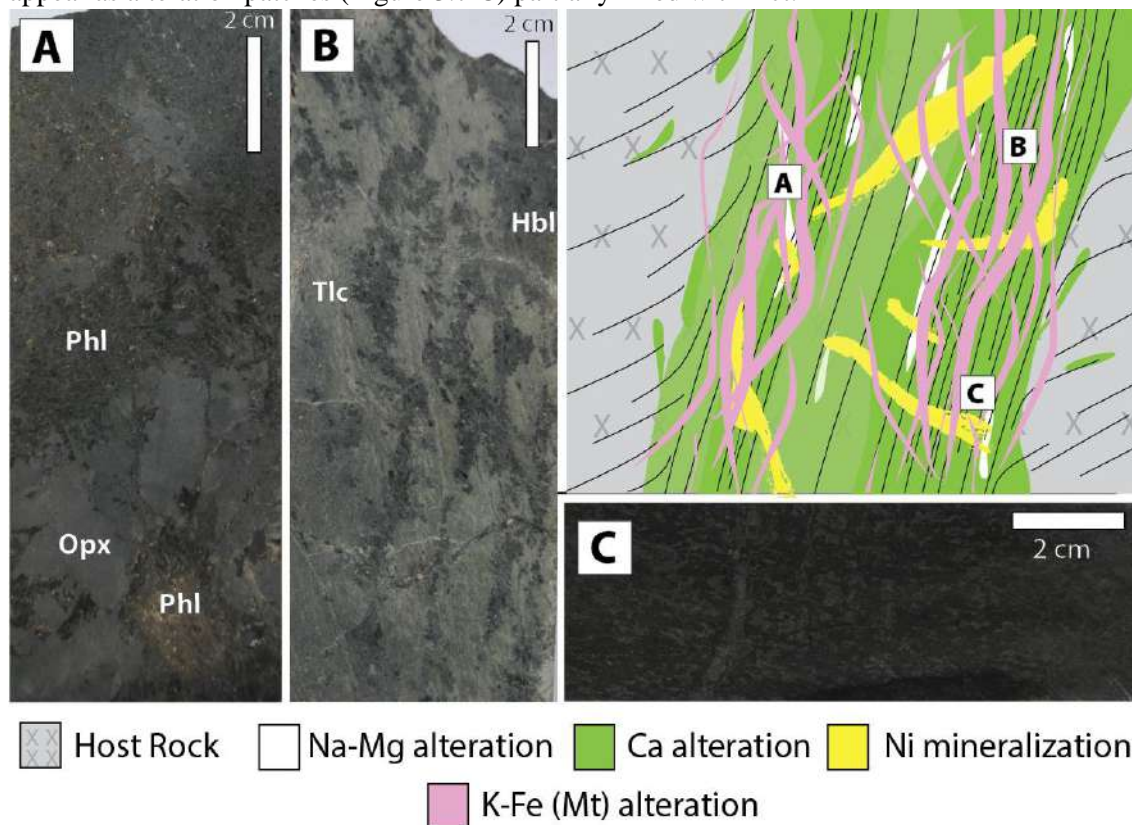


Figure 3.7 – Schematic representation of K-Fe (Mt) alteration. Samples are located within the scheme by the corresponding letters. A – Phlogopite formation with partially preserved fine to coarse Opx crystals. B – Irregular Tlc veins with Ca-alteration Hbl partially preserved. Very fine discordant Qtz-Chl-Ab veins displace K-Fe (Mt) alteration. C – Fine light gray pods to veins overprinting dark gray fine-grained Ca and Na-Mg alteration.

Magnetite forms with the first remobilization of the main nickel mineralization, forming local sharp millimetric veins (Figure 3.4 G). The Mt occurs when K-Fe (Mt) veins cut Ni sulfide-rich zones, forming fine Cpy-Po-Mt agglomerates mostly within Tlc (Figure 3.4 H) veins with local Py formation. Pentlandite fragments commonly appear within the Tlc veinlets as a result of mechanical transport. The first remobilization does not appear to produce significant economic amounts at the GT-34 deposit; however, it is important for understanding the system as whole.

Due to the fine and localized characteristics of K-Fe (Mt) alteration at GT-34, thin section observations are essential for its description. Contained in Phl, partially preserved Opx and Hbl rounded to angular fragments are present (Figure 3.8 A), with the former partially altered to Hbl and the latter partially altered to Phl. Phlogopite also forms fine lamellae associated with Tlc (Figure 3.8 B) that are recognized due to distinct Phl pleochroism. Within Tlc veins, Act needles (Figure 3.8 B, C) are highlighted due to the contrast in relief, with Act needles also occurring at the borders of Hbl fragments. Talc veins contain an elevated zircon concentration and fine subhedral Mt inclusions. Zircon crystals associated with this alteration were handpicked and dated.

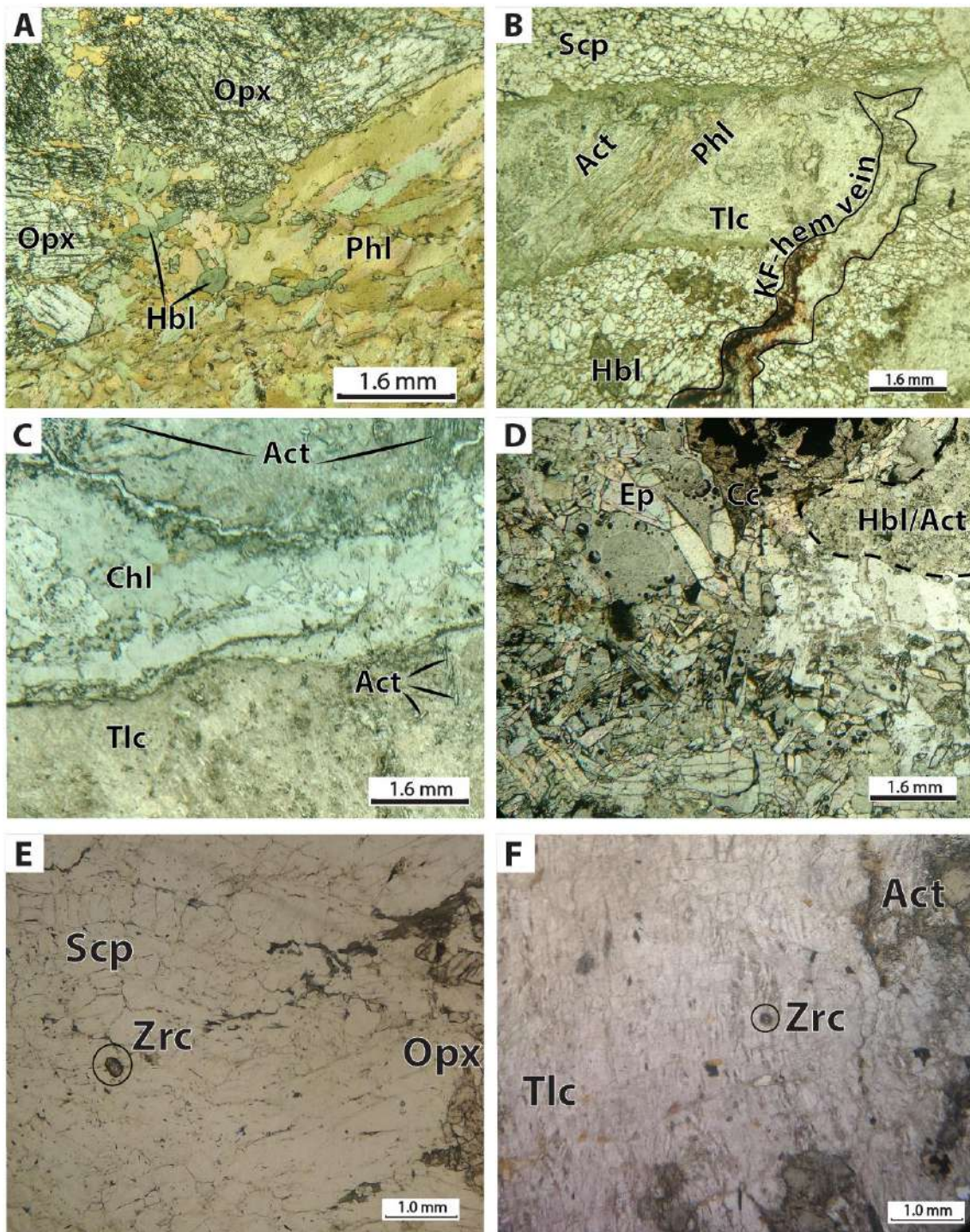


Figure 3.8 – Details of late-stage alteration zones and zircon crystals used for geochronology: A (K-Fe (Mt) alteration); B, C (K-Fe (Mt) and K-Fe (Hem) alteration); D (K-Fe (Hem) alteration); E (Na-Mg alteration zircons); F (K-Fe (Mt) alteration zircons). A – Phlogopite vein with fragments of Ca-alteration Hbl and overprinting Na-Mg alteration Opx. B – Scapolite overprinted by Ca-alteration Hbl. Talc veins with fine Act needles and Phl from K-Fe (Mt) alteration displace Na and Ca alteration. Red Kf vein with Chl from K-Fe (Hem) cutting previous alterations. C – Talc with Act needles from K-Fe (Mt) alteration cut by Chl-Qtz-Ab vein from late-stage K-Fe (Hem) alteration. D – Epidote rich with associated Cc. Dashed line marks the fragments from previous alterations. E – Zircon (Zrc) crystals associated with initial Na-Mg alteration. F – Zircon crystal associated with Tlc and Act with late-stage K-Fe (Mt) alteration.

3.6.6 K-Fe (Hem) alteration and second sulfide remobilization

This alteration is the last one identified at the GT-34 deposit, present as sharp limited irregular veins associated with characteristic brittle deformation. It occurs under even more

restricted conditions than K-Fe (Mt) alteration forming wide mineral assemblage. Typically, red Kf with associated Chl and CC (Figure 3.8 B; Figure 3.9 A) forms fine veinlets that crosscut previous alterations and partially preserve tonalite to granodiorite. Quartz-albite veins with Chl are also common (Figure 3.9 B) and are associated with the second sulfide remobilization. Albite is characteristic due to its red color marked by pervasive Hem inclusions (Figure 3.9 D), while Ep and Cc may locally fill the Qtz-Ab veins.

During the second remobilization, millerite (Mill) and Py are the dominant sulfides with galena (Gn) and sphalerite (Sph) present in trace amounts. Hydroxylapatite (ApOH) also occurs associated with Qtz-Ab veins and remobilized sulfides, chiefly Mill (Figure 3.9 C). The ApOH of this stage is significantly different from the ApCl of the main mineralization stage in terms of mineral assemblage, texture and chemistry. At this stage, ApOH is distinctively white and forms fine euhedral crystals, while at the main mineralization stage, the ApCl is fine to coarse with yellow to light gray colors and rounded crystals.

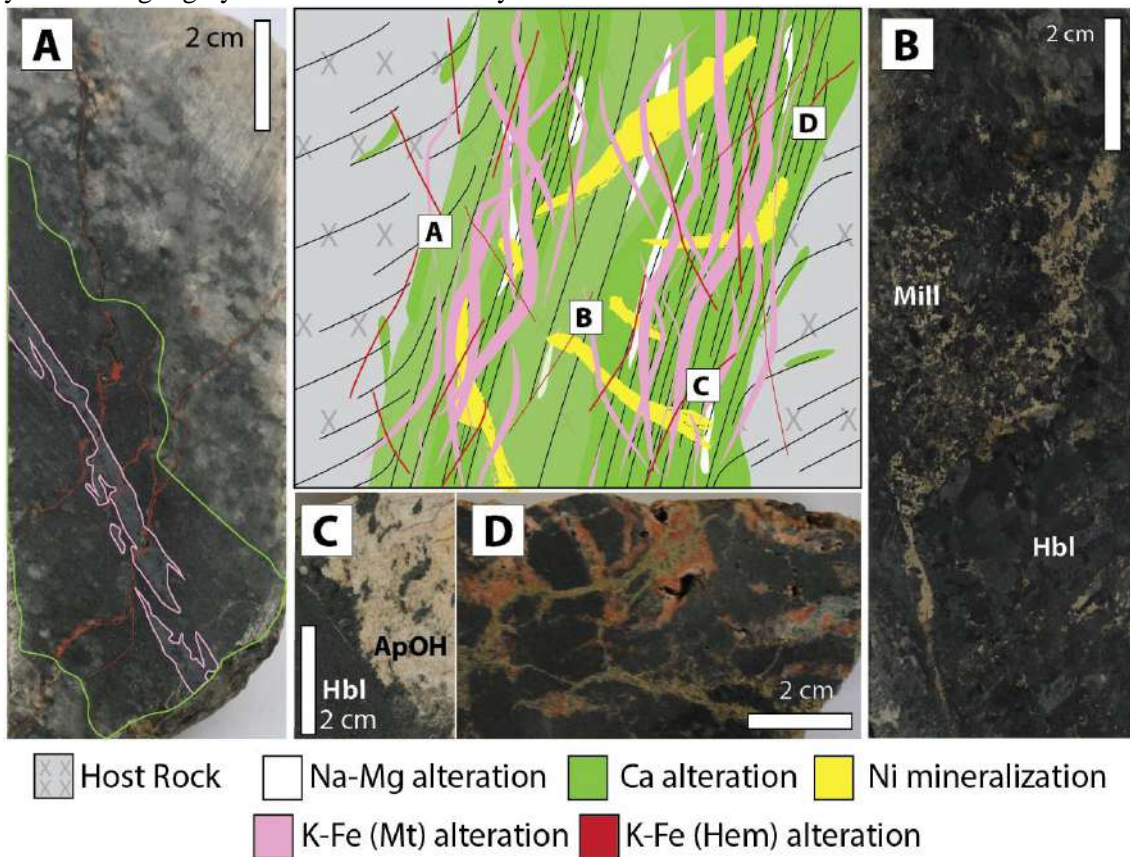


Figure 3.9 – Schematic representation of K-Fe (Hem) alteration. Samples are located within the scheme by the corresponding letters. A – Partially preserved host rock at top right. Dark gray mass represents fine-grained Na-Mg and Ca alteration (green lines). Light gray vein is from K-Fe (Mt) alteration forming Tlc with Act needles (pink lines). Fine, irregular black/red veins that displace all previous alteration are from K-Fe (Hem) alteration with red Kf and Chl. B – Remobilization of Ni mineralization precipitating as Mill during K-Fe (Hem) alteration cutting Ca alteration. C – Hydroxylapatite from K-Fe (Hem) alteration. D- Irregular veining from K-Fe (Hem) alteration with partially preserved fragments from Ca alteration.

Thin section study reveals that Chl forms at the borders of the veins with a comb-like texture (Figure 3.8 C) locally observed on Qtz and Ab. Inclusions, mostly Hem, inside Kf are distinctive under the microscope, giving the sample a fine dark red color (Figure 3.8 B). Epidote occurs as fine to medium euhedral crystals forming an adiablastic texture (Figure 3.8 D). Tourmaline inclusions are identified within Qtz-Ab, normally inside Qtz crystals forming fine needles that display distinct pleochroism.

A summary of all the alteration zones can be observed in Table 3.1. The mineralogy suggests a highly saline-CO₂ fluid that progressively becomes richer in H₂O content and lower in salinity.

Table 3.1– Progression of mineral parageneses observed for each alteration and Ni mineralization

Min.	Alt.	Na-Mg	Ca	Ni mineralization	K-Fe (Mt)	K-Fe (Hem)
Orthopyroxene		—				
Scapolite		—				
Hornblende			—			
Oligoclase			—			
Clinopyroxene			—			
Apatite				—		
Pentlandite				—	---	
Pyrrhotite				—		
Pyrite				—		—
Chalcopyrite						—
Sphalerite						---
Galene						---
Millerite						—
Phlogopite					—	
Talc					—	
Actinolite					—	
Magnetite		---		—		
K-feldspar						—
Chlorite						—
Calcite						—
Hematite						---
Epidote						—
Quartz						—
Albite						—
Fluid	H2O	—				
	CO2	—				—
	Cl	—				---
	F		---		—	

Main
 Local
 Trace

3.7 Mineral Chemistry

Mineral analyses conditions are in methodology section. Most representative results are summarized in (Table 3.2). The full dataset is available in Appendix 1.

Orthopyroxene: Fine to coarse Opx and partially preserved ones were analyzed. Calculations were made based on a total of 6 oxygens, revealing a Mg-dominant (En₆₈₋₇₆) and Ca-depleted (W_{O0.2-0.7}) composition ranging from hypersthene to bronzite. Low values were obtained for Al (0.19 to 1.08 wt%) with one outlier value of 2.09 wt%, Ti (≤ 0.1 wt%) and Cr (≤ 0.1 wt%). Small variations in the composition were not directly associated with partially preserved crystals or recrystallized ones.

Typical igneous Opx display different values for Ti, Cr, Ca and Al from the ones obtained for GT-34. When compared (Figure 3.10 A), the values range from as low as the ones found at the GT-34 deposit to values up to three times higher. The obtained contents (Ti, Cr, Ca, and Al) for GT-34 Opx are more like the ones obtained for incipient charnockite Opx despite the En%. These systematic low values are inconsistent with typical igneous Opx, suggesting that an alternative formation process was involved.

Table 3.2 – Most representative mineral chemistry analyses from the main minerals associated with each alteration.

Alteration	Na	Na	Ca	Ca	Ca	K-Fe (Mt)	K-Fe (Mt)	K-Fe (Mt)	Ni min.	K-Fe (Hem)
Mineral	Opx	Scp	Cpx	Mg-Hbl	Mg-Hst	Act	Tre	Phl	AptCl	ApOH
P2O5	n.a.	n.a.	n.a.	n.a.	n.a.	n.a.	n.a.	n.a.	41.84	42.61
SiO2	54.35	57.86	54.40	46.97	44.01	56.94	55.45	39.95	0.06	0.63
Al2O3	0.44	21.68	0.77	9.96	10.68	0.46	2.10	12.97	0.00	0.02
FeO	19.57	0.16	7.53	10.37	12.16	9.29	6.20	8.96	0.02	0.15
Cr2O3	0.00	0.00	0.00	0.02	0.06	0.00	0.05	0.00	0.00	0.06
TiO2	0.00	0.06	0.00	0.49	0.80	0.05	0.05	1.96	0.13	0.00
NiO	0.13	0.06	0.00	0.20	0.22	0.08	0.34	0.30	0.05	0.09
MnO	0.28	0.04	0.08	0.00	0.12	0.18	0.09	0.12	0.00	0.05
MgO	25.08	0.02	14.41	16.24	13.92	18.34	20.62	20.28	0.00	0.29
CaO	0.16	4.78	20.28	10.22	11.15	11.38	11.87	0.02	52.57	53.01
Na2O	0.03	11.06	0.69	2.38	2.38	0.10	0.50	0.18	0.08	0.07
K2O	0.02	0.79	0.06	0.62	0.90	0.06	0.13	8.99	0.00	0.00
Cl	0.00	3.48	0.00	0.66	1.06	0.05	0.13	0.83	6.66	2.11
F	0.00	0.00	0.00	1.08	0.96	0.00	0.53	2.05	0.05	0.02
SO3	n.a	n.a	n.a	n.a	n.a	n.a	n.a	n.a	0.04	0.08
V2O3	0.00	0.03	0.03	0.10	0.14	0.10	0.00	0.02	0.00	0.00
Total	100.05	100.02	98.25	98.70	97.91	97.02	98.66	95.57	99.99	98.69
P	n.a.	n.a.	n.a.	n.a.	n.a.	n.a.	n.a.	n.a.	6.09	6.06
Si	1.99	8.32	2.03	6.63	6.47	7.97	7.65	5.87	0.01	0.11
Al iv	0.01	3.67	-0.03	1.37	1.53	0.03	0.34	2.13	0.00	0.00
Al vi	0.01	n.	0.07	0.28	0.32	0.05	0.00	0.11	n.	n.
Fe iii	0.00	n.	0.00	1.13	0.67	0.52	0.68	n.	n.	n.
Cr	0.00	0.00	0.00	0.00	0.01	0.00	0.01	0.00	0.00	0.00
Ti	0.00	0.01	0.00	0.05	0.09	0.01	0.01	0.22	0.02	0.00
Fe ii	0.60	0.02	0.24	0.09	0.82	0.57	0.03	1.10	0.00	0.02
Mn	0.01	0.00	0.00	0.00	0.02	0.02	0.01	0.01	0.00	0.01
Mg	1.37	0.00	0.80	3.42	3.05	3.83	4.24	4.44	0.00	0.07
Ca	0.01	0.74	0.81	1.54	1.76	1.71	1.75	0.00	9.69	9.53
Na	0.00	3.08	0.05	0.65	0.68	0.03	0.13	0.05	0.03	0.02
K	0.00	0.15	0.00	0.11	0.17	0.01	0.02	1.68	0.00	0.00
Cl	n.	0.86	n.	0.16	0.26	0.01	0.03	0.21	1.94	0.60
F	n.	0.00	n.	0.48	0.45	0.00	0.23	0.95	0.01	0.00
OH*	n.	n.	n.	1.36	1.29	1.99	1.74	2.84	0.04	1.39
CO3*	n.	0.14	n.	n.	n.	n.	n.	n.	n.	n.
SO3	n.	0.00	n.	n.	n.	n.	n.	n.	0.00	0.00
total	4.00	16.99	3.98	17.31	17.60	16.74	16.91	19.66	17.84	17.82
	En % 69	Me% 19	En% 43							

* Calculated values for CO3 and OH; n.a. = not analysed; n. = null; abbreviations in the text

Scapolite: Coarse euhedral and granoblastic Scp were analyzed and displayed chemical homogeneity, dominantly of marialite composition (Me% 0.17 to 0.26). One outlier value displayed elevated Fe (2.21 wt%) and Mg (2.25 wt%) contents with increasing divalent cations and therefore a higher meionite (Me% 0.35) not directly associated with the presence of Ca. Calculations were made assuming a full T site (12 cations) normalization factor. The chlorine content obtained (3.02 to 3.83 wt%) practically fills the A site (0.77 to 0.96 apfu), with SO₃ content, when analyzed, not exceeding 0.1 wt%. Calculated CO₃ values were assumed to complete the remaining A-site vacancies. The anhydrous content, together with relative Mg-Fe present in Scp crystalline structure, are in agreement with conditions that would favor Opx formation, confirming this atypical mineral association.

Amphibole: Values obtained for amphiboles were calculated based on 23 oxygens and 13 cations, typical for calcic amphiboles. Although amphiboles are present in both Ca- and K-Fe (Mt) alterations, they are treated in the same topic for comparison purposes. During Ca alteration, amphibole compositions range from Mg-hornblende to Mg-hastingsite with a few tschermakite

and endenite members. On the other hand, K-Fe (Mt) amphiboles are of actinolite composition with minor tremolite and Mg-hornblende. In terms of chemical structure, the main differences are highlighted in Figure 3.10. Aluminum_{total} ($Al_{total} = Al^{iv} + Al^{vi}$) values are higher for amphiboles found within Ca alteration (1.10 to 2.37 apfu) than for amphiboles of the K-Fe (Mt) alteration (0.06 to 1.01 apfu) (Figure 3.10 C). Sodium and K also show significant differences, with higher values (> 0.5 apfu) found with Ca alteration and lower values (< 0.5 apfu) with K-Fe (Mt) (Figure 3.10 D) (Monteiro et al. 2008a).

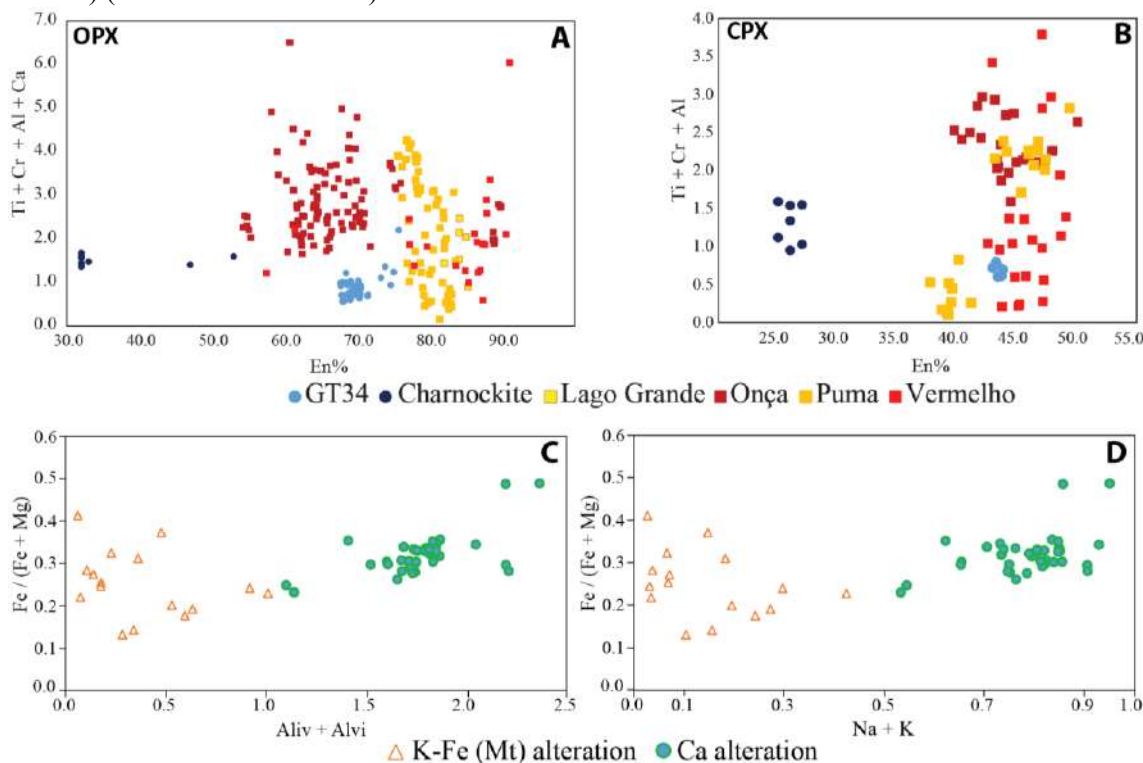


Figure 3.10 – Mineral chemistry compositional distribution. A – Opx from GT-34 compared with Opx from charnockites and typical igneous Opx. B – Cpx from GT-34 compared with Cpx from charnockites and typical igneous Cpx. C, D – Chemical comparison between Ca and K-Fe (Mt) alteration amphiboles. Total Fe = $Fe^{+3} + Fe^{+2}$. Data available from Rosa 2014; Teixeira et al. 2015; Yang et al. 2016; Siepierski 2016.

Another difference between amphiboles from Ca and K-Fe (Mt) alterations is the halogen content on the anionic site. Calcic-alteration amphiboles have higher halogens ($F + Cl = 0.35$ to 0.82 apfu). Comparison with K-Fe (Mt) alteration ($F + Cl = 0.00$ to 0.35 apfu) shows that the fluid phase and halogen content associated with each alteration were different, with Ca alteration amphiboles developing under more saline conditions.

Clinopyroxene: Analyses of punctual Cpx crystals reveal a composition of En_{43-44} and Wo_{44} . Similar to Opx crystals, Cpx also display low Al (0.55 to 0.77 wt %), Ti (≤ 0.1 wt%) and Cr (≤ 0.1 wt%). Low values such as these are also not common for igneous/metamorphic Cpx, suggesting that another crystallization process was involved. The similarity found with EPMA results does not necessary mean Cpx is chemically homogeneous due to restricted sampling and analyses. The difference observed in the Opx (En_{68-76}) and Cpx (En_{43-44}) enstatite reveals that these pyroxenes formed under different conditions.

Similar to the Opx values, GT-34 Cpx also display low values for Ti, Cr and Al when compared with igneous Cpx (Figure 3.10 B). Igneous Cpx may display contents > 2.0 (Ti + Cr + Al), while GT-34 Cpx values are < 1.0 . Charnockite values are also < 2.0 and approximate the GT-34 Cpx despite the En%.

Plagioclase: The composition of metasomatic plagioclase ranges from An_{15-48} (oligoclase to andesine). Oligoclase is dominant and more commonly present, normally associated with Scp

borders. Andesine occurs as isolated grains limited mostly by Mg-hornblende and does not show a direct relationship with Scp as oligoclase does.

Phlogopite: The phlogopite calculations were made based on 24 anions (O, OH, F, and Cl). Ratios obtained for Fe/(Fe+Mg) are low (0.165 to 0.241), showing a high Mg content corresponding to Phl classification. Aluminum_{total} ($Al_{total} = Al^{iv} + Al^{vi}$) values range from 2.129 to 2.390, with Al^{vi} up to 0.241 apfu, showing relatively small substitution in the tetrahedral-octahedral positions.

Fluorine predominantly represents halogen content (up to 1.07 apfu), while the presence of Cl is significantly lower (up to 0.26 apfu). The values obtained for Phl halogen content are similar to K-Fe (Mt) amphibole halogen content (up to 31 mol% of A site for Phl; up to 22 mol% of A site for K-Fe (Mt) amphiboles).

Apatite: Analyses were conducted on apatites associated with the Ni mineralization and with the later remobilization. Calculations were made assuming 25 oxygens. The data revealed that the P₂O₅ values range from 40.17 to 43.62 wt% with CaO ranging from 50.27 to 54.99 wt%. The anionic content suggests two main apatite populations differing between ApCl and ApOH (Figure 3.11).

Chlorapatite grains are yellowish white and may display up to 6.94 wt% Cl, showing an elevated Cl content, and are directly associated with the Ni mineralization. The irregular zonation is linked with the Cl and H₂O content. Where the Cl content is elevated, the apatite displays a light gray interference color, and where the H₂O content is elevated, the apatite displays a dark gray interference color.

Hydroxylapatite crystals are associated with the ApCl zonation and with the late low-temperature later hydrothermal alterations. They typically present a white color without any evidence for distinct zonation. The composition may be up to 1.83 calculated OH with 0.08 Cl and F apfu. Small variations in the OH and F content may be observed where the F content reaches up to 3.02 wt%.

Compositional maps were obtained for both ApOH and ApCl using the EPMA. The irregular zonation can be observed in terms of Cl and F content. Hydroxyl values are elevated where both F and Cl are low. Elevated Cl content associated with the Ni mineralization is usually cut by F and OH fractures causing the irregular zonation (Figure 3.11, left side). This local change causes the compositional range from Cl to OH observed in the triangular plot for the Ni mineralization apatite (Figure 3.11).

Unlike the Ni mineralization apatite, the low-temperature apatite displays a weak regular compositional zonation (Figure 3.11, right side) with low values for F and Cl. Predominantly, the values display elevated OH content showing the presence of ApOH.

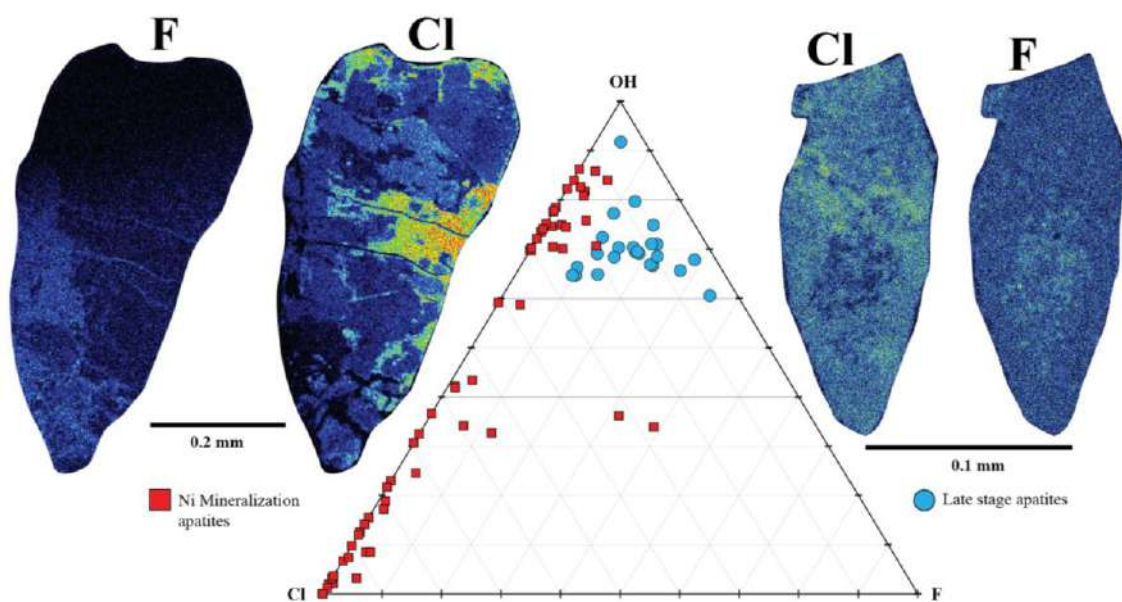


Figure 3.11 – Different apatite populations. Red squares are associated with the main Ni mineralization. Blue circles are associated with late low-temperature remobilization. Compositional maps are shown on the left (red square) and right side (blue circle) of the image. Compositional maps vary from cold to hot colors, where cold colors show low content and hot colors show elevated content.

3.8 Geochronology

Uranium-Pb analyses procedures are detailed in methodology section. Supplementary tables are provided in Appendix 2.

Sample 3A corresponds to the initial Na-Mg alteration with partially preserved host rock. Two distinct zircon populations were recovered from this sample. Both populations displayed similar external features such as a subhedral, bypyramidal prismatic habit. Under Cathodoluminescence (CL) imaging, the first zircon population shows composite internal structures, with oscillatory zoned cores overgrown by a bright, irregularly textured rim, which evidences features typical of fluid-rock interaction (coupled dissolution-precipitation process), such as convolute, inward resorption gulfs and ghost zoning (Figure 3.12). Uranium-Pb data of the first population resulted in concordant to highly discordant individual ages. One single core age of 3.056 ± 7 Ga was obtained. Four concordant dates obtained in rims yield a Concordia age of 2.828 ± 4 Ga (MSWD=0.13, Figure 3.12 A), which is interpreted as the host rock crystallization age.

The second zircon population recovered from sample 3A (Figure 3.8 E) exhibit extremely complex internal textures without clear core-rim correlation typical of metasomatic reactions (Figure 3.12). Analyses of these zircon crystals yielded discordant ages (2.731 ± 4 to 2.694 ± 20 Ga).

Sample 11B corresponds to the late-stage K-Fe (Mt) alteration (Figure 3.8 F). Zircon crystals show similar external features to that observed in sample 3A, forming bypyramidal prims. Internal textures, however, are extremely complex and suggests a pervasive transformation throughout a fluid-rock interaction (Figure 3.12), similar to the second zircon population obtained for sample 3A. No core-rim relation can be clearly defined in such grains. Individual U-Pb ages vary from concordant to highly discordant; usually, dates obtained in the inner parts are older than in outer zones, but results aling in a Pb-loss discordia upper-intercept pointing towards c.a. 2.739 ± 21 Ga (Figure 3.12 B). Four zircon grains render a Concordia age of 2.724 ± 4 Ga (MSWD=1.2, Figure 3.12 C), which is interpreted as the time of fluid-rich interaction and disturbance of zircon grains, which promoted the reset of the original U-Pb isotopic signature.

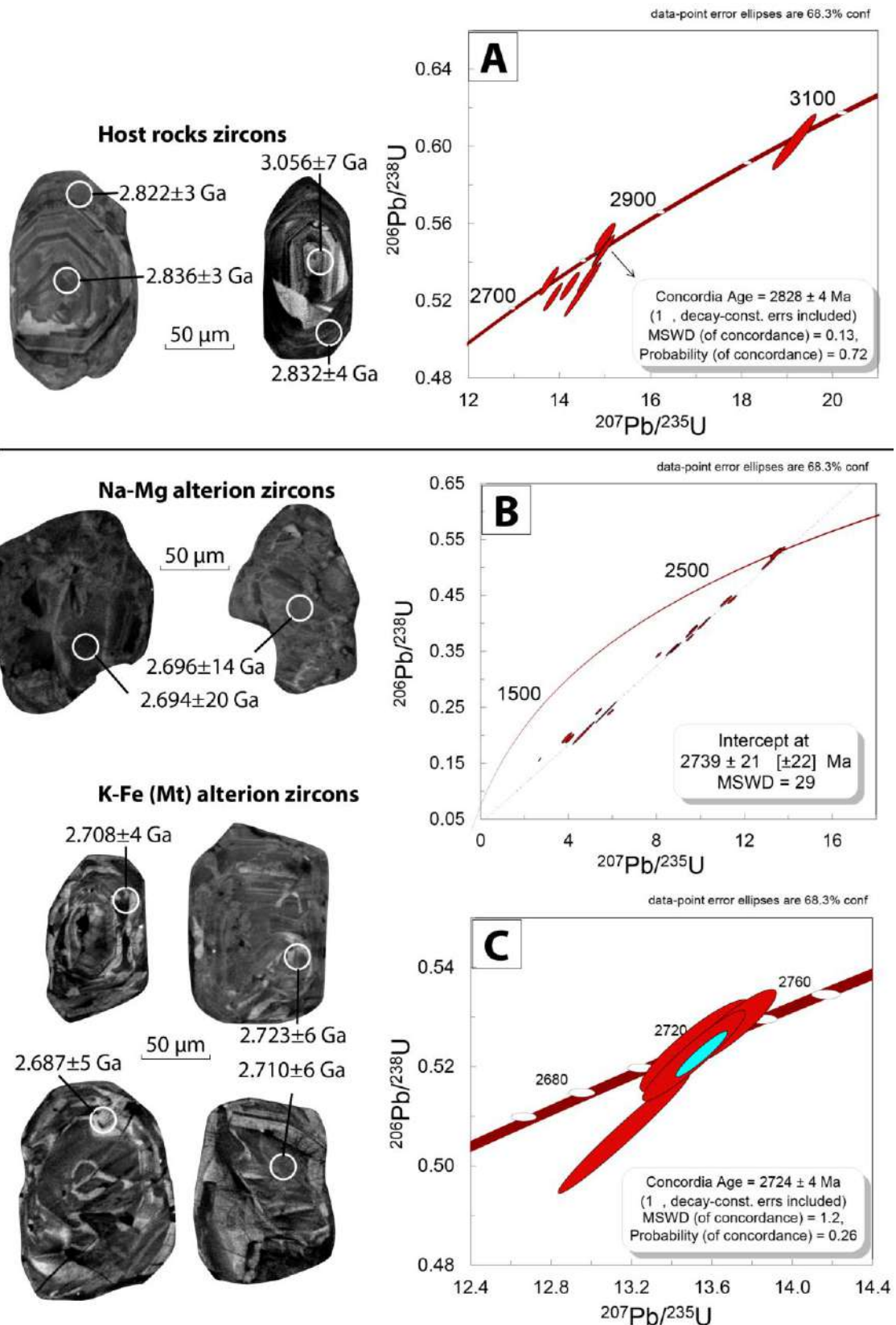


Figure 3.12 – Summarized geochronology obtained for this study. Zircons obtained from host rocks display typical regular igneous zoning. Zircons obtained from alteration zones display irregular zoning characteristic of metasomatism. A – Concordant ages obtained for the host rocks from igneous zircons. B – Discordant age obtained from metasomatic zircons. C – Concordant age obtained from metasomatic zircons.

3.9 Discussion

3.9.1 GT-34 and the IOCG system

Iron-oxide-copper-gold systems are known today as widely variable deposits marked by pervasive Fe-alkali metasomatism (Porter, 2010). Several studies (Hitzman et al., 1992; Williams et al., 2005; Groves et al., 2010; Xavier et al., 2010; Barton, 2014) have identified characteristics that cluster deposits within this particularly variable group. Some of the main characteristics are: (1) hydrothermal properties with marked structural control and breccias; (2) abundant low-Ti Fe oxides and Fe silicates; (3) temporal relations with magmatism but not direct relations such as porphyry style; (4) LREE and polymetallic enrichment; (5) involvement of complex highly saline, aqueous and carbonic fluids; and (6) economic Cu-Au concentrations.

Considering the *sensu stricto* IOCG definition (Groves et al., 2010), the GT-34 deposit may apparently not fit because Cu and Au are subeconomic. However, other corroborating evidence exists and suggests that the GT-34 deposit represents the deeper part of an IOCG system. The GT-34 deposit formed along a NE-trending shear zone with pervasive Fe-alkali alteration zones, denoting the strong structural control and metasomatism characteristic of an IOCG system. Rounded fragmental breccias are the main mineralization type and occur in similar textural relationship to proximal deposits.

Titanium concentrations are low in both Fe silicates and Fe oxides found at GT-34, which is one of the most distinguishing features. The abundant iron oxides (>10%) expected for classical IOCG deposits are present in smaller amounts at GT-34. Crystallization of Pn-Po-Py provides evidence for a high fS_2 that forms associated with spaced Mt. During late-stage alterations (K-Fe (Mt) and K-Fe (Hem)), iron oxide occurs in the expected proportion as a partial remobilization of the Ni mineralization.

Another feature of the GT-34 deposit that is similar to IOCG systems is the LREE and polymetallic enrichment. Siepinski (2008) observed a relative enrichment in LREE associated with Ni mineralization, following the geochemical pattern observed for several IOCG deposits. The polymetallic feature is the main characteristic of the GT-34 deposit, with Ni representing the main metal. Copper, Au, Pd, Te and Ag are the most common metals present in Pn-Po-Py-Cpy crystalline structures.

Nickel is recurrent among different IOCG provinces (e.g., Eloise and Mt. Elliot, Cloncurry district, Australia – Williams and Pollard, 2003; Terra, Norrex and Silver Bear, Great Bear Magmatic Zone, Canada – Corriveau et al., 2016; Tocopilla, Gatico and Tamaya, Central Andes – Sillitoe, 2003). In the Carajás Domain, Ni-rich horizons are also recognized at the Castanha deposit (Pestilho, 2011), Jatobá (Veloso et al., 2016) and at the Jaguar deposit (Ferraz, 2016). The presence of Ni in GT-34 and the other deposits highlights the polymetallic enrichment characteristic of IOCG systems.

Despite the unusual alteration assemblage and the lack of economic Cu-Au as the main commodity, most processes that occur in IOCG systems were also present in the GT-34 deposit. The wide presence of satellite deposits, including the nearby classic IOCG Sequerinho-Sossego orebodies (e.g., Castanha, Bacaba, Jatobá), points toward GT-34 representing one more of these deposits. The main difference relies on the highest P-T conditions, placing GT-34 as possibly the deepest IOCG occurrence reported to date (**Erro! Fonte de referência não encontrada.**).

Additionally, geochronology data obtained in this study yielded ages concordant with the Neoproterozoic IOCG mineralization (2.72–2.68 Ga) expected for the Southern copper belt (Moreto et al. 2015a, 2015b). Ages obtained in this study from metamictic zircon crystals (Figure 3.12) recovered from pre-Ni mineralization (Na-Mg alteration) and post-Ni mineralization (K-Fe (Mt) alteration) support a Neoproterozoic formation for the GT-34 deposit at 2.724 ± 4 Ga. The age constrains suggest that the Neoproterozoic IOCG mineralizing process were present at the GT-34 deposit corroborating that the referred deposit is indeed part of the IOCG system. The Pb loss and ages pointing toward ca. 2.70 Ga (Figure 3.12 A) also suggest a Neoproterozoic tectono-thermal disturbance in the system that may be caused by either the widespread Neoproterozoic magmatism or the IOCG mineralization system.

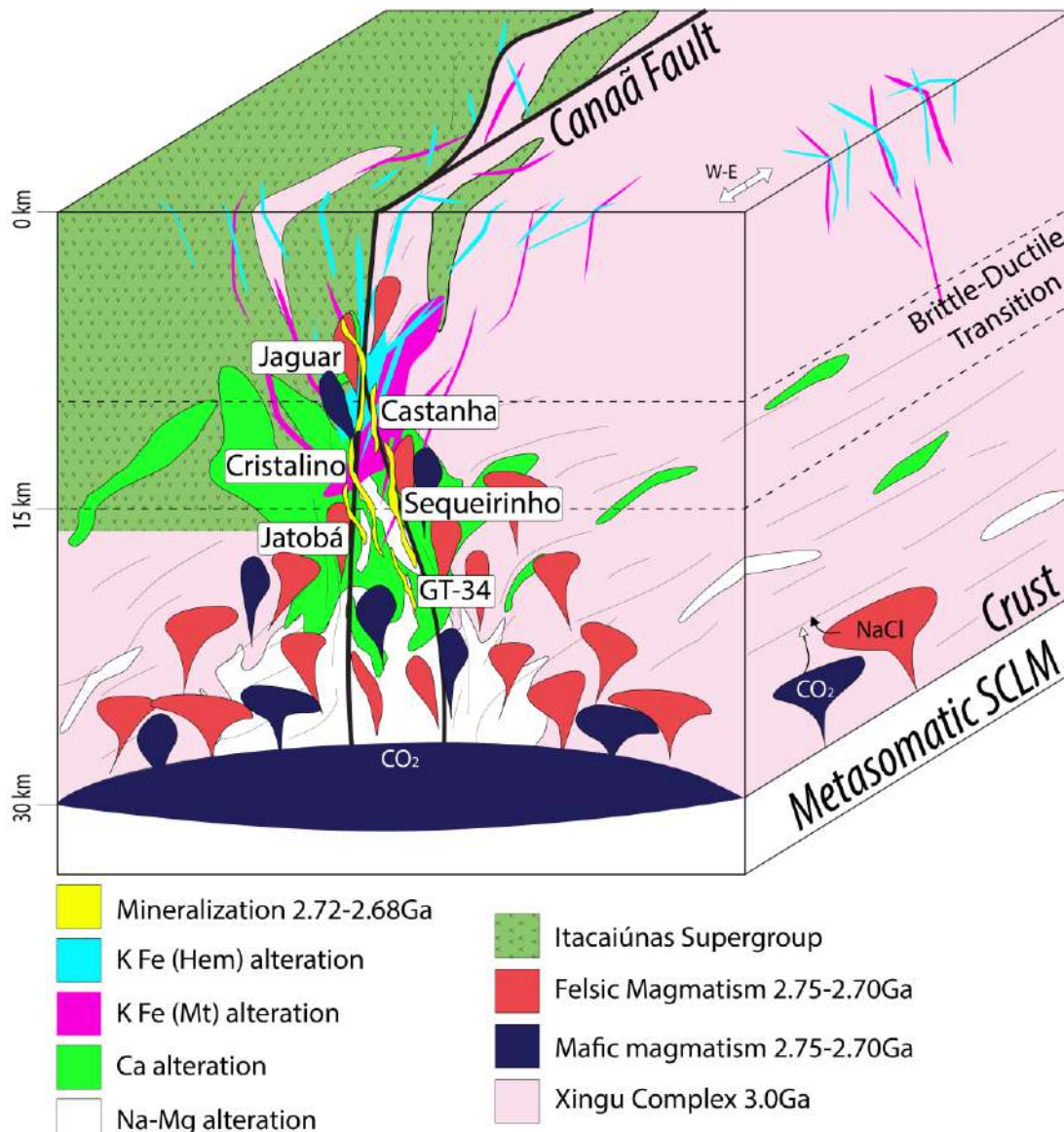


Figure 3.13 – Schematic representation for the Carajás IOCG system. Transcrustal shear zones (Canaã fault) channelize the magmatic and mantellic fluids. Deposits are locally controlled by the regional shearing. Alteration zones extend far away from the deposit locations. .

3.9.2 Orthopyroxene formation

The unique Opx presence in the GT-34 deposit alteration makes it a singular example for IOCG systems worldwide (Hitzman et al., 1992; Hitzman, 2000; Williams et al., 2005; Corriveau et al., 2010; Xavier et al., 2010; Corriveau et al., 2016). Initial discussion concerning Opx formation at the GT-34 deposit (Siepierski, 2008) suggested its metasomatic origin at temperatures $>700^{\circ}\text{C}$ and pressures >0.5 kbar. The individualization of Opx-Scp parageneses was recently proposed as a result of an immiscible CO_2 -NaCl high-temperature fluid with low $a_{\text{H}_2\text{O}}$ (Garcia et al., 2017). Further considerations regarding Opx formation and fluid are detailed here.

Orthopyroxene is normally associated with igneous and high-grade metamorphic terranes. Charnockites are Opx- or fayalite-bearing (Frost and Forst, 2008) granitic rocks and represent more uncommon examples of Opx-bearing rocks. The origin of charnockites remains controversial and is polarized as fluid-induced and fluid-absent (Rajesh et al., 2013; Harlov et al., 2014; Newton and Tsunogae, 2014; references therein), the former associated with low- H_2O activity fluids and the latter with partial melting. Fluid-induced are typically dominated by CO_2 with a saline component (KCl, NaCl) and $a_{\text{H}_2\text{O}}$ not higher than 0.5 (Perchuk et al., 2000; Newton and Tsunogae, 2014). These fluids may cause solid-state dehydration of Garnet, Bt and Hbl

(metamorphic charnockite), and/or the fluid may change the original chemical composition of the former rock via a metasomatic reaction (Perchuk et al., 2000; Newton and Tsunogae, 2014).

In addition to Opx, other minerals are commonly associated with charnockites, such as Cpx, Plg and Kf. At GT-34, none of these are observed in equilibrium with Opx; instead, Scp is present with Opx. Although the exact same paragenesis (Opx-Scp) has not been observed, immiscible CO₂-NaCl fluids have been associated with Opx formation for fluid-induced charnockites (Perchuk and Gerya 1993; Touret and Huizenga 1999). Saline fluids (NaCl-rich) may also be associated with Scp formation while the high a_{CO_2} would provide anhydrous conditions for Opx stability. Such fluids may therefore be associated with the initial GT-34 Na-Mg alteration (Opx-Scp) in a manner similar to the fluid-induced formation of metasomatic charnockites.

GT-34 textures suggest that Opx is of metasomatic origin and crystallized together with Scp. The mineral chemistry results reveal that Opx displays low Al, Ca, Ti and Cr when compared with igneous and metamorphic Opx. However, when compared to fluid-induced charnockites, or incipient charnockites, Opx mineral chemistry (e.g., Rajesh et al. 2013; Yang et al. 2016) is similarly low in Al, Ca, Ti and Cr values despite the difference in the En%. The similarity between GT-34 deposit Opx and fluid-induced charnockite Opx chemistry may support a metasomatic origin. The difference in the En content is considered a result of the initial $X_{\text{Fe-Mg}}$ conditions and the fluid a_{CO_2} (Mg⁺ transport). In addition, primary Hbl and Bt were identified in the GT-34 host rock. Typical fluid-induced charnockites may form by the solid-state dehydration of mafic minerals (Harlov et al. 2014), forming Opx from previous hydrated phases such as Hbl and Bt. Therefore, the dehydration of Hbl and Bt from GT-34 host rock induced by the immiscible CO₂-NaCl high-temperature fluid could also form the GT-34 Opx without the need of adding Fe and/or Mg.

Scapolite chemistry reveals a dominant marialite composition and the presence of Fe and Mg during its formation. Meionite content (Me% 0.17) and the elevated Cl (up to 3.83 wt%) suggest that Scp formed under a NaCl-rich fluid (Mora and Valley, 1989). The crystallization of hydrothermal Scp is associated with deep systems at > 500°C (Vanko and Bishop, 1982). Scapolite stability within NaCl-rich fluids has been experimentally studied (Vanko and Bishop, 1982; Newton et al., 1998), revealing that at 800°C and 7-10 kbar, Scp is not stable, and plagioclase forms instead. Nevertheless, at 750°C and 1 kbar, plagioclase gives place to marialite. Marialite preferentially forms under elevated NaCl activity, and the rapid decrease in NaCl activity at pressures >4 kbar favors Plg formation but does not rule out Scp. Based on these experimental results, Na-Mg alteration must have developed at pressures <7 kbar. The Scp A site also provides indirect evidence for the presence of CO₂, since Cl and SO₃ do not completely fill the anionic sites, requiring CO₂ to be involved.

The absence of quartz during the initial Na-Mg alteration paragenesis may also suggest the pressure conditions under which the alteration developed. Manning and Aranovich (2014) experimentally demonstrated that Qtz becomes unstable in the presence of NaCl fluids at pressures >5 kbar and temperatures >700°C. Considering that the host rock originally had Qtz and no Qtz is observed in association with the Na-Mg alteration, it seems reasonable that the pressure was probably > 5 kbar.

The relatively simple mineral assemblage (Opx-Scp) suggests a fluid-buffered reaction. Fluid-buffered reactions form minerals that may be representative of fluid compositions. Based on textural relations and mineral chemistry, the Scp-Opx may reflect the fluid composition, revealing an immiscible NaCl – CO₂ high-temperature fluid.

3.9.3 Proximal charnockites

The presence of charnockites in the proximity of the GT-34 deposit may raise questions concerning how extensive the process suggested here in fact was. The formerly named Pium complex, now the Pium diopside norite (Araújo and Maia, 1991; Pidgeon et al., 2000; Ricci and Carvalho, 2006; Santos and Oliveira, 2010; Feio et al., 2012), consists of norite-gabbro elongate bodies with associated charnockites. With the introduction of GT-34 metasomatic Opx, a review of the Opx formation process is necessary.

The Pium complex was originally interpreted as mafic granulites; however, Ricci and Carvalho (2006) verified that they actually represent gabbros with charnockite affinity. Field relations show that gabbro and norite are found as partially preserved enclaves and angular fragments within quartz-Opx charnockites. Controversial obtained ages associated with the protolith, metamorphism and charnockite formation are 3002 ± 14 Ma, 2859 ± 9 Ma (U-Pb, Pidgeon et al., 2000) and 2735 ± 5 Ma (U-Pb, Feio et al., 2012), respectively.

An igneous origin for the charnockites has been proposed (Feio et al., 2012) as a result of partial melting of granulitic mafic crust caused by underplating of mafic magma, based on Frost and Frost (2008). Igneous (or fluid-absent) charnockites tend to be larger than fluid-induced ones, which occur at a localized scale. Although the two types are different, they may be spatially associated since charnockitic magmas can provide CO₂-rich fluids for fluid-induced charnockites. Furthermore, the mafic underplating suggested could also provide CO₂-rich fluids that contribute to fluid-induced charnockites.

Therefore, a CO₂ fluid source for GT-34 is regionally available, supporting its metasomatic origin. Fluids rich in CO₂ could have been channelized by regional transcrustal structures widely present in the Carajás Domain. Another plausible CO₂ source may be invoked as a mantle decarbonation process (Santosh and Omori, 2008). This process essentially calls upon the release of CO₂ from the mantle to explain ultrahigh-temperature rocks and incipient charnockite formation. The temperature predicted for the CO₂ release lies between 700 and 900°C under pressures of 10-13 kbar, leading to Opx along with spinel and manegsite formation. The CO₂ released by this process could also be channelized by regional structures providing CO₂ for the metasomatic system.

3.9.4 Different amphibole-bearing alterations

Amphiboles are widely present in Carajás Domain deposits (Gomes and Lindenmayer, 2003; Dreher, 2004; Monteiro et al., 2008a; Xavier et al., 2010; Pestilho 2011; Craveiro et al., 2012; de Melo et al., 2016), with their formation normally associated with the Na-Ca alteration defined by Monteiro et al. (2008b). The Na-Ca alteration appears as partially preserved fragments overprinted by the subsequent K-alteration, chloritization-carbonatization and Cu-Au mineralization. Monteiro et al. (2008a) initially studied the mineral chemistry and suggested that the Na-Ca alteration was divided in two different stages.

Unlike the main IOCG deposits in the Carajás Domain, the main alteration stage of the GT-34 deposit developed in a deeper part of the system formed under higher P-T conditions. Thus, initial alterations that are only partially preserved in other associated deposits can be observed in further detail at GT-34. Differences regarding parageneses, shape and mineral chemistry are used to distinguish between the two amphibole-bearing alterations.

One of the main differences between the Ca-alteration amphibole and the K-alteration amphibole lies in the paragenetic association. The former occur as Hbl-Plg-Cpx, while the latter occur as Act-Phl-Tlc-Mt. However, the complete parageneses are hardly ever found together, which may lead to misinterpretations if only this aspect is taken into consideration.

Considering the shape of the alteration, Ca alteration occurs as a widespread well developed alteration with localized narrow sharp veins cutting the Na-Mg-alteration. On the other hand, K-Fe (Mt) appears as restricted veins and veinlets with fuzzy boundaries. The systematic individualization of the amphiboles in different parageneses and alteration shapes is also observed in the mineral chemistry results.

Amphibole chemistry results are similar to the ones available at the literature (Monteiro et al., 2008a and references therein; Figure 3.10 A, B). The grains formed during the Ca alteration are more aluminous (up to 2.37 apfu) and alkaline (> 0.5 Na+K apfu), while K-Fe (Mt) alteration amphiboles are less aluminous (up to 1.0 apfu) and less alkaline (< 0.5 Na+K apfu). The different halogen contents also reveal that these amphiboles formed under distinct conditions.

The alteration progression observed at GT-34 shows that the Ca alteration occurs before the K-Fe (Mt) alteration, similar to the sequence previously determined at other deposits. Consequently, Ca was already present in the system when the K-Fe (Mt) alteration developed. Hence, amphiboles could form during K-Fe (Mt) alteration by partially reworking the previous

Ca alteration, without needing to add Ca to the system twice. Partial reworking is evident by the presence of K-Fe (Mt) alteration amphiboles chiefly on the borders of Ca-alteration amphiboles. The initial division of these different amphiboles into two Na-Ca alteration stages (Monteiro et al., 2008a) is therefore not necessary for the GT-34 deposit since a progressive reworking of the system can also form them.

Previously, formation conditions were defined as 481 to $547 \pm 75^\circ\text{C}$ at 5 kbar (Monterio et al., 2008a) using a Hbl-Plg thermometer (Holland and Blundy, 1994). A later refinement of the results considering Ab, Act/Mg-Hbl, titanite, Ep, Qtz and Cc suggested 500°C and 1.4 kbar. Conditions initially obtained using the Hbl-Plg thermometer (481 to $547 \pm 75^\circ\text{C}$ at 5 kbar) indicate formation under amphibolite conditions. With the individualization of the GT-34 deposit Opx-bearing Na-Mg alteration, not only an initial new alteration became recognized but also concurring evidence that the Carajás Domain IOCG system formed at even higher P-T conditions. Sodic-magnesium alteration conditions are predicted as 5 - 7 kbar and $>700^\circ\text{C}$ based on the defined parageneses and existing experimental results. The conditions defined at GT-34 show that the Carajás Domain IOCG system developed at even higher P-T conditions than previously expected, with the GT-34 deposit representing the deepest alteration zone so far documented in the Carajás Domain.

3.9.5 Fluid source

The Carajás Domain IOCG fluid source and genetic model have been continually discussed (Hitzman, 2000; Williams et al., 2005; Xavier et al., 2010; Groves et al., 2010; Barton et al., 2014; Montreuil et al., 2016). Fluid sources and formation dynamics for IOCG deposits are still controversial and explained by multiple hypotheses: (1) Magmatic fluids and metals (Perring et al., 2000; Pollard, 2001); (2) Basinal fluids and crustal metal leaching controlled by magmatic heat (Barton and Johnson, 1996); (3) Mixing of magmatic and non-magmatic fluids (Williams et al., 2001); and (4) Basinal-metamorphic driven (Hunt et al., 2005) or purely immiscible magmatic fluids (Tornos et al., 2016). For the Carajás Domain IOCG deposits, evaporitic brines are commonly invoked (Xavier et al., 2010 and references therein), although no direct evidence for Archean evaporites exists.

The GT-34 deposit initial association (Scp-Opx) indicates high temperature ($>700^\circ\text{C}$) and pressure up to 7 kbar forming in the presence of an immiscible CO_2 -NaCl fluid. Under conditions of high-grade terranes similar to the ones calculated for GT-34, evaporitic brines are hardly preserved (Manning and Aranovich, 2014). This situation implies that even if an evaporitic CO_2 -NaCl fluid existed, it would not be present at the expected conditions. More likely, mantle-derived magmas feed fluids for this system under such conditions. The elevated saline content may originate from felsic magmatism, which is abundant in the Carajás Domain. Calculations and theoretical proof of magmatic saline fluid production (Perring et al., 2000; Pollard, 2001) were made for the Australian Cloncurry district and may also be applied to the Carajás Domain.

Mafic magmas have high solubilities for Cl and CO_2 , which are preferentially extracted during magmatic degassing (Stopler et al., 1987; Webster and Holloway, 1988; Pollard, 2001; Webster et al., 2002; Webster, 2004) and may also contribute to fluid sources, bearing in mind the characteristic bimodal magmatism in the Carajás Domain. The initial extraction of CO_2 relative to H_2O (Lowenstern, 2001) supports the circumstances expected for the stabilization of the initial atypical Opx-Scp alteration. The presence of a vapor phase (CO_2) would also increase the diffusion rate, favoring the formation of coarser crystals as observed for localized Opx. The CO_2 may also be sourced from mantellic degassing as proposed by Santosh and Omori (2008). The mixing of multiple CO_2 and saline sources is fundamental for IOCG development.

Furthermore, the presence of Ni as the main commodity typically requires mafic-ultramafic magmas or host rocks. Although proximal small gabbroic occurrences are present, they have not been identified as host rocks. Leaching of these mafic-ultramafic (Xavier et al., 2010) bodies could only partially account for the Ni present at GT-34 due to their restricted size. Therefore, mafic-ultramafic magmas would be necessary to provide enough metal and possibly to source CO_2 as well.

The critical point regards the Ni mobility. Experimental studies on Ni mobility/transport are scarce (Liu et al., 2012; Tian et al., 2012 and references therein) and realized under much lower temperature conditions (< 400°C) than expected for GT-34. Relatively low mobility was observed with Cl ligands for the experimental conditions. At higher temperature, Ni mobility remains unknown experimentally. Although experimental studies provide no support, GT-34 shows indirect evidence for elevated Cl presence (chlorapatite; Siepierski, 2008) in fluids associated with Ni mineralization.

Further, textural evidence supports the interpretation that Ni-bearing phases at GT-34 were formed at high temperature, similar to what is observed at mafic-ultramafic deposits (Naldrett, 2004) where Po-Pn are the dominant sulfides. Comparatively, different sulfide associations form hydrothermal nickel deposits. Millerite, bravoite, vaesite and gersdorffite are the sulfides that are chiefly associated with hydrothermal nickel deposits (González-Álvarez et al., 2013). This difference could imply that Ni at GT-34 was not transported with complexants, but alternatively, Ni could also move as an immiscible sulfide liquid carried by passing high-temperature (>700°C) hydrothermal fluids, which would explain the textures described.

Contrasting the proposed initial magmatic conditions, late-stage K-Fe (Mt) and K-Fe (Hem) conditions are not well constrained. Existing studies support basinal hydrothermal formation, although evidence found here is suggestive of a magmatic origin. Evidence currently available is still ambiguous, and late-stage (K-Fe (Mt) and K-Fe (Hem)) alterations in the GT-34 deposit remain controversial and are probably a result of mixed sources (Xavier et al., 2008; Monteiro 2008b). Remobilization associated with Paleoproterozoic A-type granites could also account for these alterations, as observed at Alvo 118 and Sossego (Moreto et al., 2015a).

The characteristics described for GT-34 deposit fluids display an initial carbonic saline content of magmatic origin (Garcia et al., 2017) with a progressively increasing aqueous component. The progress from a deep to a shallow IOCG system could enable marine to meteoric waters to mix with initial magmatic fluids.

3.10 Conclusions

1. Processes associated with classic IOCG deposits were also present at the GT-34 deposit (e.g., alkali-Fe alteration, strong structural control, low-Ti Fe oxides). Although Cu-Au are subeconomic, they are still present, implying that the GT-34 deposit is indeed part of the IOCG system.
2. Pressure–temperature conditions defined for the initial Na-Mg alteration (Opx-Scp) suggest $T > 700^{\circ}\text{C}$ and P 5–7 kbar. These conditions raise the temperature at least 200°C from those previously defined (5 kbar – 500°C) and pressure up to 2 kbar higher. Such parameters indicate that the GT-34 deposit is the deepest IOCG occurrence in the Carajás Domain.
3. The Carajás Domain displays a continuum of IOCG occurrences at different crustal levels. Shallow (e.g., Sossego), middle (e.g., Sequerinho) and deep (GT-34) alteration zones reflect the formation conditions of each occurrence.
4. Initial CO_2 -NaCl immiscible fluids suggest a dominant magmatic origin due to elevated P–T conditions, contradicting the evaporitic source previously considered. Late-stage alteration zone fluid provenance remains controversial and likely resulted from mixed sources.
5. The system displays evidence of continuous reworking as different alterations develop. Nickel is present in Pn during the main mineralization and replaced by Mill during late-stage K-Fe (Hem) alteration. Remobilization is also observed when K-Fe (Mt) alteration overlaps the main Ni mineralization and/or Ca alteration, respectively, forming Mag-Po-Cpy and/or Act. Changing the sulfide/amphibole phase also reflect different P-T conditions at which the alteration developed
6. Geochronological data obtained support a Neoproterozoic (2.724±4 Ga) mineralization event. The mineralization partially overlaps the bimodal Neoproterozoic magmatism (2.75–2.70 Ga) present at the Carajás domain supporting a magmatic-hydrothermal formation.

3.11 Acknowledgements

We are thankful for outstanding logistical support from VALE. We are also thankful for financial support from (CNPq) and from The Swedish Research Council. Further thanks are to S. B. Hühn (VALE) for showing distinct IOCG features at CMP.

3.12 Reference

- Araújo OJB, Maia RGN, Jorge-João XS, Costa JBS (1988) A megaestruturação da folha Serra dos Carajás. In: 7th Congresso Latino Americano de Geologia, Belém. (Proceedings).
- Araújo OJB, Maia RGN (1991) Serra dos Carajás, folha SB.22-ZA, Estado do Pará. Programa Levantamentos Geológicos Básicos do Brasil. Companhia de Pesquisa de Recursos Minerais
- Barton MD, Johnson DA (1996) Evaporitic source model for igneous-related Fe oxide-(REE-Cu-Au-U) mineralization. *Geology* 24:259–262
- Barton MD (2014) Iron oxide(-Cu-Au-REE-P-Ag-U-Co) systems. In: Holland H, Turekian K (eds) *Treatise on Geochemistry*, 2nd edn. pp 515–541.
- Corriveau L, Mumin AH, Setterfield T (2010) IOCG environments in Canada: Characteristics, geological vectors to ore and challenges. In: Porter TM (ed) *Hydrothermal iron oxide copper-gold & related deposits: A global perspective*. Adelaide, Australia, pp 311–344.
- Corriveau L, Montreuil JF, Potter EG (2016) Alteration facies linkages among iron oxide copper-gold, iron oxide apatite, and affiliated deposits in the Great Bear magmatic zone, Northwest Territories, Canada. *Econ Geol* 111:2045–2072.
- Costa UAP, Paula RR, Silva DPB, Barbosa JPO, Silva CMG, Tavares FM, Oliveira JKM, Justo AP (2016) Programa Geologia do Brasil – PGB. Mapa de integração Geológico geofísico da ARIM Carajás. Estado do Pará, Belém. CPRM, escala 1: 250000
- Craveiro GS, Villas RN, Silva ARC (2012) Depósito Cu-Au Visconde, Carajás (PA): geologia e alteração hidrotermal das rochas encaixantes. *Revista Brasileira de Geociências* 42:453-470
- Dall’Agnol R, Lafon JM, Macambira MJB (1994) Proterozoic anorogenic magmatism in the Central Amazonian Province, Amazonian Craton: geochronological, petrological and geochemical aspects. *Miner Petrol* 50:113-138.
- Dardenne MA, Ferreira Filho CF, Meirelles MR (1988) The role of shoshonitic and calc-alkaline suites in the tectonic evolution of the Carajás district, Brazil. *J S American Earth Sci* 1:363–372.
- Dardenne MA, Schobbenhaus CS (2001) *Metalogênese do Brasil*. Editora Universidade de Brasília/CNPq, Brasília.
- deMelo GHC, Moteiro LVS, Xavier RP, Moreto CPN, Santiago ESB, Dufrane SA, Aires B, Santos AFF (2017) Temporal evolution of the giant Salobo IOCG deposit, Carajás Province (Brazil): constraints from paragenesis of hydrothermal alteration and U-Pb geochronology. *Miner Deposita* 52:709-732.
- DOCEGEO (1988) Revisão litoestratigráfica da Província Mineral de Carajás - Litoestratigrafia e principais depósitos minerais. In: 35th Congresso Brasileiro de Geologia, Belém. (Proceedings).
- Domingos FHG (2009) The structural setting of the Canaã dos Carajás region and Sossego-Sequeirinho deposits, Carajás, Brazil. Dissertation, Durham University.
- Dreher AM (2004) O depósito primário de Cu–Au de Igarapé Bahia, Carajás: Rochas fragmentárias, fluidos mineralizantes e modelo metalogenético. Ph.D. thesis, Universidade Estadual de Campinas, 221p.
- Feio GRL, Dall’Agnol R, Dantas EL, Macambira MJB, Gomes ACB, Sardinha AS, Oliveira DC, Santos RD, Santos PA (2012) Geochemistry, geochronology, and origin of the Neoproterozoic Planalto Granite suite, Carajás, Amazonian craton: a-type or hydrated charnockitic granites? *Lithos* 151:57–73
- Feio GRL, Dall’Agnol R, Dantas EL, Macambira MJB, Santos JOS, Althoff FJ, Soares JEB (2013) Archean granitoid magmatism in the Canaã dos Carajás area: implications for crustal evolution of the Carajás province, Amazonian craton, Brazil. *Precambrian Res* 227:157–185
- Ferraz MM (2016) Caracterização e metalogênese do depósito de Ni do Jaguar, Província Mineral Carajás. Dissertation, Universidade de Brasília.
- Ferreira Filho CF, Caçado F, Correa C, Macambira EMB, Junqueira-Brod TC, Siepierski L (2007) Mineralizações estratiformes de PGE-Ni associadas a complexos acamadados em Carajás: os exemplos de Luanga e Serra da Onça. In: Rosa-Costa LT, Klein EL, Viglio EP (eds) *Contribuições à geologia da Amazônia*. SBG-Núcleo Norte, Belém, pp 1–14
- Frost CD, Frost BR (2008) On charnockites. *Gondwana Res* 13:30–44.
- Garcia VB, Della Giustina MES, Oliveira CG (2017) Orthopyroxene-bearing alteration at the roots of the Carajás IOCG mineral system, Brazil: an example from GT-34 prospect. In: 14th Biennial Meeting of the SGA, Québec. (Proceedings)

- Gibbs AK, Wirth KR, Hirata WK, Olszewski WJ Jr (1986) Age and composition of the grão Pará group volcanics, Serra dos Carajás. *Rev Bras Geocienc* 16:201–211
- Gomes CH, Lindenmayer ZG (2003) Anfibólitos cálcicos dos depósitos de Cu–Au de Gameleira, Salobo e Bahia, Província Mineral de Carajás, Pará: minerais metamórficos ou hidrotermais? In: Ronchi LH, Althoff FJ (Eds) *Caracterização e modelamento de depósitos minerais*. São Leopoldo, Rio Grande do Sul, pp 119–145.
- González-Álvarez I, Pirajno F, Kerrich R (2013) Hydrothermal nickel deposits: Secular variation and diversity. *Ore geol rev* 52:1–3
- Grainger CJ, Groves DI, Tallarico FHB, Fletcher IR (2008) Metallogensis of the Carajás mineral province, Southern Amazon craton, Brazil: Varying styles of Archean through Paleoproterozoic to Neoproterozoic base- and precious-metal mineralization. *Ore Geol Rev* 33:451–489.
- Groves DI, Bierlein FP, Meinert LD, Hitzman MW (2010) Iron oxide copper-gold (IOCG) deposits through earth history: Implications for origin, lithospheric setting, and distinction from other epigenetic iron oxide deposits. *Econ Geol* 105:641–654
- Harlov DE, Kerkhof AVD, Johansson L (2014) Localized, solid-state dehydration associated with the Varberg charnockite intrusion, SW Sweden. *Precambrian Res* 253:50–62
- Hirata WK, Rigon JC, Kadokaru K, Cordeiro AAC, Meireles EA (1982) *Geologia Regional da Província Mineral de Carajás*. In: 1st Simpósio de Geologia da Amazônia, Brazil. (Proceedings).
- Hitzman MW (2000) Iron oxide–Cu–Au deposits: What, where, when, and why. In: Porter TM (ed) *Hydrothermal iron oxide copper–gold and related deposits: A global perspective*. Austral Miner Fund, Adelaide, pp 9–25
- Hitzman MW, Oreskes N, Einaudi MT (1992) Geological characteristics and tectonic setting of Proterozoic iron oxide (Cu–U–Au–REE) deposits. *Precambrian Res* 58:241–287
- Holland T, Blundy J (1994) Non-ideal interactions in calcic amphiboles and their bearing on amphibole–plagioclase thermometry. *Contrib to Mineral Petrol* 116:443–447.
- Huhn SRB, Souza CIJ, Albuquerque MC, Leal E.D., Brustolin V (1999) Descoberta do depósito Cu(Au) Cristalino: Geologia e mineralização associada região da Serra do Rabo - Carajás – PA. In: 6th Simpósio de Geologia da Amazônia, Manaus. (Proceedings)
- Hunt J, Baker T, Thorkelson D (2005) Regional-scale Proterozoic IOCG mineralized breccia systems: examples from the Wernecke Mountains, Yukon, Canada. *Miner Deposita* 40:492–514
- Lafon JM, Macambira MJB, Pidgeon RT (2000) Zircon U–Pb SHRIMP dating of Neoproterozoic magmatism in the southwestern part of the Carajás Province (eastern Amazonian Craton, Brazil). In: 30th International Geological Congress, Beijing, China.
- Lancaster Oliveira J, Fanton J, Almeida AJ, Leveille RA, Vieira S (2000) Discovery and geology of the Sossego copper-gold deposit, Carajás District, Pará State, Brazil: In: 31st International Geology Congress, Rio de Janeiro. (Proceedings)
- Lindenmayer ZG (2003) Depósito de Cu–Au do Salobo, Serra dos Carajás: Uma revisão. In: Ronchi LH, Althoff FJ (eds) *Caracterização e modelamento de depósitos minerais*. Editora Unisinos, São Leopoldo, pp 69–98
- Liu W, Migdisov A, Williams-Jones A (2012) The stability of aqueous nickel (II) chloride complexes in hydrothermal solutions: Results of UV–Visible spectroscopic experiments. *Geochim Cosmochim Acta* 94:276–290
- Lopes AM, Moreto CPN, Xavier RP, Melo GHC (2017) Caracterização geológica e metalogenética do depósito IOCG Pantera, Domínio Rio Maria – Carajás. In: 15 Simpósio de Geologia da Amazônia, Belém. (Proceedings)
- Lowenstern JB (2001) Carbon dioxide in magmas and implications for hydrothermal systems. *Miner Deposita* 36:490–502.
- Ludwig KR (2012) User's manual for Isoplot 3.75: a geochronological toolkit for Microsoft Excel. Spec Pub Berkley Geochron Center (5 edn)
- Macambira BEM, Ferreira Filho CF (2002) Fracionamento magmático dos corpos máfico ultramáficos da Suíte Intrusiva Cateté – sudeste do Pará. In: Klein EL, Vasquez ML, Rosa-Costa LT (Eds) *Contribuições à geologia da Amazônia*. Belém, SBG-Núcleo Norte, pp 105–114
- Machado N, Lindenmayer ZG, Krogh TE (1991) U–Pb Geochronology of Archean magmatism and basement reactivation in the Carajás area, Amazon Shield, Brazil. *Precambrian Res* 49:329–354
- Manning CE, Aranovich LY (2014) Brines at High Pressure and Temperature: Thermodynamic, Petrologic and Geochemical Effects. *Precambrian Res* 253:6–16
- Monteiro LVS, Xavier RP, Hitzman MW, Juliani C, Souza Filho CR, Carvalho ER (2008a) Mineral chemistry of ore and hydrothermal alteration at the Sossego iron oxide-copper-gold deposit, Carajás mineral province, Brazil. *Ore Geol Rev* 34:317–336.

- Monteiro LVS, Xavier RP, Carvalho ER, Hitzman MW, Johnson CA, Souza Filho CR, Torresi I (2008b) Spatial and temporal zoning of hydrothermal alteration and mineralization in the Sossego iron oxide–copper–gold deposit, Carajás Mineral Province, Brazil: Paragenesis and stable isotope constraints. *Miner Deposita* 43:129–159
- Montreuil JF, Corriveau L, Potter EG, De Toni AF (2016) Tectonomagmatic evolution of the southern Great Bear magmatic zone (Northwest Territories, Canada): Implications for the genesis of iron oxide-alkali-altered hydrothermal systems. *Econ Geol* 111:2111–2138.
- Mora CI, Valley JW (1989) Halogen-rich scapolite and biotite: implications for metamorphic fluid-rock interactions. *Am Mineral* 74:721–737
- Moreto CPN, Monteiro LVS, Xavier RP, Amaral WS, Santos TJS, Juliani C, Souza Filho CR (2011) Mesoarchean (3.0 and 2.86 Ga) host rocks of the iron oxide-Cu-Au Bacaba deposit, Carajás Mineral province: U-Pb geochronology and metallogenetic implications: *Miner Deposita* 46:789–811.
- Moreto CPN (2013) U-Pb and Re-Os geochronology applied to the metallogenetic evolution of the Southern Copper Belt of the Carajás Province. Dissertation, University of Campinas
- Moreto CPN, Monteiro LVS, Xavier RP, Creaser RA, DuFrane A, Melo GHC, Silva MAD, Tassinari CCG, Sato K (2015a) Timing of multiple hydrothermal events in the iron oxide-copper-gold deposits of the southern copper belt, Carajás Province, Brazil. *Miner Deposita* 50:517–546
- Moreto CPN, Monteiro LVS, Xavier RP, Creaser RA, Dufrane SA, Tassinari CCG, Sato K, Kemp AIS, Amaral WS (2015b) Neoproterozoic Iron Oxide-Copper-Gold Events at the Sossego Deposit, Carajás Province, Brazil: Re-Os and U-Pb Geochronological Evidence. *Econ Geol* 110:809-835
- Naldrett AJ (2004) Magmatic sulfide deposits geology, geochemistry and exploration. pp. 727
- Newton RC, Aranovich LY, Hansen EC, Vandenheuvel BA (1998) Hypersaline fluids in Precambrian deep-crustal metamorphism. *Precambrian Res* 91:41-63.
- Newton RC, Tsunogae T (2014) Incipient charnockite: Characterization at the type localities. *Precambrian Res* 253:38–49
- Nogueira ACR, Truckenbrod W, Costa JBS, Pinheiro RVL (1994) Análise faciológica e estrutural da Formação Águas Claras, Pré-Cambriano da Serra dos Carajás. In: 4th Simpósio de Geologia da Amazônia, Brazil. (Proceedings)
- Perchuk LL, Gerya TV (1993) Fluid control of charnockitization. *Chem Geol* 108:175-186.
- Perchuk LL, Safonov OG, Gerya TV, Fu B, Harlov DE (2000) Mobility of components in metasomatic transformation and partial melting of gneisses; an example from Sri Lanka. *Contrib Miner Petrol* 140:212–232.
- Perring CS, Pollard PJ, Dong G, Nunn AJ, Blake KL (2000) The Lightning Creek sill complex, Cloncurry District, Northwest Queensland, a source of fluids for Fe oxide Cu–Au mineralization and sodic–calcic alteration. *Econ Geol* 95:1067–1089.
- Pestilho ALS (2011) Sistemática de isótopos estáveis aplicada à caracterização da evolução dos paleosistemas hidrotermais associados aos depósitos cupríferos Alvo Bacaba e Alvo Castanha, Província Mineral de Carajás, PA. PhD thesis, University of Campinas
- Pidgeon RT, Macambira MJB, Lafon JM (2000) Th–U–Pb isotopic systems and internal structures of complex zircons from the enderbite from the Pium Complex, Carajás Province, Brazil: evidence for the ages of granulite facies metamorphism and the protolith of the enderbite. *Chem Geol* 166:159–171
- Pimentel MM, Machado N (1994) Geocronologia U–Pb dos terrenos granito-greenstone de Rio Maria, Pará. In: 38th Congresso Brasileiro de Geologia, Camboriú. (Proceedings)
- Pinheiro RVL, Holdsworth RE (1997) Reactivation of Archaean strike-slip fault systems, Amazon region, Brazil. *J Geol Soc London* 154: 99–103
- Pinheiro RVL, Kadekaru K, Soares AV, Freitas C, Ferreira SN, Matos FMV (2013) Carajás, Brazil—a short tectonic review. In: 13th Simposio de geologia da Amazônia. Belém. (Proceedings)
- Pollard PJ (2001) Sodic–(calcic) alteration in Fe-oxide–Cu–Au districts: an origin via unmixing of magmatic H₂O–CO₂–NaCl+CaCl₂–KCl fluids. *Miner Deposita* 36:93–100.
- Porter TM (2010) Current understanding of iron oxide associated-alkali altered mineralised systems. Part 1. An overview. In: Porter TM (ed) *Hydrothermal iron oxide copper–gold and related deposits: A global perspective*. Austral Miner Fund, Adelaide, pp 5–32
- Prado EBG (2017) Petrografia, Calcografia e Microtectônica do Depósito Salobo, Província Mineral de Carajás, Sudeste do Pará, Brasil. Dissertation, Universidade Federal do Rio de Janeiro.
- Rajesh HM, Belyanin GA, Safonov, OG, Kovaleva EI, Golunova MA, Van Reenen DD (2013) Fluid-induced dehydration of the Paleoproterozoic Sand River Biotite-Hornblende Gneiss, Central Zone, Limpopo Complex, South Africa *J Petrol.* 54:3–40.
- Réquia K, Stein H, Fontboté L, Chiaradia M (2003) Re-Os and Pb-Pb geochronology of the Archean Salobo iron oxide copper–gold deposit, Carajás Mineral Province, north Brazil. *Miner Deposita* 38:727–738

- Ricci PSF, Carvalho MA (2006) Rocks of the Pium-Area, Carajás Block, Brazil – a deep seated high-T gabbroic pluton (charnockitoid-like) with xenoliths of enderbite gneisses dated at 3002 Ma — the basement problem revisited. In: 8th Simpósio de Geologia da Amazônia, Brazil.
- Rosa WD (2014) Complexos acamadados da Serra da Onça e Serra do Puma: Geologia e petrologia de duas intrusões Máfico-Ultramáficas com sequência de cristalização distinta na Província Arqueana de Carajás, Brasil. Dissertation, Universidade de Brasília.
- Santos JOS (2003) Geotectônica do Escudo das Guianas e Brasil-Central. In: Bizzi LA et al. (eds) Geologia, tectônica e recursos minerais do Brasil: texto, mapas e SIG. CPRM-Serviço Geológico do Brasil, Brasília, pp 169-226
- Santos RD, Oliveira DC (2010) Geologia, petrografia e caracterização geoquímica das rochas máficas do Complexo Pium — Província Mineral de Carajás. In: 45th Congresso Brasileiro de Geologia, Belém.
- Santosh M, Omori S (2008) CO₂ Flushing: A plate tectonic perspective. *Gondwana Res* 13:86-102.
- Sardinha AS, Barros CE De M, Krymsky M (2006) Geology, geochemistry and U–Pb geochronology of the Archean (2.74 Ga) Serra do Rabo granite stocks, Carajás Metallogenic Province, northern Brazil. *J S Am Earth Sci* 20:327–339
- Siepierski L (2016) Geologia, petrologia e potencial para mineralizações magmáticas dos corpos máfico-ultramáficos da região de Canaã dos Carajás, Província Mineral de Carajás, Brasil. PhD Thesis, Universidade de Brasília.
- Siepierski L (2008) Geologia e petrologia do prospecto GT-34: Evidência de metassomatismo de alta temperatura e baixa fO₂, Província Mineral Carajás, Brasil. Dissertation, University of Brasília.
- Sillitoe RH (2003) IOCG deposits: An Andean view. *Miner Deposita* 38:787–812.
- Stolper E, Fine G, Johnson T, Newman S (1987) Solubility of carbon dioxide in albitic melt. *American Mineral* 72:1071-1085
- Teixeira AS, Ferreira Filho CF, Giustina MESD, Araujo SM, Silva HHAB (2015) Geology, petrology and geochronology of the Lago Grande layered complex: Evidence for a PGE-mineralized magmatic suite in the Carajás Mineral Province, Brazil. *J S American Earth Sci* 64:116-138.
- Tian Y, Etschmann B, Liu W, Borg S, Mei Y, Testemale D, O'Neill B, Rae N, Sherma DM, Ngothai Y, Johannessen B, Glover C, Brugger J (2012) Speciation of nickel (II) chloride complexes in hydrothermal fluids: in situ XAS study. *Chem Geol* 334:345-363
- Tornos F, Velasco F, Hanchar JM (2016) Iron-rich melts, magmatic magnetite, and superheated hydrothermal systems: The El Laco deposit, Chile. *Geology* 44:427-430.
- Torresi I, Bortholoto DFA, Xavier RP, Monteiro LVS (2012) Hydrothermal alteration, fluid inclusions and stable isotope systematics of the Alvo 118 iron oxide–copper–gold deposit, Carajás Mineral Province (Brazil): implications for ore genesis. *Miner Deposita* 47:299–323
- Touret JLR, Huizenga JM (1999) Precambrian intraplate magmatism: high temperature, low pressure crustal granulites. *J African Earth Sci* 28:367-382
- VALE (2016) Form 20-F Annual Report Pursuant to section 13 or 15(d) of the securities exchange act of 1934. For the fiscal year ended: December 31, 2015. Commission File number: 001-15030. pp 174
- Vanko DA, Bishop FC (1982) Occurrence and origin of marialitic scapolite in the Humboldt Lopolith, N.W. Nevada. *Contrib Mineral Petrol* 81:277–289
- Vasquez LV, Rosa-Costa LR, Silva CG, Ricci PF, Barbosa JO, Klein EL, Lopes ES, Macambira EB, Chaves CL, Carvalho JM, Oliveira JG, Anjos GC, Silva HR (2008) Geologia e Recursos Minerais do Estado do Pará: Sistema de Informações Geográficas—SIG: Texto Explicativo dos Mapas Geológico e Tectônico e de Recursos Minerais do Estado do Pará. Organizers: M.L Vasquez, L.T. Rosa- Costa. Escala 1:1.000.000. Belém: CPRM.
- Veloso ASR, Moteiro LVS, Juliani C (2016) Depósito de cobre-(Níquel) Jatobá, Província Carajás (PA): Evolução paragenética e fontes de enxofre. In: 48th Congresso Brasileiro de Geologia, Porto Alegre.
- Webster JD, Holloway JR (1988) Experimental constraints on the partitioning of Cl between topaz rhyolite melt and H₂O and H₂O + CO₂ fluids: New implications for granitic differentiation and ore deposition. *Geol Soc America B* 52:2091-2105.
- Webster JD, Kinzler RJ, Mathez EA (2002) Chloride and water solubility in basalt and andesite liquids and implications for magmatic degassing. *Geochim Cosmochim Acta* 63:729- 738.
- Webster JD (2004) The exsolution of magmatic hydrosaline chloride liquids. *Chem Geol* 210:33–48.
- Whitehouse MJ, Kamber BS (2005) Assigning dates to thin gneissic veins in high- grade metamorphic terranes - a cautionary tale from Akilia, southwest Greenland. *J Petrol* 46:291-318.
- Whitehouse MJ, Kamber BS, Moorbath S (1999) Age significance of U-Th-Pb zircon data from early Archean rocks of west Greenland – a reassessment based on combined ion-microprobe and imaging studies. *Chem Geol* 160:201-224.

- Williams PJ, Guoyi D, Ryan CG, Pollard PJ, Rotherham JF, Mernagh TP, Chapman LH (2001) Geochemistry of high-salinity fluid inclusions from the Starra (Fe)-Cu-Au deposit, Cloncurry district, Queensland. *Econ Geol* 96:875–883.
- Williams PJ, Pollard PJ (2003) Australian Proterozoic iron oxide–Cu–Au deposits: An overview with new metallogenic and exploration data from the Cloncurry district, northwest Queensland. *Explor Min Geol* 10:191–213
- Williams PJ, Barton MD, Johnson DA, Fontboté L, de Haller A, Mark G, Oliver NHS, Marschik R (2005) Iron oxide-copper-gold deposits: Geology, space-time distribution, and possible modes of origin. *Econ Geol* 100th anniversary volume: 371–405.
- Wirth KR, Gibbs AK, Olszewski WJ (1986) U-Pb ages of zircons from the Grão Pará group and Serra dos Carajás granite, Pará, Brazil. *Revista Brasileira de Geociências* 16:195–200
- Xavier RP, Wiedenbeck M, Trumbull RB, Dreher AM, Monteiro LVS, Rhede D, Araújo CEG, Torresi I (2008) Tourmaline B-isotopes fingerprint marine evaporites as the source of high-salinity ore fluids in iron oxide-copper-gold deposits, Carajás mineral province (Brazil). *Geol* 36:743–746.
- Xavier RP, Monteiro LVS, Souza Filho CR, Torresi I, Carvalho ER, Dreher AM, Wiedenbeck M, Trumbull RB, Pestilho ALS, Moreto CPN (2010) The iron oxide copper–gold deposits of the Carajás Mineral Province, Brazil: An updated and critical review. In: Porter TM (ed) *Hydrothermal iron oxide copper-gold & related deposits: A global perspective*, volume 3. PGC Publishing, Adelaide, pp 285–306
- Xavier RP, Monteiro LVS, Moreto CPN, Pestilho ALS, Melo GHC, Silva MAD, Aires B, Ribeiro C, Silva FHF (2012) The iron oxide copper-gold systems of the Carajás mineral province, Brazil. *SEG* 16:433–454.
- Xavier RP, Moreto C, de Melo GHC, Toledo P, Hunger R, Delinardo M, Faustioni J, Lopes A (2017) Geology and metallogeny of Neoproterozoic and Paleoproterozoic copper systems of the Carajás Domain, Amazonian Craton, Brazil. In: 14th SGA Biennial Meeting, Québec. (Proceedings)
- Yang XQ, Li ZL, Yu SQ (2016) Phase equilibrium modeling, fluid inclusions and origin of charnockites in the Datian region of the northeastern Cathaysia Block, South China. *J Asian Earth Sci* 126:14–28

Capítulo 4: *Conclusão*

1. Processos similares aos descritos para o Sistema IOCG clássico também foram observados no depósito GT-34 (e.g. Alteração álcali-Fe, controle estrutural, óxido de Fe). Mesmo com Cu e Au presentes em níveis subeconômicos, o depósito GT-34 apresenta as demais características similares a depósitos do sistema IOCG.
2. Condições de pressão e temperatura definidas para alteração Na-Mg inicial (Opx-Scp) sugerem temperaturas $> 700^{\circ}\text{C}$ e pressões entre 5-7 kbar. Essas condições elevam em pelo menos 200°C a temperatura inicial e a pressão em até 2 kbar. Tais parâmetros tornam o depósito GT-34 a porção mais profunda até então conhecida para o Sistema IOCG de Carajás.
3. O Sistema IOCG de Carajás revela um contínuo em diferentes níveis crustais. Níveis rasos (Sossego), médios (Sequerinho) e profundos (GT-34) são inferidos a partir da associação mineral das alterações hidrotermais.
4. Fluidos iniciais imiscíveis $\text{CO}_2\text{-NaCl}$ sugerem uma fonte predominantemente magmática devido às elevadas condições de P-T. Tais condições contrapõem as sugestões iniciais que fluidos originários a partir de evaporitos seriam associados a elevada salinidade do sistema. Contudo, alterações tardias são controversas e podem ser resultado de uma mistura de fluidos.
5. O sistema apresenta evidências para um retrabalhamento contínuo conforme as diferentes alterações se desenvolvem. Niquel, presente inicialmente como pentlandita, é retrabalhado reprecipitado como millerita durante a alteração K-Fe (Hem). Evidência para remobilização também é observada quando a alteração K-Fe (Mt) corta a mineralização de Ni e/ou alteração Ca, formando-se, respectivamente, Mag-Po-Cpy e/ou Act. Tais mudanças refletem diferentes condições de P-T em que as alterações se desenvolveram.
6. Dados de geocronologia U-Pb (2.724 ± 4) suportam um evento mineralizante Neoarqueano. As idades obtidas sobrepõem-se ao magmatismo bimodal Neoarqueano (2.75–2.70 Ga) do domínio Carajás corroborando uma origem magmático-hidrotermal.

Referências

- Alvarenga C J S, Moura CAV, Gorayeb PSS, Abreu FAM (2000) Paraguai and Araguaia belts. In: Cordani UG, Milani EJ, Thomaz Filho A, Campos DA (Eds.), *Tectonic Evolution of South America*, pp 183-193.
- Augusto RA, Monteiro LVS, Xavier R, Souza Filho CR (2008) Zonas de alteração hidrotermal e paragênese do minério de cobre do Alvo Bacaba, Província Mineral de Carajás (PA). *Rev Bras Geocienc* 38(2):263–277.
- Araújo OJB, Maia RGN, Jorge-João XS, Costa JBS (1988) A megaestruturação da folha Serra dos Carajás. In: 7th Congresso Latino Americano de Geologia, Belém. (Proceedings).
- Araújo OJB, Maia RGN (1991) Serra dos Carajás, folha SB.22-ZA, Estado do Pará. Programa Levantamentos Geológicos Básicos do Brasil. Companhia de Pesquisa de Recursos Minerais.
- Barbosa JPO (2004) Geologia Estrutural, Geoquímica, Petrografia e Geocronologia de granitóides da região do Igarapé Gelado, norte da Província Mineral de Carajás. Dissertação, Universidade Federal do Pará.
- Barros CDM, Barbey P, Boullier AM (2001) Role of magma pressure, tectonic stress and crystallization progress in the emplacement of syntectonic granites. The A-type Estrela Granite Complex (Carajás Mineral Province, Brazil). *Tectonophysics*, 343(1): 93-109
- Barton MD, Johnson DA (1996) Evaporitic source model for igneous related Fe oxide–(REE–Cu–Au–U) mineralization. *Geology* 24:259–262
- Barton MD (2014) Iron oxide(-Cu-Au-REE-P-Ag-U-Co) systems. In: Holland H, Turekian K (eds) *Treatise on Geochemistry*, 2nd edn. pp 515–541.
- Botelho NF, Moura MA, Teixeira LM, Olivo GR, Cunha LM, Santana UM (2005) Caracterização geológica e metalogenética do depósito de Cu ± (Au, W, Mo, Sn) Breves, Carajás. In: Marini OJ, Queiroz ET, Ramos BW (eds) *Caracterização de depósitos minerais em Distritos Mineiros da Amazônia*, 2nd edn, Brasília, ADIMB, pp 335-389.
- Corriveau L, Montreuil JF, Potter EG (2016) Alteration facies linkages among iron oxide copper-gold, iron oxide apatite, and affiliated deposits in the Great Bear Magmatic Zone, Northwest Territories, Canada. *Econ Geol* 111:2045-2072
- Corriveau L, Blein O, Gervais F, Trapy PH, De Souza S (2017) Iron Oxide and Alkali-calcic alteration, Skarn and Epithermal Mineralizing systems of the Grenville Province, Canada: The Bondy Gneiss Complex in the central metasedimentary belt as a case example: a field trip to the 14th biennial SGA meeting; Geological Survey of Canada, Open File, pp 110
- Costa UAP, Paula RR, Silva DPB, Barbosa JPO, Silva CMG, Tavares FM, Oliveira JKM, Justo AP (2016) Programa Geologia do Brasil – PGB. Mapa de integração Geológico geofísico da ARIM Carajás. Estado do Pará, Belém. CPRM, escala 1: 250000
- Craveiro GS (2011) Geologia, fluidos hidrotermais e origem do depósito cupro-aurífero Visconde, Província Mineral de Carajás. Dissertation, University Federal of Pará
- Dall’Agnol R, Lafon JM, Macambira MJB (1994) Proterozoic anorogenic magmatism in the Central Amazonian Province, Amazonian Craton: geochronological, petrological and geochemical aspects. *Miner Petrol* 50:113-138.
- Dall’Agnol R, Teixeira NP, Rämö OT, Moura CAV, Macambira MJB, Oliveira DC (2005) Petrogenesis of the Paleoproterozoic, rapakivi, A-type granites of the Archean Carajás Metallogenic Province, Brazil. *Lithos* 80:01–129.
- Dardenne MA, Ferreira Filho CF, Meirelles MR (1988) The role of shoshonitic and calc-alkaline suites in the tectonic evolution of the Carajás district, Brazil. *J S American Earth Sci* 1:363–372.

- DOCEGEO (1988) Revisão litoestratigráfica da Província Mineral de Carajás - Litoestratigrafia e principais depósitos minerais. In: 35th Congresso Brasileiro de Geologia, Belém. (Proceedings).
- Domingos FHG (2009) The structural setting of the Canaã dos Carajás region and Sossego-Sequeirinho deposits, Carajás, Brazil. Dissertation, Durham University.
- Feio GRL, Dall'Agnol R, Dantas EL, Macambira MJB, Gomes ACB, Sardinha AS, Oliveira DC, Santos RD, Santos PA (2012) Geochemistry, geochronology, and origin of the Neoproterozoic Planalto Granite suite, Carajás, Amazonian craton: a-type or hydrated charnockitic granites? *Lithos* 151:57–73
- Feio GRL, Dall'Agnol R, Dantas EL, Macambira MJB, Santos JOS, Althoff FJ, Soares JEB (2013) Archean granitoid magmatism in the Canaã dos Carajás area: implications for crustal evolution of the Carajás province, Amazonian craton, Brazil. *Precambrian Res* 227:157–185
- Ferraz MM (2016) Caracterização e metalogênese do depósito de Ni do Jaguar, Província Mineral Carajás. Dissertation, Universidade de Brasília.
- Frutos J, Oyarzun J (1975) Tectonic and geochemical evidence concerning the genesis of El Laco magnetite lava flow deposits, Chile. *Econ Geol Bulletin Soc Econ Geol*, 70:988–990
- Garcia VB, Della Giustina MES, Oliveira CG (2017) Orthopyroxene-bearing alteration at the roots of the Carajás IOCG mineral system, Brazil: an example from GT-34 prospect. In: 14th Biennial Meeting of the SGA, Québec. (Proceedings)
- Galarza MA, Macambira MJB (2002) Geocronologia e evolução crustal da área do depósito de Cu-Au Gameleira, Província Mineral de Carajás (Pará), Brasil. *Geol USP*, 2:143-159
- Galarza MA, Macambira MJB, Moura CAV (2003) Geocronologia Pb-Pb e Sm-Nd das rochas máficas do depósito Igarapé Bahia, Província Mineral de Carajás (PA). In: 7th Simpósio de Geologia da Amazônia, Belém (Proceedings)
- Gibbs AK, Wirth KR, Hirata WK, Olszewski WJ Jr (1986) Age and composition of the grão pará group volcanics, Serra dos Carajás. *Rev Bras Geocienc* 16:201–211
- Grainger CJ, Groves DI, Tallarico FHB, Fletcher IR (2008) Metallogenesis of the Carajás mineral province, Southern Amazon craton, Brazil: Varying styles of Archean through Paleoproterozoic to Neoproterozoic base- and precious-metal mineralization. *Ore Geol Rev*, 33:451–489
- Groves DIP, Bierlein FP, Meinert LD, and Hitzman MW (2010) Iron oxide copper–gold (IOCG) deposits through Earth history; implications for origin, lithospheric setting, and distinction from other epigenetic iron oxide deposits. *Economic Geology* 105: 641–654.
- Hauck SA (1990) Petrogenesis and tectonic setting of middle Proterozoic iron oxide-rich ore deposits – An ore deposit model for Olympic Dam-type mineralization. *USGS Bulletin* 1932:4–39.
- Hirata WK, Rigon JC, Kadkaru K, Cordeiro AAC, Meireles EA (1982) Geologia Regional da Província Mineral de Carajás. In: 1st Simpósio de Geologia da Amazônia, Belém. (Proceedings)
- Hitzman MW (2000) Iron oxide–Cu–Au deposits: What, where, when, and why. In: Porter TM (ed) *Hydrothermal iron oxide copper–gold and related deposits: A global perspective*. Austral Miner Fund, Adelaide, pp 9–25
- Hitzman MW, Oreskes N, Einaudi MT (1992) Geological characteristics and tectonic setting of Proterozoic iron oxide (Cu-U-Au-REE) deposits. *Precambrian Res* 58:241–287
- Huhn SB, Macambira MJB, Dall'Agnol R (1999a) Geologia e geocronologia Pb/Pb do granito alcalino arqueano Planalto, região da Serra do Rabo, Carajás-PA. In: 7th Simpósio de Geologia da Amazônia, Manaus. (Proceedings)
- Huhn SRB, Souza CIJ, Albuquerque MC, Leal E.D., Brustolin V (1999b) Descoberta do depósito Cu(Au) Cristalino: Geologia e mineralização associada região da Serra do Rabo - Carajás – PA. In: 6th Simpósio de Geologia da Amazônia, Manaus. (Proceedings)

- Hunger RB (2015) O Depósito de Cu-Au Santa Lúcia, Província Carajás (PA): Caracterização geológica e evolução do sistema hidrotermal. Dissertation, Universidade estadual de Campinas.
- Hunger RB, Xavier RP, Moreto CPN, Toledo PIF, Su ZK, Zhao XF (2017) Fluid evolution in the Grota Funda Iron Oxide Copper-Gold (IOCG) deposit, Carajás Domain, Brazil: Evidence from fluid inclusions and Boron Isotope Analyses. In: 15th Simpósio de Geologia da Amazônia, Belém (Proceedings)
- Hunt JA, Baker T, Thorkelson DJ (2007) A review of iron oxide copper–gold deposits, with focus on the Wernecke Breccias, Yukon, Canada, as an example of a non-magmatic end member and implications for IOCG genesis and classification. *Explo Mining Geol* 16:209–232.
- Jesus SSGP, Monteiro LVS, Iguma B, Melo GHC, Rosendo OSC, Silva AJC (2016) O Depósito de óxido de Ferro-Cobre e Ouro de Furnas, Província Mineral Carajás: Zonas de alteração hidrotermal e Paragênese do Minério. In: 48 Congresso Brasileiro de Geologia, Porto Alegre, RS. (Proceedings)
- Lancaster Oliveira J, Fanton J, Almeida AJ, Leveille RA, Vieira S (2000) Discovery and geology of the Sossego copper-gold deposit, Carajás District, Pará State, Brazil: In: 31st International Geology Congress, Rio de Janeiro. (Proceedings)
- Lopes AM, Moreto CPN, Xavier RP, Melo GHC (2017) Caracterização geológica e metalogenética do depósito IOCG Pantera, Domínio Rio Maria – Carajás. In: 15 Simpósio de Geologia da Amazônia, Belém. (Proceedings)
- Macambira BEM, Ferreira Filho CF (2002) Fracionamento magmático dos corpos máfico ultramáficos da Suíte Intrusiva Cateté – sudeste do Pará. In: Klein EL, Vasquez ML, Rosa-Costa LT (Eds) Contribuições à geologia da Amazônia. Belém, SBG-Núcleo Norte, pp 105-114.
- Macambira EMB, Ferreira Filho CF (2005) Exploration and origin of stratiform PGE mineralization in the Serra da Onça layered complex, Carajás Mineral Province, Brazil. In: 10th International Platinum Symposium Extended Abstract, Oulu. (Proceedings)
- Machado N, Lindenmayer ZG, Krogh TE (1991) U-Pb Geochronology of Archean magmatism and basement reactivation in the Carajás area, Amazon Shield, Brazil. *Precambrian Res* 49(3-4):329-354
- Mansur ET, Ferreira Filho CF (2016) Magmatic structure and geochemistry of the Luanga Mafic-Ultramafic Complex: Further constraints for the PGE-mineralized magmatism in Carajás, Brazil. *Lithos* doi:10.1016/j.lithos.2016.09.036
- Melo GHC, Monteiro LVS, Moreto CPN, Xavier RP, Silva MAD (2014) Bacuri copper deposit: host rocks, hydrothermal alteration and characterization of the copper ore, Carajás Province (PA). *Braz J Geol* 44:73–90
- Melo GHC, Monteiro LVS, Xavier RP, Moreto CPN, Santiago ESB, Dufrane A, Aires B, Santos AFF (2016) Temporal evolution of the giant Salobo IOCG deposit, Carajás Province (Brazil): constraints from paragenesis of hydrothermal alteration and U-Pb geochronology. *Miner Deposita* 52:709-732.
- Meyer C (1988) Ore deposits as guides to geologic history of the Earth. *Annual Rev Earth Plan Sci* 16:147–171.
- Monteiro LVS, Xavier RP, Carvalho ER, Hitzman MW, Johnson CA, Souza Filho CR, Torresi I (2008a) Spatial and temporal zoning of hydrothermal alteration and mineralization in the Sossego iron oxide–copper–gold deposit, Carajás Mineral Province, Brazil: Paragenesis and stable isotope constraints. *Miner Deposita* 43:129–159.
- Monteiro LVS, Xavier RP, Hitzman MW, Juliani C, Souza Filho CR, Carvalho ER (2008b) Mineral chemistry of ore and hydrothermal alteration at the Sossego iron oxide-copper-gold deposit, Carajás mineral province, Brazil. *Ore Geol Rev* 34:317–336
- Moreto CPN, Monteiro LVS, Xavier RP, Amaral WS, Santos TJS, Juliani C, Souza Filho CR (2011) Mesoarchean (3.0 and 2.86 Ga) host rocks of the iron oxide-Cu-Au Bacaba deposit, Carajás Mineral province: U-Pb geochronology and metallogenetic implications: *Miner Deposita* 46:789–811.

- Moreto CPN, Monteiro LVS, Xavier RP, Creaser RA, DuFrane A, Melo GHC, Silva MAD, Tassinari CCG, Sato K (2015a) Timing of multiple hydrothermal events in the iron oxide-copper-gold deposits of the southern copper belt, Carajás Province, Brazil. *Miner Deposita* 50:517–546
- Moreto CPN, Monteiro LVS, Xavier RP, Creaser RA, Dufrane SA, Tassinari CCG, Sato K, Kemp AIS, Amaral WS (2015b) Neoproterozoic and Paleoproterozoic Iron Oxide-Copper-Gold Events at the Sossego Deposit, Carajás Province, Brazil: Re-Os and U-Pb Geochronological Evidence. *Econ Geol* 110:809-835
- Nogueira ACR, Truckenbrodt W, Pinheiro RVL (1995) Formação águas claras, Pré-cambriano da serra dos carajás: redescoberta e redefinição litoestratigráfica. In: Goeldi E (ed) *Bol Mus Paraense, Ciências da Terra* 7:177–277
- Panno SV, Hood WC (1983) Volcanic stratigraphy of the Pilot Knob iron deposits, Iron County, Missouri. *Econ Geol* 78:972-982.
- Park CR (1961) A magnetite “flow” in northern Chile: *Econ Geol Bulletin Soc Econ Geol*, 56: 431– 436.
- Parak T (1985) Phosphorus in different types of ore, sulfide in the iron deposit and the type and origin of ores at Kiruna. *Econ Geol* 80:646-665
- Perring CS, Pollard PJ, Dong G, Nunn AJ, Blake KL (2000) The Lightning Creek sill complex, Cloncurry District, Northwest Queensland, a source of fluids for Fe oxide Cu–Au mineralization and sodic–calcic alteration. *Econ Geol* 95:1067–1089.
- Pestilho ALS (2011) Sistemática de isótopos estáveis aplicada à caracterização da evolução dos paleo-sistemas hidrotermais associados aos depósitos cupríferos Alvo Bacaba e Alvo Castanha, Província Mineral de Carajás, PA. PhD thesis, University of Campinas
- Pidgeon RT, Macambira MJB, Lafon JM (2000) Th–U–Pb isotopic systems and internal structures of complex zircons from an enderbite from the Pium Complex, Carajás Province, Brazil: evidence for the ages of granulite facies metamorphism and the protolith of the enderbite. *Chem Geol* 166:159–171
- Pinheiro RVL, Holdsworth RE (1997) Reactivation of Archaean strikeslip fault systems, Amazon region, Brazil. *J Geol Soc London* 154: 99–103
- Pollard PJ (2001) Sodic–(calcic) alteration in Fe-oxide–Cu–Au districts: an origin via unmixing of magmatic H₂O–CO₂–NaCl+CaCl₂–KCl fluids. *Miner Deposita* 36:93–100.
- Porter TM (2010) Current understanding of iron oxide associated-alkali altered mineralised systems. Part 1. An overview. In: Porter TM (ed) *Hydrothermal iron oxide copper–gold and related deposits: A global perspective*. Austral Miner Fund, Adelaide, pp 5–32
- Previato M (2016) Evolução Paragenética e regime de fluidos hidrotermais no sistema mineral Borrachudo: implicações para metalogênese de cobre na província Carajás. Dissertation, Universidade de São Paulo
- Rigon JC, Munaro P, Santos LA, Nascimento JAS, Barreira CF (2000) Alvo 118 copper-gold deposit: Geology and mineralization, Serra dos Carajás, Pará, Brazil. In: 31st International Geological Congress, Rio de Janeiro. (Proceedings).
- Roberts DE, Hudson GRT (1983) The Olympic Dam copper-uranium-gold deposit, Roxby Downs, South Australia. *Econ Geol* 78:799-822
- Sardinha AS, Barros CEM, Krymsky RS, Macambira MJB (2001) Petrografia e geocronologia U-Pb em zircão do Granito Serra do Rabo, Província Mineral de Carajás, Pará. In: 7th Simpósio de Geologia da Amazônia, Belém. (Proceedings)
- Santiago ESB (2016) Elementos traço (in situ LA-ICP-MS) e isótopos estáveis ($\delta^{33}\text{S}$, $\delta^{34}\text{S}$, $\delta^{56}\text{Fe}$ e $\delta^{18}\text{O}$) em magnetita e sulfetos: origem e evolução de sistemas de Cu-Au Neoproterozoicos e Paleoproterozoicos da Província Mineral de Carajás, Brasil. PhD thesis, University of Campinas.

- Siepierski L (2016) Geologia, petrologia e potencial para mineralizações magmáticas dos corpos máfico-ultramáficos da região de Canaã dos Carajás, Província Mineral de Carajás, Brasil. PhD Thesis, Universidade de Brasília.
- Silva MG, Teixeira JBG, Pimentel MM, Vasconcelos PM, Arielo A, Rocha WJSF (2005) Geologia e mineralizações de Fe-Cu-Au do Alvo GT46 (Igarapé Cinzento), Carajás. In Marini OJ, Queiroz ET, Ramos BW (eds) Caracterização de Depósitos Mineraiis em Distritos Mineiros da Amazônia: DNPM, CT-Mineral/FINEP, ADIMB, pp 94–151.
- Tallarico FHB, Figueiredo BR, Groves DI, Kositcin N, McNaughton NJ, Fletcher IR, Rego JL (2005) Geology and SHRIMP U-Pb geochronology of the Igarapé Bahia deposit, Carajás copper-gold belt, Brazil: An Archean (2.57 Ga) example of iron-oxide Cu-Au-(U-REE) mineralization. In: *Econ Geol*, 100:7–28
- Tazava E, Oliveira CG (2000) The Igarapé Bahia Au-Cu-(REE-U) deposit, Carajás mineral province, northern Brazil. In: Porter TM (ed) *Hydrothermal iron oxide copper-gold and related deposits: A global perspective*. Austral Miner Fund, Adelaide, pp 203–212
- Teixeira AS, Ferreira Filho CF, Giustina MESD, Araujo SM, Silva HHAB (2015) Geology, petrology and geochronology of the Lago Grande layered complex: Evidence for a PGE-mineralized magmatic suite in the Carajás Mineral Province, Brazil. *J S American Earth Sci* 64:116-138.
- Tornos F, Velasco F, Hanchar JM (2016) Iron-rich melts, magmatic magnetite, and superheated hydrothermal systems: The El Laco deposit, Chile. *Geoly* 44:427-430.
- Torresi I, Bortholoto DFA, Xavier RP, Monteiro LVS (2012) Hydrothermal alteration, fluid inclusions and stable isotope systematics of the Alvo 118 iron oxide-copper-gold deposit, Carajás Mineral Province (Brazil): implications for ore genesis. *Miner Deposita* 47:299–323
- VALE (2016) Form 20-F Annual Report Pursuant to section 13 or 15(d) of the securities exchange act of 1934. For the fiscal year ended: December 31, 2015. Comission File number: 001-15030. pp 174
- Vasquez LV, Rosa-Costa LR, Silva CG, Ricci PF, Barbosa JO, Klein EL, Lopes ES, Macambira EB, Chaves CL, Carvalho JM, Oliveira JG, Anjos GC, Silva HR (2008) Geologia e Recursos Mineraiis do Estado do Pará: Sistema de Informações Geográficas—SIG: Texto Explicativo dos Mapas Geológico e Tectônico e de Recursos Mineraiis do Estado do Pará. Organizers: M.L Vasquez, L.T. Rosa- Costa. Escala 1:1.000.000. Belém: CPRM.
- Veloso ASR, Moteiro LVS, Juliani C (2016) Depósito de cobre- (Níquel) Jatobá, Província Carajás (PA): Evolução paragenética e fontes de enxofre. In: 48th Congresso Brasileiro de Geologia, Porto Alegre.
- Vieira EAP, Saueressig R, Siqueira JB, Silva ERP, Rego JL, Castro FDC (1988) Caracterização geológica da jazida polimetálica do Salobo 3a, reavaliação. In: 35th Congresso Brasileiro de Geologia, Belém. (Proceedings)
- Williams PJ, Barton MD, Johnson DA, Fontboté L, de Haller A, Mark G, Oliver NHS, Marschik R (2005) Iron oxide-copper-gold deposits: Geology, space-time distribution, and possible modes of origin. *Econ Geol* 100th anniversary volume:371–405.
- Wirth KR, Gibbs AK, Olszewski WJ (1986) U-Pb ages of zircons from the Grão Pará group and Serra dos Carajás granite, Pará, Brazil. *Revista Brasileira de Geociências* 16:195–200
- Xavier RP, Monteiro LVS, Moreto CPN, Pestilho ALS, Melo GHC, Silva MAD, Aires B, Ribeiro C, Silva FHF (2012) The iron oxide copper-gold systems of the Carajás mineral province, Brazil. *SEG* 16:433–454.
- Xavier RP, Moreto C, de Melo GHC, Toledo P, Hunger R, Delinardo M, Faustioni J, Lopes A (2017) Geology and metallogeny of Neoproterozoic and Paleoproterozoic copper systems of the Carajás Domain, Amazonian Craton, Brazil. In: 14th SGA Biennial Meeting, Québec. (Proceedings)

ANEXO I – supplementary EPMA analyses.

wt%	OPX1	OPX2	OPX3	OPX4	OPX5	OPX6	OPX7	OPX9	OPX8
SiO2	53.90	53.91	54.51	54.89	54.64	54.55	54.48	53.90	54.39
Al2O3	0.57	0.52	0.45	0.58	0.98	0.45	0.52	0.72	0.49
FeO	18.15	18.27	17.47	18.29	15.66	18.87	17.69	19.71	18.62
Cr2O3	0.00	0.04	0.00	0.00	0.04	0.08	0.01	0.00	0.02
TiO2	0.00	0.07	0.11	0.00	0.00	0.06	0.00	0.00	0.00
NiO	0.12	0.11	0.09	0.00	0.00	0.05	0.11	0.09	0.11
MnO	0.26	0.06	0.24	0.36	0.09	0.27	0.24	0.26	0.10
MgO	24.85	25.12	25.33	24.35	27.11	24.27	25.51	23.98	24.94
CaO	0.24	0.25	0.16	0.26	0.23	0.19	0.16	0.27	0.20
Na2O	0.00	0.02	0.03	0.01	0.03	0.00	0.05	0.00	0.00
K2O	0.00	0.02	0.04	0.02	0.01	0.03	0.02	0.00	0.03
V2O3	0.06	0.02	0.03	0.00	0.04	0.01	0.04	0.00	0.06
Total	98.17	98.41	98.44	98.75	98.80	98.82	98.82	98.94	98.95
Number of cations per 6 oxygens									
Si	2.00	2.00	2.01	2.02	1.99	2.01	2.00	2.00	2.00
Al iv	0.00	0.00	-0.01	-0.02	0.01	-0.01	0.00	0.00	0.00
Al vi	0.03	0.02	0.03	0.05	0.03	0.03	0.02	0.03	0.03
Fe iii	0.00	0.00	0.00	0.00	0.00	0.00	0.00	0.00	0.00
Cr	0.00	0.00	0.00	0.00	0.00	0.00	0.00	0.00	0.00
Ti	0.00	0.00	0.00	0.00	0.00	0.00	0.00	0.00	0.00
Fe ii	0.57	0.57	0.54	0.57	0.48	0.59	0.55	0.61	0.58
Mn	0.01	0.00	0.01	0.01	0.00	0.01	0.01	0.01	0.00
Mg	1.38	1.39	1.39	1.34	1.47	1.34	1.40	1.32	1.37
Ca	0.01	0.01	0.01	0.01	0.01	0.01	0.01	0.01	0.01
Na	0.00	0.00	0.00	0.00	0.00	0.00	0.00	0.00	0.00
K	0.00	0.00	0.00	0.00	0.00	0.00	0.00	0.00	0.00
total	3.98	3.99	3.98	3.97	3.99	3.98	3.99	3.99	3.98
Wo	0.49	0.51	0.33	0.54	0.45	0.39	0.33	0.55	0.40
En	70.22	70.55	71.49	69.40	75.04	68.92	71.43	67.71	70.02
Fs	29.29	28.93	28.18	30.06	24.51	30.68	28.24	31.74	29.58

wt%	OPX10	OPX11	OPX12	OPX13	OPX14	OPX15	OPX17	OPX16	OPX18
SiO2	54.28	53.88	54.37	53.66	54.56	54.30	54.42	54.81	54.89
Al2O3	0.19	0.50	0.60	0.51	0.65	0.54	0.62	0.93	1.08
FeO	19.52	19.71	19.09	19.03	18.44	18.66	18.66	16.75	16.32
Cr2O3	0.06	0.06	0.10	0.00	0.00	0.00	0.01	0.00	0.00
TiO2	0.00	0.18	0.00	0.25	0.02	0.07	0.00	0.04	0.15
NiO	0.14	0.02	0.16	0.10	0.05	0.16	0.06	0.14	0.08
MnO	0.15	0.28	0.23	0.29	0.32	0.25	0.18	0.17	0.18
MgO	24.21	23.92	24.21	25.05	24.95	25.09	25.15	26.40	26.50
CaO	0.32	0.19	0.30	0.17	0.26	0.18	0.20	0.15	0.14
Na2O	0.06	0.09	0.00	0.01	0.00	0.01	0.01	0.01	0.04
K2O	0.00	0.02	0.03	0.00	0.00	0.00	0.03	0.00	0.03
V2O3	0.03	0.10	0.02	0.04	0.02	0.03	0.08	0.02	0.02
Total	98.95	98.96	99.10	99.11	99.27	99.29	99.40	99.41	99.43
Number of cations per 6 oxygens									
Si	2.01	2.00	2.01	1.98	2.00	2.00	2.00	1.99	1.99
Al iv	-0.01	0.00	-0.01	0.02	0.00	0.00	0.00	0.01	0.01
Al vi	0.02	0.02	0.03	0.01	0.03	0.02	0.02	0.03	0.04
Fe iii	0.00	0.00	0.00	0.00	0.00	0.00	0.00	0.00	0.00
Cr	0.00	0.00	0.00	0.00	0.00	0.00	0.00	0.00	0.00
Ti	0.00	0.00	0.00	0.01	0.00	0.00	0.00	0.00	0.00
Fe ii	0.61	0.61	0.59	0.59	0.57	0.57	0.57	0.51	0.50
Mn	0.00	0.01	0.01	0.01	0.01	0.01	0.01	0.01	0.01
Mg	1.34	1.32	1.33	1.38	1.36	1.38	1.38	1.43	1.43
Ca	0.01	0.01	0.01	0.01	0.01	0.01	0.01	0.01	0.01
Na	0.00	0.01	0.00	0.00	0.00	0.00	0.00	0.00	0.00
K	0.00	0.00	0.00	0.00	0.00	0.00	0.00	0.00	0.00
total	3.98	3.99	3.98	4.00	3.98	3.99	3.99	3.99	3.98
Wo	0.64	0.39	0.61	0.34	0.53	0.35	0.39	0.29	0.27
En	68.19	67.76	68.55	69.57	69.87	69.99	70.09	73.28	73.84
Fs	31.17	31.85	30.84	30.10	29.60	29.66	29.52	26.43	25.89

wt%	OPX19	OPX20	OPX21	OPX22	OPX23	OPX24	OPX25	OPX26	OPX27
SiO2	54.35	54.28	54.00	54.72	54.02	54.04	54.52	54.58	54.35
Al2O3	0.52	0.69	0.80	2.09	0.57	0.44	0.39	0.53	0.44
FeO	18.81	19.37	18.88	15.31	19.18	20.03	19.32	18.63	19.57
Cr2O3	0.01	0.00	0.00	0.02	0.05	0.00	0.00	0.02	0.00
TiO2	0.03	0.06	0.04	0.00	0.14	0.05	0.07	0.07	0.00
NiO	0.15	0.09	0.10	0.09	0.10	0.17	0.08	0.20	0.13
MnO	0.21	0.27	0.15	0.08	0.36	0.36	0.32	0.22	0.28
MgO	25.30	24.55	25.43	27.24	24.98	24.46	24.97	25.35	25.08
CaO	0.13	0.19	0.21	0.10	0.29	0.22	0.17	0.31	0.16
Na2O	0.02	0.01	0.00	0.00	0.07	0.01	0.00	0.00	0.03
K2O	0.02	0.02	0.00	0.00	0.03	0.01	0.01	0.00	0.02
V2O3	0.00	0.02	0.04	0.03	0.00	0.00	0.00	0.00	0.00
Total	99.55	99.56	99.66	99.69	99.78	99.79	99.84	99.90	100.05
Number of cations per 6 oxygens									
Si	1.99	2.00	1.98	1.97	1.98	1.99	2.00	1.99	1.99
Al iv	0.01	0.00	0.02	0.03	0.02	0.01	0.00	0.01	0.01
Al vi	0.02	0.03	0.01	0.06	0.01	0.01	0.01	0.02	0.01
Fe iii	0.00	0.00	0.00	0.00	0.01	0.00	0.00	0.00	0.00
Cr	0.00	0.00	0.00	0.00	0.00	0.00	0.00	0.00	0.00
Ti	0.00	0.00	0.00	0.00	0.00	0.00	0.00	0.00	0.00
Fe ii	0.58	0.60	0.57	0.46	0.58	0.62	0.59	0.57	0.60
Mn	0.01	0.01	0.00	0.00	0.01	0.01	0.01	0.01	0.01
Mg	1.38	1.35	1.39	1.46	1.37	1.34	1.36	1.38	1.37
Ca	0.01	0.01	0.01	0.00	0.01	0.01	0.01	0.01	0.01
Na	0.00	0.00	0.00	0.00	0.00	0.00	0.00	0.00	0.00
K	0.00	0.00	0.00	0.00	0.00	0.00	0.00	0.00	0.00
total	3.99	3.99	4.00	3.99	4.00	3.99	3.99	3.99	4.00
Wo	0.26	0.39	0.42	0.19	0.58	0.44	0.33	0.61	0.32
En	70.13	68.69	70.15	75.73	69.11	67.83	69.11	70.10	69.04
Fs	29.61	30.92	29.44	24.08	30.32	31.73	30.56	29.29	30.64

wt%	OPX28	OPX29	OPX30	OPX31	OPX32	OPX33	OPX34	OPX35	OPX36
SiO2	54.62	54.51	54.66	55.33	54.97	54.62	55.09	54.31	54.74
Al2O3	0.56	0.19	0.73	0.80	0.58	0.48	0.56	1.03	0.45
FeO	19.64	20.15	19.89	16.28	18.63	19.41	19.23	19.78	18.98
Cr2O3	0.02	0.00	0.01	0.00	0.00	0.05	0.02	0.00	0.00
TiO2	0.00	0.08	0.09	0.02	0.01	0.00	0.00	0.01	0.00
NiO	0.09	0.08	0.06	0.16	0.11	0.08	0.11	0.12	0.10
MnO	0.27	0.15	0.21	0.12	0.27	0.31	0.21	0.31	0.21
MgO	24.59	24.62	24.28	27.35	25.61	25.25	25.19	24.77	25.83
CaO	0.13	0.31	0.18	0.13	0.16	0.18	0.15	0.18	0.20
Na2O	0.02	0.05	0.08	0.03	0.01	0.02	0.01	0.04	0.02
K2O	0.10	0.03	0.01	0.00	0.01	0.02	0.00	0.01	0.00
V2O3	0.05	0.02	0.04	0.04	0.00	0.00	0.00	0.00	0.05
Total	100.09	100.17	100.23	100.24	100.35	100.40	100.55	100.55	100.58

Number of cations per 6 oxygens

Si	2.00	2.00	2.00	1.99	2.00	1.99	2.00	1.98	1.99
Al iv	0.00	0.00	0.00	0.01	0.00	0.01	0.00	0.02	0.01
Al vi	0.02	0.01	0.03	0.02	0.02	0.01	0.02	0.03	0.01
Fe iii	0.00	0.00	0.00	0.00	0.00	0.00	0.00	0.00	0.01
Cr	0.00	0.00	0.00	0.00	0.00	0.00	0.00	0.00	0.00
Ti	0.00	0.00	0.00	0.00	0.00	0.00	0.00	0.00	0.00
Fe ii	0.60	0.62	0.61	0.49	0.57	0.59	0.59	0.60	0.57
Mn	0.01	0.00	0.01	0.00	0.01	0.01	0.01	0.01	0.01
Mg	1.34	1.35	1.32	1.47	1.39	1.37	1.36	1.35	1.40
Ca	0.01	0.01	0.01	0.00	0.01	0.01	0.01	0.01	0.01
Na	0.00	0.00	0.01	0.00	0.00	0.00	0.00	0.00	0.00
K	0.00	0.00	0.00	0.00	0.00	0.00	0.00	0.00	0.00
total	3.99	4.00	3.99	3.99	3.99	4.00	3.99	4.00	4.00
Wo	0.26	0.60	0.36	0.25	0.31	0.35	0.29	0.37	0.39
En	68.54	67.95	67.97	74.62	70.45	69.29	69.52	68.47	70.32
Fs	31.20	31.44	31.67	25.13	29.24	30.36	30.20	31.16	29.29

wt%	OPX37	OPX38
SiO2	55.38	56.25
Al2O3	0.39	0.54
FeO	19.25	18.50
Cr2O3	0.00	0.00
TiO2	0.00	0.05
NiO	0.13	0.11
MnO	0.27	0.19
MgO	24.93	25.69
CaO	0.27	0.34
Na2O	0.04	0.27
K2O	0.01	0.08
V2O3	0.01	0.09
Total	100.67	102.11

Number of cations per 6 oxygens

Si	2.01	2.01
Al iv	-0.01	-0.01
Al vi	0.03	0.03
Fe iii	0.00	0.00
Cr	0.00	0.00
Ti	0.00	0.00
Fe ii	0.59	0.55
Mn	0.01	0.01
Mg	1.35	1.37
Ca	0.01	0.01
Na	0.00	0.02
K	0.00	0.00
total	3.98	3.99
Wo	0.53	0.66
En	69.03	70.50
Fs	30.44	28.83

wt%	SCP1	SCP2	SCP3	SCP4	SCP5	SCP6	SCP7	SCP8	SCP9
SiO2	54.37	56.93	57.52	57.49	58.02	57.33	57.78	58.80	58.12
Al2O3	20.99	22.12	21.97	21.55	23.05	22.44	21.62	21.59	21.29
FeO	2.21	0.09	0.35	0.39	0.14	0.03	0.14	0.03	0.20
Cr2O3	0.07	0.00	0.00	0.04	0.01	0.01	0.00	0.04	0.06
TiO2	0.00	0.00	0.08	0.13	0.02	0.10	0.08	0.00	0.00
NiO	0.09	0.03	0.00	0.00	0.00	0.05	0.00	0.00	0.11
MnO	0.12	0.00	0.10	0.00	0.00	0.00	0.02	0.11	0.02
MgO	2.25	0.00	0.23	0.25	0.00	0.03	0.00	0.01	0.11
CaO	4.96	5.24	4.70	4.53	5.78	5.33	4.71	4.31	4.50
Na2O	9.77	11.05	11.08	10.58	11.02	10.90	11.04	10.47	10.82
K2O	0.58	0.57	0.82	0.92	0.58	0.65	0.80	0.76	0.85
Cl	3.02	3.30	3.31	3.32	3.32	3.33	3.34	3.35	3.35
F	0.00	0.00	0.00	0.00	0.00	0.00	0.00	0.00	0.00
SO3	n.a	n.a	n.a	n.a	n.a	n.a	n.a	n.a	n.a
V2O3	0.00	0.00	0.00	0.04	0.01	0.07	0.01	0.00	0.00
Total	98.43	99.32	100.16	99.23	101.95	100.26	99.53	99.46	99.43

Number of cations per 24 oxygens

Si	8.25	8.23	8.27	8.31	8.17	8.20	8.32	8.38	8.38
Al	3.75	3.77	3.72	3.67	3.83	3.78	3.67	3.62	3.62
Cr	0.01	0.00	0.00	0.00	0.00	0.00	0.00	0.00	0.01
Ti	0.00	0.00	0.01	0.01	0.00	0.01	0.01	0.00	0.00
Fe	0.28	0.01	0.04	0.05	0.02	0.00	0.02	0.00	0.02
Mn	0.02	0.00	0.01	0.00	0.00	0.00	0.00	0.01	0.00
Mg	0.51	0.00	0.05	0.05	0.00	0.01	0.00	0.00	0.02
Ca	0.81	0.81	0.72	0.70	0.87	0.82	0.73	0.66	0.69
Na	2.87	3.10	3.09	2.96	3.01	3.02	3.08	2.89	3.03
K	0.11	0.11	0.15	0.17	0.10	0.12	0.15	0.14	0.16
Cl	0.77	0.82	0.82	0.83	0.81	0.82	0.83	0.83	0.83
F	0.00	0.00	0.00	0.00	0.00	0.00	0.00	0.00	0.00
CO3*	0.23	0.18	0.18	0.17	0.19	0.18	0.17	0.17	0.17
SO3	0.00	0.00	0.00	0.00	0.00	0.00	0.00	0.00	0.00
total	17.60	17.03	17.06	16.94	17.00	16.97	16.97	16.71	16.94
%me	0.35	0.20	0.20	0.20	0.22	0.21	0.19	0.18	0.19
EqAn	25.06	25.64	24.08	22.41	27.53	26.16	22.33	20.81	20.60

wt%	SCP18	SCP19	SCP2	SCP20	SCP21	SCP22	SCP23	SCP24	SCP25
SiO2	57.63	56.77	56.78	58.05	58.61	57.81	57.07	58.19	58.09
Al2O3	21.63	22.24	21.01	21.60	21.57	21.35	22.47	21.86	21.47
FeO	0.54	0.05	1.14	0.07	0.08	0.19	0.07	0.05	0.03
Cr2O3	0.04	0.02	0.00	0.00	0.02	0.00	0.01	0.05	0.00
TiO2	0.00	0.00	0.01	0.01	0.00	0.01	0.00	0.00	0.09
NiO	0.06	0.00	0.05	0.00	0.02	0.01	0.03	0.04	0.00
MnO	0.01	0.00	0.00	0.03	0.00	0.00	0.00	0.00	0.01
MgO	0.31	0.06	0.95	0.02	0.01	0.00	0.00	0.01	0.00
CaO	4.71	5.33	4.42	4.50	4.42	4.71	5.71	4.77	4.70
Na2O	10.87	10.83	10.46	11.31	11.57	11.53	10.86	11.38	10.69
K2O	0.93	0.67	0.88	0.84	0.90	0.64	0.59	0.59	0.98
Cl	3.36	3.36	3.11	3.37	3.37	3.38	3.38	3.39	3.39
F	0.00	0.00	0.00	0.00	0.00	0.00	0.00	0.00	0.00
SO3	n.a	n.a	n.a	n.a	n.a	n.a	n.a	n.a	n.a
V2O3	0.00	0.00	0.00	0.00	0.01	0.03	0.07	0.05	0.07
Total	100.09	99.33	98.79	99.80	100.58	99.67	100.26	100.37	99.50

Number of cations per 24 oxygens

Si	8.32	8.21	8.36	8.34	8.37	8.36	8.20	8.32	8.35
Al	3.68	3.79	3.64	3.66	3.63	3.64	3.80	3.68	3.64
Cr	0.00	0.00	0.00	0.00	0.00	0.00	0.00	0.01	0.00
Ti	0.00	0.00	0.00	0.00	0.00	0.00	0.00	0.00	0.01
Fe	0.07	0.01	0.14	0.01	0.01	0.02	0.01	0.01	0.00
Mn	0.00	0.00	0.00	0.00	0.00	0.00	0.00	0.00	0.00
Mg	0.07	0.01	0.21	0.00	0.00	0.00	0.00	0.00	0.00
Ca	0.73	0.83	0.70	0.69	0.68	0.73	0.88	0.73	0.72
Na	3.04	3.04	2.98	3.15	3.20	3.23	3.02	3.15	2.98
K	0.17	0.12	0.16	0.15	0.16	0.12	0.11	0.11	0.18
Cl	0.83	0.84	0.78	0.84	0.83	0.84	0.84	0.84	0.84
F	0.00	0.00	0.00	0.00	0.00	0.00	0.00	0.00	0.00
CO3*	0.17	0.16	0.22	0.16	0.17	0.16	0.16	0.16	0.16
SO3	0.00	0.00	0.00	0.00	0.00	0.00	0.00	0.00	0.00
total	17.08	17.01	17.19	17.01	17.06	17.10	17.02	17.00	16.89
%me	0.21	0.21	0.25	0.18	0.17	0.18	0.22	0.18	0.19
EqAn	22.68	26.34	21.43	21.91	21.00	21.26	26.76	22.73	21.25

SCP20	SCP21	SCP22	SCP23	SCP24	SCP25	SCP26	SCP27	SCP28	SCP29
SiO2	57.68	55.13	55.42	56.48	57.79	55.60	56.37	58.04	55.98
Al2O3	21.15	21.86	22.21	21.56	21.08	22.26	21.55	21.34	21.95
FeO	0.05	0.02	0.02	0.03	0.45	0.10	0.06	0.04	0.05
Cr2O3	0.00	0.00	0.01	0.05	0.00	0.00	0.02	0.00	0.07
TiO2	0.00	0.00	0.00	0.00	0.11	0.00	0.00	0.04	0.10
NiO	0.04	0.05	0.03	0.00	0.00	0.08	0.00	0.00	0.04
MnO	0.00	0.00	0.00	0.06	0.03	0.00	0.03	0.00	0.01
MgO	0.00	0.00	0.00	0.00	0.35	0.00	0.03	0.00	0.02
CaO	4.89	6.30	6.43	5.75	4.75	6.34	5.92	4.39	6.05
Na2O	10.88	10.25	9.96	10.31	10.68	10.17	10.74	10.85	10.51
K2O	0.83	0.61	0.63	0.64	0.81	0.63	0.64	0.88	0.64
Cl	3.39	3.66	3.65	3.73	3.24	3.76	3.71	3.43	3.68
F	0.00	0.00	0.00	0.00	0.00	0.00	0.00	0.00	0.00
SO3	n.a	0.05	0.04	0.06	n.a	0.02	0.00	n.a	0.04
V2O3	0.02	0.05	0.03	0.00	0.00	0.00	0.00	0.01	0.01
Total	98.92	97.98	98.43	98.65	99.27	98.95	99.07	99.02	99.15

Number of cations per 24 oxygens

Si	8.38	8.18	8.15	8.28	8.38	8.15	8.27	8.37	8.20
Al	3.62	3.82	3.85	3.72	3.60	3.85	3.73	3.63	3.79
Cr	0.00	0.00	0.00	0.01	0.00	0.00	0.00	0.00	0.01
Ti	0.00	0.00	0.00	0.00	0.01	0.00	0.00	0.00	0.01
Fe	0.01	0.00	0.00	0.00	0.05	0.01	0.01	0.01	0.01
Mn	0.00	0.00	0.00	0.01	0.00	0.00	0.00	0.00	0.00
Mg	0.00	0.00	0.00	0.00	0.08	0.00	0.01	0.00	0.00
Ca	0.76	1.00	1.01	0.90	0.74	1.00	0.93	0.68	0.95
Na	3.07	2.95	2.84	2.93	3.00	2.89	3.06	3.03	2.98
K	0.15	0.12	0.12	0.12	0.15	0.12	0.12	0.16	0.12
Cl	0.85	0.93	0.92	0.94	0.81	0.95	0.93	0.86	0.93
F	0.00	0.00	0.00	0.00	0.00	0.00	0.00	0.00	0.00
CO3*	0.15	0.06	0.07	0.05	0.20	0.05	0.07	0.14	0.07
SO3	0.00	0.01	0.00	0.01	0.00	0.00	0.00	0.00	0.00
total	16.99	17.07	16.97	16.97	17.02	17.02	17.13	16.88	17.07
%me	0.19	0.25	0.26	0.23	0.22	0.25	0.23	0.18	0.24
EqAn	20.69	27.40	28.29	24.13	20.14	28.23	24.24	20.89	26.30

SCP30	SCP31	SCP32	SCP33	SCP34	SCP35	SCP36	SCP37	SCP38	SCP39
SiO2	56.25	58.17	57.66	57.13	56.48	58.10	56.46	56.77	57.86
Al2O3	21.78	21.35	21.44	22.06	22.06	21.41	22.25	22.06	21.68
FeO	0.08	0.02	0.17	0.00	0.04	0.01	0.00	0.08	0.16
Cr2O3	0.00	0.05	0.11	0.01	0.12	0.01	0.00	0.02	0.00
TiO2	0.03	0.00	0.01	0.12	0.00	0.00	0.14	0.00	0.06
NiO	0.10	0.03	0.03	0.00	0.00	0.01	0.00	0.02	0.06
MnO	0.12	0.00	0.00	0.00	0.00	0.08	0.00	0.00	0.04
MgO	0.00	0.00	0.06	0.00	0.03	0.04	0.00	0.03	0.02
CaO	5.63	4.59	4.80	5.25	6.05	4.67	5.53	5.77	4.78
Na2O	10.82	10.92	11.12	10.85	10.51	11.16	10.78	10.66	11.06
K2O	0.71	0.86	0.69	0.64	0.65	0.79	0.66	0.70	0.79
Cl	3.81	3.48	3.43	3.47	3.71	3.45	3.26	3.83	3.48
F	0.00	0.00	0.00	0.00	0.00	0.00	0.00	0.00	0.00
SO3	0.06	n.a	n.a	n.a	0.06	n.a	n.a	0.03	n.a
V2O3	0.01	0.00	0.00	0.00	0.04	0.00	0.00	0.04	0.03
Total	99.38	99.47	99.51	99.52	99.74	99.71	99.08	100.01	100.02
Number of cations per 24 oxygens									
Si	8.24	8.38	8.34	8.24	8.22	8.37	8.18	8.23	8.32
Al	3.76	3.62	3.66	3.75	3.78	3.63	3.80	3.77	3.67
Cr	0.00	0.01	0.01	0.00	0.01	0.00	0.00	0.00	0.00
Ti	0.00	0.00	0.00	0.01	0.00	0.00	0.02	0.00	0.01
Fe	0.01	0.00	0.02	0.00	0.00	0.00	0.00	0.01	0.02
Mn	0.01	0.00	0.00	0.00	0.00	0.01	0.00	0.00	0.00
Mg	0.00	0.00	0.01	0.00	0.01	0.01	0.00	0.01	0.00
Ca	0.88	0.71	0.74	0.81	0.94	0.72	0.86	0.90	0.74
Na	3.07	3.05	3.12	3.03	2.96	3.12	3.03	3.00	3.08
K	0.13	0.16	0.13	0.12	0.12	0.14	0.12	0.13	0.15
Cl	0.96	0.87	0.85	0.87	0.93	0.86	0.81	0.96	0.86
F	0.00	0.00	0.00	0.00	0.00	0.00	0.00	0.00	0.00
CO3*	0.03	0.13	0.15	0.13	0.07	0.14	0.13	0.04	0.14
SO3	0.01	0.00	0.00	0.00	0.01	0.00	0.00	0.00	0.00
total	17.11	16.92	17.04	16.96	17.05	17.00	16.95	17.04	16.99
%me	0.22	0.18	0.19	0.20	0.24	0.18	0.21	0.23	0.19
EqAn	25.30	20.78	21.86	24.95	26.09	21.11	26.68	25.66	22.44

SCP40	SCP41	SCP42	SCP43	SCP44	SCP45	SCP46	SCP47	SCP48
SiO2	58.44	56.82	57.83	56.56	55.83	56.57	58.11	57.15
Al2O3	21.13	22.65	22.32	22.69	22.62	22.78	21.09	22.01
FeO	0.18	0.20	0.03	0.27	0.08	0.02	0.02	0.08
Cr2O3	0.00	0.00	0.00	0.00	0.00	0.12	0.00	0.11
TiO2	0.15	0.00	0.08	0.00	0.02	0.24	0.07	0.00
NiO	0.00	0.01	0.03	0.06	0.00	0.00	0.01	0.08
MnO	0.00	0.00	0.00	0.00	0.00	0.00	0.00	0.04
MgO	0.01	0.02	0.01	0.02	0.10	0.00	0.01	0.01
CaO	4.72	5.56	5.26	5.67	5.86	5.88	4.49	5.12
Na2O	11.25	10.96	11.07	10.80	10.38	10.32	10.87	11.16
K2O	0.80	0.62	0.64	0.58	0.56	0.64	0.87	0.63
Cl	3.40	3.40	3.52	3.28	3.28	3.28	3.29	3.29
F	0.00	0.00	0.00	0.00	0.00	0.00	0.00	0.00
SO3	n.a	n.a	n.a	n.a	n.a	n.a	n.a	n.a
V2O3	0.00	0.00	0.03	0.00	0.06	0.01	0.06	0.00
Total	100.08	100.24	100.81	99.91	98.79	99.85	98.89	99.68

Number of cations per 24 oxygens

Si	8.40	8.16	8.24	8.15	8.12	8.12	8.40	8.25
Al	3.58	3.84	3.75	3.85	3.88	3.85	3.59	3.75
Cr	0.00	0.00	0.00	0.00	0.00	0.01	0.00	0.01
Ti	0.02	0.00	0.01	0.00	0.00	0.03	0.01	0.00
Fe	0.02	0.02	0.00	0.03	0.01	0.00	0.00	0.01
Mn	0.00	0.00	0.00	0.00	0.00	0.00	0.00	0.00
Mg	0.00	0.00	0.00	0.00	0.02	0.00	0.00	0.00
Ca	0.73	0.86	0.80	0.87	0.91	0.90	0.70	0.79
Na	3.13	3.05	3.06	3.02	2.93	2.87	3.05	3.12
K	0.15	0.11	0.12	0.11	0.10	0.12	0.16	0.12
Cl	0.84	0.84	0.87	0.81	0.82	0.81	0.82	0.82
F	0.00	0.00	0.00	0.00	0.00	0.00	0.00	0.00
CO3*	0.16	0.16	0.13	0.19	0.18	0.18	0.12	0.18
SO3	0.00	0.00	0.00	0.00	0.00	0.00	0.00	0.00
total	17.03	17.05	16.98	17.04	16.98	16.90	16.85	17.06
%me	0.19	0.22	0.20	0.23	0.24	0.23	0.18	0.20
EqAn	19.37	27.85	24.95	28.39	29.27	28.48	19.74	24.85

wt%	ANF 1	ANF 2	ANF 3	ANF 4	ANF 5	ANF 6	ANF 7	ANF 8	ANF 9
SiO2	45.90	44.10	46.17	45.79	43.71	44.31	43.87	42.57	45.42
Al2O3	8.12	10.54	8.95	10.07	10.70	10.55	10.68	12.70	9.30
FeO	13.46	12.22	11.49	10.25	11.64	12.16	12.64	10.67	11.11
Cr2O3	0.01	0.06	0.06	0.01	0.00	0.05	0.11	0.19	0.13
TiO2	0.86	0.76	1.06	0.57	1.00	0.87	0.61	0.80	1.05
NiO	0.10	0.16	0.17	0.15	0.18	0.21	0.26	0.19	0.24
MnO	0.22	0.00	0.13	0.09	0.02	0.06	0.11	0.08	0.08
MgO	13.77	13.97	15.18	14.92	14.02	14.22	13.88	14.17	14.61
CaO	11.36	9.81	10.11	10.01	10.51	10.29	10.22	10.50	9.90
Na2O	1.79	2.25	1.97	2.36	2.20	2.22	2.38	2.64	2.21
K2O	0.59	0.87	0.56	0.64	0.87	0.86	0.92	0.83	0.64
Cl	0.82	1.07	0.86	0.77	1.27	1.14	1.15	1.00	1.10
F	0.45	0.64	0.80	0.84	0.57	0.66	0.68	0.77	0.73
V2O3	0.18	0.10	0.09	0.08	0.14	0.07	0.15	0.03	0.05
Total	97.26	96.04	97.06	96.01	96.29	97.13	97.10	96.59	96.03

Number of cations per 23 Oxygens

Si	6.77	6.49	6.67	6.68	6.47	6.47	6.44	6.25	6.66
Al iv	1.23	1.51	1.33	1.32	1.53	1.53	1.56	1.75	1.34
Al vi	0.18	0.32	0.19	0.41	0.33	0.29	0.29	0.45	0.27
Feiii	0.65	1.11	1.13	0.86	0.85	1.04	1.06	0.90	0.96
Cr	0.00	0.01	0.01	0.00	0.00	0.01	0.01	0.02	0.01
Ti	0.10	0.08	0.11	0.06	0.11	0.10	0.07	0.09	0.12
Feii	1.01	0.39	0.26	0.39	0.59	0.45	0.49	0.41	0.41
Mn	0.03	0.00	0.02	0.01	0.00	0.01	0.01	0.01	0.01
Mg	3.03	3.07	3.27	3.24	3.09	3.10	3.04	3.10	3.20
Ca	1.79	1.55	1.56	1.57	1.67	1.61	1.61	1.65	1.56
Na	0.51	0.64	0.55	0.67	0.63	0.63	0.68	0.75	0.63
K	0.11	0.16	0.10	0.12	0.16	0.16	0.17	0.15	0.12
Cl	0.20	0.27	0.21	0.19	0.32	0.28	0.28	0.25	0.27
F	0.21	0.30	0.36	0.39	0.26	0.30	0.32	0.36	0.34
OH*	1.59	1.44	1.43	1.42	1.42	1.42	1.40	1.39	1.39
Total	17.42	17.35	17.22	17.35	17.46	17.40	17.46	17.56	17.31
Na+K	0.62	0.81	0.65	0.78	0.79	0.79	0.85	0.91	0.75
Altotal	1.41	1.83	1.52	1.73	1.87	1.82	1.85	2.20	1.61
Xfe	0.35	0.33	0.30	0.28	0.32	0.32	0.34	0.30	0.30

wt%	ANF 10	ANF 11	ANF 12	ANF 13	ANF 14	ANF 15	ANF 16	ANF 17	ANF 18
SiO2	43.90	45.37	48.81	44.20	46.97	45.50	44.59	42.57	43.65
Al2O3	10.60	9.73	6.51	10.31	9.96	9.79	10.05	12.73	10.55
FeO	11.91	10.57	9.83	12.14	10.37	11.70	11.14	10.06	11.27
Cr2O3	0.00	0.06	0.02	0.00	0.02	0.05	0.02	0.14	0.00
TiO2	0.63	0.56	0.97	0.88	0.49	0.64	0.72	0.90	1.27
NiO	0.21	0.19	0.25	0.15	0.20	0.13	0.21	0.14	0.15
MnO	0.03	0.07	0.09	0.12	0.00	0.07	0.01	0.00	0.09
MgO	14.12	15.08	16.59	13.81	16.24	14.75	14.71	14.29	14.41
CaO	11.38	10.30	10.11	11.33	10.22	10.21	10.20	10.73	10.25
Na2O	1.96	2.21	1.66	2.43	2.38	2.53	2.42	2.63	2.49
K2O	0.93	0.65	0.45	0.83	0.62	0.61	0.70	0.83	0.76
Cl	0.92	0.78	0.45	1.08	0.66	0.79	0.90	0.88	0.94
F	0.83	0.94	0.68	0.79	1.08	0.98	0.94	0.95	0.95
V2O3	0.18	0.12	0.14	0.07	0.10	0.09	0.21	0.09	0.09
Total	97.04	96.06	96.16	97.55	98.70	97.23	96.22	96.32	96.26
Number of cations per 23 Oxygens									
Si	6.48	6.64	7.02	6.53	6.63	6.61	6.56	6.28	6.44
Al iv	1.52	1.36	0.98	1.47	1.37	1.39	1.44	1.72	1.56
Al vi	0.32	0.32	0.12	0.33	0.28	0.29	0.30	0.49	0.27
Feiii	0.72	0.94	1.00	0.51	1.13	0.96	0.95	0.73	0.92
Cr	0.00	0.01	0.00	0.00	0.00	0.01	0.00	0.02	0.00
Ti	0.07	0.06	0.10	0.10	0.05	0.07	0.08	0.10	0.14
Feii	0.75	0.36	0.19	0.99	0.09	0.46	0.42	0.51	0.47
Mn	0.00	0.01	0.01	0.01	0.00	0.01	0.00	0.00	0.01
Mg	3.11	3.29	3.55	3.04	3.42	3.19	3.22	3.14	3.17
Ca	1.80	1.61	1.56	1.79	1.54	1.59	1.61	1.69	1.62
Na	0.56	0.63	0.46	0.69	0.65	0.71	0.69	0.75	0.71
K	0.17	0.12	0.08	0.16	0.11	0.11	0.13	0.16	0.14
Cl	0.23	0.19	0.11	0.27	0.16	0.19	0.22	0.22	0.23
F	0.39	0.43	0.31	0.37	0.48	0.45	0.44	0.44	0.44
OH*	1.38	1.37	1.58	1.36	1.36	1.36	1.34	1.34	1.32
Total	17.53	17.36	17.10	17.64	17.31	17.41	17.43	17.60	17.47
Na+K	0.73	0.75	0.55	0.85	0.76	0.82	0.82	0.91	0.86
Altotal	1.84	1.68	1.10	1.80	1.66	1.68	1.74	2.21	1.83
Xfe	0.32	0.28	0.25	0.33	0.26	0.31	0.30	0.28	0.30

wt%	ANF 19	ANF 20	ANF 21	ANF 22	ANF 23	ANF 24	ANF 25	ANF 26	ANF 27
SiO2	43.09	44.19	42.46	45.23	48.80	45.48	44.01	45.11	43.70
Al2O3	10.47	9.97	11.70	9.95	6.76	9.98	10.68	10.17	10.01
FeO	12.99	12.43	12.68	10.95	9.22	11.41	12.16	11.33	12.26
Cr2O3	0.02	0.00	0.06	0.00	0.00	0.09	0.06	0.08	0.00
TiO2	1.36	0.76	0.50	0.71	0.72	0.72	0.80	0.89	0.87
NiO	0.19	0.22	0.15	0.12	0.21	0.14	0.22	0.12	0.23
MnO	0.03	0.10	0.01	0.04	0.03	0.12	0.12	0.02	0.08
MgO	13.38	13.90	13.48	14.74	17.05	14.48	13.92	14.53	13.89
CaO	10.52	10.71	10.24	10.23	10.36	10.42	11.15	10.33	10.89
Na2O	2.15	2.01	2.59	2.41	1.60	2.43	2.38	2.53	2.34
K2O	1.21	0.87	0.96	0.70	0.49	0.68	0.90	0.67	0.77
Cl	1.33	1.30	1.36	0.93	0.64	0.97	1.06	0.85	1.15
F	0.74	0.77	0.74	0.99	0.59	1.00	0.96	1.09	0.93
V2O3	0.16	0.13	0.16	0.13	0.08	0.06	0.14	0.23	0.14
Total	97.03	96.75	96.47	96.49	96.15	97.33	97.91	97.29	96.58
Number of cations per 23 Oxygens									
Si	6.41	6.54	6.31	6.63	7.00	6.63	6.47	6.58	6.50
Al iv	1.59	1.46	1.69	1.37	1.00	1.37	1.53	1.42	1.50
Al vi	0.24	0.27	0.36	0.34	0.14	0.34	0.32	0.33	0.26
Feiii	0.85	0.88	1.03	0.85	0.98	0.79	0.67	0.81	0.75
Cr	0.00	0.00	0.01	0.00	0.00	0.01	0.01	0.01	0.00
Ti	0.15	0.08	0.06	0.08	0.08	0.08	0.09	0.10	0.10
Feii	0.77	0.65	0.55	0.50	0.12	0.60	0.82	0.57	0.77
Mn	0.00	0.01	0.00	0.00	0.00	0.01	0.02	0.00	0.01
Mg	2.96	3.06	2.99	3.22	3.65	3.15	3.05	3.16	3.08
Ca	1.68	1.70	1.63	1.61	1.59	1.63	1.76	1.62	1.74
Na	0.62	0.58	0.75	0.69	0.44	0.69	0.68	0.71	0.67
K	0.23	0.16	0.18	0.13	0.09	0.13	0.17	0.12	0.15
Cl	0.34	0.33	0.34	0.23	0.16	0.24	0.26	0.21	0.29
F	0.35	0.36	0.35	0.46	0.27	0.46	0.45	0.50	0.44
OH*	1.31	1.31	1.31	1.31	1.58	1.30	1.29	1.29	1.27
Total	17.52	17.44	17.56	17.42	17.13	17.44	17.60	17.45	17.56
Na+K	0.85	0.74	0.93	0.82	0.53	0.81	0.85	0.84	0.82
Altotal	1.83	1.74	2.05	1.72	1.14	1.71	1.85	1.75	1.75
Xfe	0.35	0.33	0.35	0.29	0.23	0.31	0.33	0.30	0.33

wt%	ANF 28	ANF 29	ANF 30	ANF 31	ANF 32	ANF 33	ANF 34	ANF 35	ANF 36
SiO2	43.94	40.22	40.22	55.15	56.94	56.14	46.26	55.69	55.80
Al2O3	10.46	12.08	13.11	0.37	0.46	0.64	9.39	0.84	1.06
FeO	12.47	16.96	16.49	16.29	9.29	11.54	11.59	11.17	10.23
Cr2O3	0.07	0.05	0.07	0.11	0.00	0.01	0.00	0.03	0.00
TiO2	0.65	0.66	1.04	0.00	0.05	0.10	0.58	0.19	0.11
NiO	0.18	0.19	0.20	0.51	0.08	0.45	0.14	0.44	0.24
MnO	0.05	0.02	0.02	0.40	0.18	0.09	0.06	0.15	0.11
MgO	13.99	10.01	9.67	12.96	18.34	16.25	14.84	16.49	17.42
CaO	11.24	10.24	10.15	10.69	11.38	11.11	10.07	11.05	11.12
Na2O	2.24	2.06	2.33	0.07	0.10	0.13	1.93	0.23	0.11
K2O	0.88	1.22	1.33	0.05	0.06	0.02	0.61	0.04	0.02
Cl	1.10	2.66	2.64	0.01	0.05	0.01	0.81	0.02	0.03
F	0.98	0.26	0.28	0.00	0.00	0.00	0.51	0.00	0.00
V2O3	0.16	0.20	0.03	0.00	0.10	0.00	0.20	0.02	0.00
Total	97.74	96.11	96.87	96.61	97.02	96.48	96.57	96.35	96.23
Number of cations per 23 Oxygens									
Si	6.47	6.21	6.16	8.02	7.97	7.99	6.70	7.93	7.89
Al iv	1.53	1.79	1.84	0.00	0.03	0.01	1.30	0.07	0.11
Al vi	0.29	0.40	0.52	0.06	0.05	0.10	0.30	0.07	0.07
Feiii	0.74	0.99	0.79	0.52	0.52	0.45	1.09	0.50	0.62
Cr	0.01	0.01	0.01	0.01	0.00	0.00	0.00	0.00	0.00
Ti	0.07	0.08	0.12	0.00	0.01	0.01	0.06	0.02	0.01
Feii	0.80	1.19	1.32	1.47	0.57	0.92	0.32	0.83	0.59
Mn	0.01	0.00	0.00	0.05	0.02	0.01	0.01	0.02	0.01
Mg	3.07	2.30	2.21	2.81	3.83	3.45	3.21	3.50	3.67
Ca	1.77	1.69	1.66	1.67	1.71	1.69	1.56	1.69	1.68
Na	0.64	0.62	0.69	0.02	0.03	0.04	0.54	0.06	0.03
K	0.17	0.24	0.26	0.01	0.01	0.00	0.11	0.01	0.00
Cl	0.27	0.70	0.69	0.00	0.01	0.00	0.20	0.01	0.01
F	0.46	0.13	0.14	0.00	0.00	0.00	0.23	0.00	0.00
OH*	1.27	1.18	1.18	2.00	1.99	2.00	1.57	1.99	1.99
Total	17.58	17.55	17.61	16.70	16.74	16.73	17.22	16.76	16.72
Na+K	0.81	0.86	0.95	0.03	0.04	0.04	0.65	0.07	0.03
Altotal	1.82	2.20	2.37	0.06	0.08	0.11	1.60	0.14	0.18
Xfe	0.33	0.49	0.49	0.41	0.22	0.28	0.30	0.28	0.25

wt%	ANF 37	ANF 38	ANF 39	ANF 40	ANF 41	ANF 42	ANF 43	ANF 44	ANF 45
SiO2	55.65	54.63	56.78	55.45	54.17	52.38	53.56	53.41	43.42
Al2O3	1.07	1.36	1.75	2.10	2.16	2.80	3.22	3.61	10.77
FeO	10.41	13.11	5.60	6.20	12.60	14.76	8.53	7.39	13.22
Cr2O3	0.10	0.06	0.00	0.05	0.07	0.00	0.02	0.00	0.00
TiO2	0.27	0.26	0.18	0.05	0.15	0.32	0.23	0.25	1.00
NiO	0.24	0.15	0.23	0.34	0.17	0.18	0.16	0.10	0.25
MnO	0.10	0.26	0.03	0.09	0.19	0.15	0.12	0.11	0.15
MgO	16.93	15.24	20.38	20.62	15.53	13.88	18.82	19.12	13.37
CaO	11.32	10.88	10.72	11.87	11.00	10.51	10.64	10.51	10.11
Na2O	0.23	0.22	0.31	0.50	0.53	0.39	0.59	0.81	2.42
K2O	0.04	0.04	0.12	0.13	0.20	0.21	0.20	0.13	0.77
Cl	0.03	0.09	0.14	0.13	0.19	0.54	0.49	0.22	1.05
F	0.00	0.00	0.45	0.53	0.13	0.00	0.37	0.68	0.50
V2O3	0.01	0.16	0.07	0.00	0.00	0.19	0.09	0.10	0.08
Total	96.38	96.43	96.54	98.66	96.99	96.18	96.78	96.11	96.66
Number of cations per 23 Oxygens									
Si	7.91	7.85	7.85	7.65	7.75	7.63	7.50	7.51	6.40
Al iv	0.09	0.15	0.15	0.34	0.25	0.37	0.50	0.49	1.60
Al vi	0.09	0.08	0.13	0.00	0.11	0.11	0.03	0.10	0.27
Feiii	0.40	0.60	0.65	0.68	0.54	0.75	1.00	0.87	1.07
Cr	0.01	0.01	0.00	0.01	0.01	0.00	0.00	0.00	0.00
Ti	0.03	0.03	0.02	0.01	0.02	0.04	0.02	0.03	0.11
Feii	0.83	0.98	0.00	0.03	0.97	1.04	0.00	0.00	0.56
Mn	0.01	0.03	0.00	0.01	0.02	0.02	0.01	0.01	0.02
Mg	3.59	3.26	4.20	4.24	3.31	3.02	3.93	4.01	2.94
Ca	1.72	1.67	1.59	1.75	1.69	1.64	1.60	1.58	1.60
Na	0.06	0.06	0.08	0.13	0.15	0.11	0.16	0.22	0.69
K	0.01	0.01	0.02	0.02	0.04	0.04	0.04	0.02	0.14
Cl	0.01	0.02	0.03	0.03	0.05	0.13	0.12	0.05	0.26
F	0.00	0.00	0.20	0.23	0.06	0.00	0.16	0.30	0.23
OH*	1.99	1.98	1.77	1.74	1.89	1.87	1.72	1.64	1.51
Total	16.79	16.74	16.72	16.91	16.87	16.79	16.81	16.86	17.43
Na+K	0.07	0.07	0.11	0.16	0.18	0.15	0.20	0.24	0.84
Altotal	0.18	0.23	0.29	0.34	0.36	0.48	0.53	0.60	1.87
Xfe	0.26	0.33	0.13	0.14	0.31	0.37	0.20	0.18	0.36

wt%	ANF 46	ANF 47	ANF 48	ANF 49	ANF 50	ANF 51	ANF 52
SiO2	52.75	50.77	50.28	45.04	44.16	44.38	44.53
Al2O3	3.84	5.48	6.06	10.13	10.74	9.70	10.43
FeO	8.13	9.63	9.32	10.40	12.82	12.77	12.51
Cr2O3	0.01	0.13	0.01	0.02	0.01	0.00	0.03
TiO2	0.52	0.59	0.55	0.91	1.14	0.93	0.89
NiO	0.23	0.08	0.24	0.27	0.27	0.11	0.20
MnO	0.06	0.07	0.13	0.08	0.09	0.00	0.06
MgO	18.95	16.85	17.47	14.98	13.51	13.94	13.83
CaO	10.30	10.60	10.08	10.53	9.96	11.13	9.94
Na2O	0.88	0.86	1.33	2.17	2.10	1.95	2.19
K2O	0.19	0.33	0.34	0.73	0.72	0.78	0.76
Cl	0.27	0.54	0.40	0.81	1.04	1.07	0.97
F	0.40	0.49	0.76	0.68	0.56	0.60	0.68
V2O3	0.05	0.08	0.12	0.10	0.08	0.14	0.09
Total	96.34	96.15	96.68	96.37	96.72	97.01	96.59
Number of cations per 23 Oxygens							
Si	7.41	7.25	7.12	6.58	6.46	6.55	6.52
Al iv	0.59	0.75	0.88	1.42	1.54	1.45	1.48
Al vi	0.04	0.17	0.13	0.32	0.32	0.24	0.32
Feiii	0.96	0.90	1.10	0.85	1.11	0.77	1.08
Cr	0.00	0.01	0.00	0.00	0.00	0.00	0.00
Ti	0.05	0.06	0.06	0.10	0.13	0.10	0.10
Feii	0.00	0.25	0.00	0.42	0.45	0.80	0.45
Mn	0.01	0.01	0.02	0.01	0.01	0.00	0.01
Mg	3.97	3.59	3.69	3.26	2.95	3.07	3.02
Ca	1.55	1.62	1.53	1.65	1.56	1.76	1.56
Na	0.24	0.24	0.36	0.62	0.60	0.56	0.62
K	0.03	0.06	0.06	0.14	0.13	0.15	0.14
Cl	0.06	0.13	0.10	0.20	0.26	0.27	0.24
F	0.18	0.22	0.34	0.31	0.26	0.28	0.31
OH*	1.76	1.65	1.56	1.49	1.48	1.45	1.45
Total	16.88	16.92	16.98	17.40	17.29	17.47	17.32
Na+K	0.27	0.30	0.43	0.75	0.73	0.71	0.76
Altotal	0.63	0.92	1.01	1.74	1.85	1.69	1.80
Xfe	0.19	0.24	0.23	0.28	0.35	0.34	0.34

wt%	FDS1	FDS2	FDS3	FDS4	FDS5	FDS6	FDS7	FDS8	FDS9
SiO2	68.66	69.58	67.69	63.09	63.84	63.53	63.32	62.81	63.01
Al2O3	19.28	19.28	18.88	21.70	22.51	22.36	22.41	22.41	22.44
FeO	0.02	0.05	1.55	0.87	0.16	0.07	0.03	0.09	0.01
Cr2O3	0.00	0.00	0.00	0.00	0.05	0.00	0.00	0.00	0.00
TiO2	0.00	0.00	0.00	0.06	0.02	0.00	0.14	0.12	0.07
NiO	0.09	0.00	0.00	0.00	0.06	0.06	0.00	0.00	0.00
MnO	0.03	0.00	0.00	0.02	0.00	0.01	0.00	0.03	0.00
MgO	0.02	0.00	0.32	0.47	0.00	0.02	0.00	0.00	0.00
CaO	0.13	0.15	0.42	3.09	3.68	3.74	3.81	3.79	3.82
Na2O	11.73	12.09	11.90	9.71	9.52	9.55	9.62	9.46	9.52
K2O	0.08	0.05	0.06	0.12	0.18	0.13	0.15	0.19	0.21
Cl	0.01	0.00	0.04	0.02	0.00	0.01	0.00	0.02	0.01
F	0.00	0.00	0.00	0.00	0.00	0.00	0.00	0.00	0.00
V2O3	0.00	0.00	0.04	0.05	0.00	0.00	0.02	0.04	0.00
Total	100.06	101.19	100.88	99.20	100.01	99.46	99.51	98.95	99.08
Number of cations per 32 Oxygens									
Si	12.01	12.02	11.90	11.33	11.29	11.30	11.30	11.24	11.25
Al	3.97	3.93	3.91	4.59	4.69	4.69	4.69	4.73	4.72
Ti	0.00	0.00	0.00	0.01	0.00	0.00	0.00	0.02	0.01
Fe(ii)	0.00	0.01	0.23	0.13	0.02	0.01	0.01	0.01	0.00
Ca	0.02	0.03	0.08	0.59	0.70	0.71	0.71	0.73	0.73
Na	3.98	4.05	4.05	3.38	3.27	3.29	3.29	3.28	3.29
K	0.02	0.01	0.01	0.03	0.04	0.03	0.03	0.04	0.05
TOTAL	20.00	20.04	20.18	20.07	20.01	20.02	20.02	20.04	20.05
An	0.62	0.66	1.93	14.84	17.42	17.65	17.65	17.93	17.94
Ab	98.95	99.10	97.77	84.49	81.55	81.64	81.64	81.01	80.90
Or	0.43	0.24	0.30	0.67	1.03	0.71	0.71	1.07	1.16

wt%	FDS10	FDS11	FDS12	FDS13	FDS14	FDS15	FDS16	FDS17	FDS18
SiO2	63.63	63.38	63.78	63.08	62.53	63.76	63.25	62.60	62.89
Al2O3	22.71	22.25	22.66	22.33	22.69	23.15	22.57	22.67	22.74
FeO	0.11	0.02	0.06	0.03	0.00	0.00	0.05	0.04	0.02
Cr2O3	0.02	0.00	0.06	0.08	0.00	0.00	0.00	0.00	0.07
TiO2	0.00	0.00	0.02	0.02	0.00	0.27	0.03	0.13	0.01
NiO	0.11	0.00	0.04	0.01	0.00	0.00	0.02	0.00	0.00
MnO	0.00	0.08	0.08	0.04	0.00	0.07	0.00	0.00	0.00
MgO	0.01	0.02	0.01	0.00	0.04	0.02	0.02	0.00	0.00
CaO	3.87	3.92	4.09	4.02	4.02	3.99	4.22	4.49	4.44
Na2O	9.64	9.19	9.45	9.27	9.24	9.18	9.42	9.08	8.94
K2O	0.17	0.17	0.17	0.19	0.17	0.10	0.21	0.24	0.26
Cl	0.00	0.00	0.01	0.01	0.00	0.02	0.02	0.00	0.01
F	0.00	0.00	0.00	0.00	0.00	0.00	0.00	0.00	0.00
V2O3	0.00	0.00	0.02	0.02	0.00	0.03	0.00	0.01	0.00
Total	100.28	99.04	100.45	99.09	98.70	100.59	99.79	99.29	99.37
Number of cations per 32 Oxygens									
Si	11.24	11.31	11.25	11.27	11.21	11.21	11.23	11.17	11.21
Al	4.73	4.68	4.71	4.70	4.79	4.79	4.72	4.77	4.78
Ti	0.00	0.00	0.00	0.00	0.00	0.04	0.00	0.02	0.00
Fe(ii)	0.02	0.00	0.01	0.00	0.00	0.00	0.01	0.01	0.00
Ca	0.73	0.75	0.77	0.77	0.77	0.75	0.80	0.86	0.85
Na	3.30	3.18	3.23	3.21	3.21	3.13	3.24	3.14	3.09
K	0.04	0.04	0.04	0.04	0.04	0.02	0.05	0.05	0.06
TOTAL	20.06	19.96	20.02	20.00	20.02	19.94	20.05	20.02	19.98
An	18.00	18.88	19.13	19.13	19.21	19.23	19.60	21.18	21.20
Ab	81.08	80.14	79.91	79.80	79.83	80.17	79.22	77.47	77.35
Or	0.91	0.98	0.97	1.07	0.96	0.59	1.17	1.34	1.45

wt%	FDS19	FDS20	FDS21	FDS22	FDS23	FDS24	FDS25	FDS26	FDS27
SiO2	62.02	60.69	60.02	60.11	60.48	60.19	58.39	59.33	59.15
Al2O3	22.65	24.80	24.35	25.77	23.73	24.81	24.72	24.83	24.80
FeO	0.03	0.07	0.19	0.13	0.30	0.15	0.37	0.03	0.10
Cr2O3	0.00	0.06	0.00	0.00	0.07	0.00	0.03	0.00	0.08
TiO2	0.12	0.22	0.00	0.16	0.21	0.07	0.00	0.03	0.20
NiO	0.01	0.00	0.03	0.09	0.06	0.00	0.03	0.00	0.00
MnO	0.01	0.01	0.00	0.09	0.01	0.04	0.01	0.00	0.06
MgO	0.00	0.01	0.02	0.00	0.00	0.00	0.00	0.01	0.02
CaO	4.57	5.46	5.58	6.58	5.96	6.08	7.22	7.24	7.23
Na2O	8.92	8.36	8.44	8.62	7.85	7.91	7.24	7.23	7.18
K2O	0.25	0.08	0.12	0.17	0.06	0.13	0.09	0.11	0.12
Cl	0.01	0.01	0.03	0.05	0.00	0.01	0.02	0.00	0.01
F	0.00	0.00	0.00	0.00	0.00	0.00	0.00	0.00	0.00
V2O3	0.00	0.02	0.00	0.08	0.00	0.01	0.04	0.00	0.00
Total	98.57	99.79	98.75	101.84	98.75	99.39	98.14	98.82	98.94
Number of cations per 32 Oxygens									
Si	11.15	10.81	10.82	10.59	10.90	10.78	10.64	10.70	10.68
Al	4.80	5.21	5.17	5.35	5.04	5.23	5.31	5.28	5.27
Ti	0.02	0.03	0.00	0.02	0.03	0.01	0.00	0.00	0.03
Fe(ii)	0.00	0.01	0.03	0.02	0.05	0.02	0.06	0.00	0.02
Ca	0.88	1.04	1.08	1.24	1.15	1.17	1.41	1.40	1.40
Na	3.11	2.89	2.95	2.94	2.74	2.75	2.56	2.53	2.51
K	0.06	0.02	0.03	0.04	0.01	0.03	0.02	0.02	0.03
TOTAL	20.02	20.01	20.08	20.20	19.93	19.99	19.99	19.93	19.93
An	21.74	26.41	26.57	29.39	29.46	29.57	35.36	35.40	35.48
Ab	76.84	73.11	72.76	69.68	70.19	69.65	64.11	63.97	63.81
Or	1.42	0.47	0.67	0.93	0.35	0.78	0.52	0.63	0.70

wt%	FDS28	FDS29	FDS30	FDS31	FDS32
SiO2	59.33	59.43	58.62	56.90	55.45
Al2O3	25.31	25.40	24.87	26.56	27.11
FeO	0.22	0.25	0.11	0.01	0.09
Cr2O3	0.02	0.01	0.04	0.00	0.07
TiO2	0.06	0.06	0.00	0.11	0.00
NiO	0.00	0.11	0.03	0.00	0.00
MnO	0.00	0.07	0.00	0.02	0.00
MgO	0.00	0.00	0.02	0.00	0.03
CaO	7.28	7.27	7.37	8.95	9.57
Na2O	7.13	7.10	6.98	5.88	5.66
K2O	0.08	0.10	0.06	0.05	0.08
Cl	0.01	0.02	0.00	0.01	0.00
F	0.00	0.00	0.00	0.00	0.00
V2O3	0.01	0.00	0.00	0.01	0.00
Total	99.45	99.85	98.15	98.52	98.05
Number of cations per 32 Oxygens					
Si	10.64	10.64	10.66	10.33	10.16
Al	5.35	5.36	5.33	5.68	5.85
Ti	0.01	0.01	0.00	0.01	0.00
Fe(ii)	0.03	0.04	0.02	0.00	0.01
Ca	1.40	1.39	1.44	1.74	1.88
Na	2.48	2.46	2.46	2.07	2.01
K	0.02	0.02	0.01	0.01	0.02
TOTAL	19.93	19.92	19.91	19.85	19.93
An	35.89	35.93	36.73	45.55	48.06
Ab	63.66	63.46	62.91	54.15	51.47
Or	0.45	0.61	0.36	0.30	0.48

wt%	CPX1	CPX2	CPX3	CPX4	CPX5	CPX6
SiO2	54.03	54.08	54.51	54.40	54.24	54.35
Al2O3	0.72	0.61	0.75	0.77	0.55	0.64
FeO	7.48	7.40	7.23	7.53	6.47	7.00
Cr2O3	0.00	0.00	0.04	0.00	0.06	0.02
TiO2	0.00	0.00	0.01	0.00	0.01	0.03
NiO	0.03	0.03	0.00	0.00	0.16	0.10
MnO	0.18	0.12	0.16	0.08	0.21	0.10
MgO	14.20	14.45	14.20	14.41	14.59	14.47
CaO	20.23	20.33	20.10	20.28	20.90	20.25
Na2O	0.50	0.57	0.54	0.69	0.49	0.64
K2O	0.02	0.01	0.03	0.06	0.02	0.02
V2O3	0.01	0.06	0.09	0.03	0.01	0.10
Total	97.38	97.65	97.64	98.25	97.69	97.73
Number of cations per 6 oxygens						
Si	2.04	2.04	2.05	2.03	2.04	2.04
Al iv	-0.04	-0.04	-0.05	-0.03	-0.04	-0.04
Al vi	0.07	0.06	0.08	0.07	0.06	0.07
Fe iii	0.00	0.00	0.00	0.00	0.00	0.00
Cr	0.00	0.00	0.00	0.00	0.00	0.00
Ti	0.00	0.00	0.00	0.00	0.00	0.00
Fe ii	0.24	0.23	0.23	0.24	0.20	0.22
Mn	0.01	0.00	0.00	0.00	0.01	0.00
Mg	0.80	0.81	0.79	0.80	0.82	0.81
Ca	0.82	0.82	0.81	0.81	0.84	0.81
Na	0.04	0.04	0.04	0.05	0.04	0.05
K	0.00	0.00	0.00	0.00	0.00	0.00
TOTAL	3.97	3.97	3.96	3.98	3.97	3.97
Wo	43.97	43.86	44.00	43.79	44.99	44.05
En	42.94	43.38	43.24	43.30	43.70	43.80
Fs	13.10	12.75	12.76	12.91	11.31	12.16

wt%	PHL1	PHL2	PHL3	PHL4	PHL5	PHL6	PHL7	PHL8	PHL9
SiO2	39.88	38.76	39.92	39.54	38.97	37.87	39.74	39.95	39.68
Al2O3	13.15	13.54	13.60	12.74	13.13	12.11	12.50	12.97	12.15
FeO	7.43	7.73	7.42	10.01	10.28	10.41	10.05	8.96	8.79
Cr2O3	0.10	0.15	0.02	0.01	0.00	0.00	0.00	0.00	0.00
TiO2	1.30	1.43	1.70	1.89	1.97	2.12	2.10	1.96	1.73
NiO	0.29	0.31	0.29	0.42	0.19	0.27	0.34	0.30	0.23
MnO	0.00	0.00	0.00	0.03	0.09	0.00	0.01	0.12	0.00
MgO	20.38	20.27	20.99	18.94	19.17	18.40	19.39	20.28	20.80
CaO	0.01	0.01	0.00	0.02	0.00	0.03	0.02	0.02	0.02
Na2O	0.40	0.39	0.34	0.22	0.31	0.17	0.28	0.18	0.11
K2O	8.67	9.12	9.15	9.16	8.88	8.95	8.80	8.99	9.24
Cl	0.74	0.75	0.75	0.98	0.99	1.01	0.99	0.83	0.76
F	2.27	1.98	2.29	1.85	1.74	1.30	1.94	2.05	2.14
V2O3	0.09	0.05	0.04	0.06	0.00	0.13	0.03	0.02	0.00
Total	93.60	93.47	95.37	94.86	94.77	91.99	95.13	95.57	94.58
Number of cations per 24 (O, F, Cl, OH)									
Si	5.93	5.80	5.84	5.90	5.81	5.84	5.90	5.87	5.90
Al iv	2.07	2.20	2.16	2.10	2.19	2.16	2.10	2.13	2.10
Al vi	0.24	0.19	0.19	0.14	0.12	0.05	0.09	0.11	0.03
Cr	0.01	0.02	0.00	0.00	0.00	0.00	0.00	0.00	0.00
Ti	0.15	0.16	0.19	0.21	0.22	0.25	0.23	0.22	0.19
Fe	0.92	0.97	0.91	1.25	1.28	1.34	1.25	1.10	1.09
Mn	0.00	0.00	0.00	0.00	0.01	0.00	0.00	0.01	0.00
Mg	4.52	4.52	4.58	4.21	4.26	4.23	4.29	4.44	4.61
Ca	0.00	0.00	0.00	0.00	0.00	0.00	0.00	0.00	0.00
Na	0.12	0.11	0.10	0.06	0.09	0.05	0.08	0.05	0.03
K	1.65	1.74	1.71	1.74	1.69	1.76	1.67	1.68	1.75
Cl	0.19	0.19	0.19	0.25	0.25	0.26	0.25	0.21	0.19
F	1.07	0.94	1.06	0.87	0.82	0.64	0.91	0.95	1.01
OH*	2.74	2.87	2.75	2.88	2.93	3.10	2.84	2.84	2.80
TOTAL	19.64	19.76	19.70	19.67	19.70	19.71	19.65	19.66	19.74
Al total	2.31	2.39	2.35	2.24	2.31	2.20	2.19	2.25	2.13
Fe/Fe+Mg	0.17	0.18	0.17	0.23	0.23	0.24	0.23	0.20	0.19

wt%	APT1	APT2	APT3	APT4	APT5	APT6	APT7	APT8	APT9
P2O5	42.63	41.40	42.61	43.43	41.84	43.29	42.60	42.72	42.19
SiO2	0.05	0.03	0.63	0.13	0.06	0.13	0.02	0.08	0.09
Al2O3	0.01	0.02	0.02	0.01	0.00	0.02	0.03	0.00	0.00
FeO	0.00	0.00	0.15	0.00	0.02	0.07	0.02	0.14	0.14
Cr2O3	0.04	0.10	0.06	0.00	0.00	0.00	0.00	0.00	0.00
TiO2	0.00	0.00	0.00	0.23	0.13	0.00	0.11	0.00	0.01
NiO	0.01	0.00	0.09	0.08	0.05	0.02	0.01	0.06	0.04
MnO	0.00	0.06	0.05	0.01	0.00	0.04	0.03	0.13	0.10
MgO	0.03	0.01	0.29	0.03	0.00	0.00	0.00	0.00	0.03
CaO	53.28	51.75	53.01	52.67	52.57	51.71	53.16	50.27	50.86
Na2O	0.02	0.05	0.07	0.04	0.08	0.08	0.07	0.07	0.09
K2O	0.01	0.00	0.00	0.00	0.00	0.00	0.03	0.00	0.03
Cl	1.24	6.67	2.11	1.11	6.66	5.57	1.68	5.54	6.03
F	0.00	0.01	0.02	0.02	0.05	0.09	0.10	0.13	0.23
SO3	0.04	0.00	0.08	0.13	0.04	0.06	0.10	0.01	0.04
V2O3	0.03	0.06	0.00	0.03	0.00	0.00	0.00	0.03	0.04
Total	97.10	98.64	98.69	97.65	99.99	99.78	97.52	97.88	98.46

Number of cations per 26 (O, Cl, F, OH)

P	6.12	6.12	6.06	6.17	6.09	6.21	6.11	6.25	6.19
Si	0.01	0.00	0.11	0.02	0.01	0.02	0.00	0.01	0.02
Al	0.00	0.00	0.00	0.00	0.00	0.00	0.00	0.00	0.00
Ti	0.00	0.00	0.00	0.03	0.02	0.00	0.01	0.00	0.00
Fe	0.00	0.00	0.02	0.00	0.00	0.01	0.00	0.02	0.02
Mn	0.00	0.01	0.01	0.00	0.00	0.01	0.00	0.02	0.01
Mg	0.01	0.00	0.07	0.01	0.00	0.00	0.00	0.00	0.01
Ca	9.68	9.67	9.53	9.46	9.69	9.39	9.65	9.30	9.44
Na	0.01	0.02	0.02	0.01	0.03	0.03	0.02	0.02	0.03
K	0.00	0.00	0.00	0.00	0.00	0.00	0.01	0.00	0.01
Cl	0.35	1.97	0.60	0.32	1.94	1.60	0.48	1.62	1.77
F	0.00	0.00	0.00	0.01	0.01	0.02	0.03	0.03	0.06
OH*	1.65	0.02	1.39	1.68	0.04	0.38	1.49	0.34	0.17
TOTAL	17.82	17.83	17.82	17.71	17.84	17.67	17.82	17.63	17.72

wt%	APT10	APT11	APT12	APT13	APT14	APT15	APT16	APT17	APT18
P2O5	43.62	43.44	42.77	43.17	42.80	42.79	42.94	42.87	42.38
SiO2	0.08	0.08	0.04	0.08	0.15	0.11	0.02	0.15	0.04
Al2O3	0.03	0.04	0.00	0.00	0.01	0.01	0.03	0.00	0.00
FeO	0.14	0.03	0.00	0.13	0.05	0.05	0.00	0.15	0.00
Cr2O3	0.00	0.00	0.00	0.06	0.05	0.00	0.05	0.00	0.00
TiO2	0.07	0.01	0.00	0.15	0.00	0.00	0.00	0.00	0.00
NiO	0.06	0.05	0.02	0.00	0.05	0.00	0.00	0.02	0.00
MnO	0.09	0.00	0.00	0.01	0.02	0.00	0.07	0.04	0.00
MgO	0.01	0.00	0.00	0.00	0.03	0.01	0.01	0.01	0.03
CaO	52.65	52.72	53.24	52.66	51.30	50.95	54.14	51.24	53.29
Na2O	0.07	0.03	0.03	0.03	0.08	0.09	0.03	0.10	0.06
K2O	0.02	0.00	0.00	0.01	0.00	0.00	0.02	0.00	0.00
Cl	1.06	1.10	2.11	1.82	6.05	6.37	0.28	4.09	1.17
F	0.25	0.27	0.00	0.27	0.29	0.31	0.33	0.51	0.84
SO3	0.08	0.04	0.04	0.02	0.07	0.10	0.03	0.05	0.05
V2O3	0.03	0.00	0.01	0.01	0.00	0.07	0.00	0.00	0.00
Total	97.89	97.44	97.78	97.89	99.46	99.29	97.73	98.08	97.23

Number of cations per 26 (O, Cl, F, OH)

P	6.18	6.18	6.13	6.16	6.20	6.22	6.10	6.21	6.10
Si	0.01	0.01	0.01	0.01	0.02	0.02	0.00	0.02	0.01
Al	0.00	0.00	0.00	0.00	0.00	0.00	0.00	0.00	0.00
Ti	0.01	0.00	0.00	0.02	0.00	0.00	0.00	0.00	0.00
Fe	0.02	0.00	0.00	0.02	0.01	0.01	0.00	0.02	0.00
Mn	0.01	0.00	0.00	0.00	0.00	0.00	0.01	0.01	0.00
Mg	0.00	0.00	0.00	0.00	0.01	0.00	0.00	0.00	0.01
Ca	9.45	9.50	9.66	9.51	9.41	9.38	9.73	9.39	9.71
Na	0.02	0.01	0.01	0.01	0.03	0.03	0.01	0.03	0.02
K	0.00	0.00	0.00	0.00	0.00	0.00	0.00	0.00	0.00
Cl	0.30	0.31	0.61	0.52	1.75	1.85	0.08	1.18	0.34
F	0.06	0.07	0.00	0.07	0.08	0.08	0.08	0.13	0.22
OH*	1.63	1.62	1.39	1.41	0.17	0.06	1.83	0.68	1.45
TOTAL	17.71	17.71	17.80	17.73	17.68	17.66	17.85	17.68	17.85

wt%	APT19	APT20	APT21	APT22	APT23	APT24	APT25	APT26	APT27
P2O5	42.04	43.18	42.29	42.15	41.00	42.76	40.17	43.59	41.63
SiO2	0.01	0.04	0.01	0.06	0.17	0.04	0.11	0.05	0.04
Al2O3	0.02	0.00	0.00	0.00	0.00	0.00	0.00	0.00	0.00
FeO	0.02	0.05	0.04	0.00	0.02	0.18	0.00	0.20	0.05
Cr2O3	0.07	0.00	0.00	0.00	0.04	0.00	0.00	0.00	0.02
TiO2	0.29	0.00	0.00	0.00	0.00	0.03	0.01	0.00	0.27
NiO	0.05	0.00	0.06	0.11	0.00	0.01	0.00	0.03	0.00
MnO	0.00	0.00	0.08	0.00	0.12	0.04	0.00	0.00	0.02
MgO	0.01	0.00	0.00	0.01	0.10	0.00	0.00	0.03	0.04
CaO	53.48	54.65	54.46	53.88	52.07	53.10	54.99	52.41	52.75
Na2O	0.05	0.05	0.08	0.02	0.14	0.06	0.02	0.05	0.12
K2O	0.02	0.01	0.00	0.02	0.01	0.00	0.02	0.02	0.02
Cl	1.48	1.07	0.88	0.88	5.92	2.24	0.32	1.93	6.72
F	1.06	1.15	1.32	1.38	0.00	2.46	2.63	3.02	0.00
SO3	0.05	0.00	0.00	0.03	0.05	0.01	0.00	0.00	0.01
V2O3	0.02	0.07	0.04	0.00	0.00	0.00	0.01	0.00	0.00
Total	97.89	99.53	98.52	97.76	98.29	99.38	97.10	99.63	100.17

Number of cations per 26 (O, Cl, F, OH)

P	6.06	6.09	6.05	6.06	6.05	6.12	5.90	6.20	6.06
Si	0.00	0.01	0.00	0.01	0.03	0.01	0.02	0.01	0.01
Al	0.00	0.00	0.00	0.00	0.00	0.00	0.00	0.00	0.00
Ti	0.04	0.00	0.00	0.00	0.00	0.00	0.00	0.00	0.04
Fe	0.00	0.01	0.01	0.00	0.00	0.03	0.00	0.03	0.01
Mn	0.00	0.00	0.01	0.00	0.02	0.01	0.00	0.00	0.00
Mg	0.00	0.00	0.00	0.00	0.03	0.00	0.00	0.01	0.01
Ca	9.75	9.75	9.85	9.81	9.73	9.63	10.21	9.43	9.72
Na	0.02	0.01	0.03	0.01	0.05	0.02	0.01	0.02	0.04
K	0.00	0.00	0.00	0.00	0.00	0.00	0.00	0.01	0.00
Cl	0.43	0.30	0.25	0.25	1.75	0.64	0.09	0.55	1.96
F	0.28	0.29	0.34	0.36	0.00	0.63	0.70	0.77	0.00
OH*	1.30	1.41	1.41	1.39	0.25	0.72	1.21	0.68	0.04
TOTAL	17.88	17.87	17.94	17.90	17.91	17.81	18.14	17.70	17.89

wt%	APT28	APT29	APT30	APT31	APT32
P2O5	40.99	41.82	41.68	41.22	41.43
SiO2	0.05	0.07	0.04	0.03	0.03
Al2O3	0.00	0.00	0.00	0.00	0.00
FeO	0.00	0.07	0.05	0.01	0.12
Cr2O3	0.07	0.00	0.00	0.12	0.05
TiO2	0.16	0.00	0.12	0.04	0.12
NiO	0.00	0.04	0.08	0.00	0.00
MnO	0.02	0.00	0.00	0.12	0.00
MgO	0.02	0.04	0.05	0.00	0.04
CaO	51.52	51.44	51.10	51.56	51.86
Na2O	0.09	0.04	0.03	0.05	0.06
K2O	0.01	0.02	0.00	0.00	0.00
Cl	6.74	6.84	6.84	6.84	6.94
F	0.00	0.00	0.00	0.00	0.00
SO3	0.00	0.06	0.00	0.00	0.00
V2O3	0.02	0.04	0.00	0.05	0.01
Total	98.17	98.91	98.44	98.49	99.07

Number of cations per 26 (O, Cl, F, OH)

P	6.09	6.15	6.15	6.11	6.10
Si	0.01	0.01	0.01	0.00	0.01
Al	0.00	0.00	0.00	0.00	0.00
Ti	0.02	0.00	0.02	0.01	0.02
Fe	0.00	0.01	0.01	0.00	0.02
Mn	0.00	0.00	0.00	0.02	0.00
Mg	0.00	0.01	0.01	0.00	0.01
Ca	9.69	9.57	9.55	9.67	9.67
Na	0.03	0.01	0.01	0.02	0.02
K	0.00	0.00	0.00	0.00	0.00
Cl	2.01	2.01	2.02	2.03	2.05
F	0.00	0.00	0.00	0.00	0.00
OH*	0.00	0.00	0.00	0.00	0.00
TOTAL	17.86	17.78	17.77	17.86	17.88

wt%	Mgt 1	Mgt 2	Mgt 3	Mgt 4	Mgt 5	Mgt 6	Mgt 7	Mgt 8	Mgt 9
SiO2	0.21	0.02	0.19	0.38	1.98	0.22	0.02	0.97	0.69
Al2O3	0.27	0.06	0.23	0.11	0.03	0.09	0.04	0.00	0.00
FeO	90.81	91.26	89.83	92.46	90.07	91.43	92.66	89.50	90.77
Cr2O3	0.43	0.35	0.22	0.14	0.06	0.04	0.03	0.02	0.00
TiO2	0.00	0.00	0.10	0.15	0.14	0.00	0.00	0.07	0.10
NiO	0.24	0.31	0.35	0.28	0.00	0.03	0.05	0.00	0.00
MnO	0.00	0.04	0.00	0.06	0.01	0.08	0.10	0.00	0.01
MgO	0.16	0.04	0.09	0.14	0.27	0.05	0.02	0.00	0.00
CaO	0.01	0.02	0.06	0.10	0.12	0.04	0.03	0.00	0.01
K2O	0.05	0.00	0.05	0.00	0.00	0.01	0.01	0.00	0.00
Cl	0.01	0.00	0.00	0.01	0.02	0.00	0.01	0.02	0.00
F	0.26	0.30	0.26	0.31	0.26	0.18	0.32	0.29	0.31
SO3	0.00	0.00	0.06	0.09	0.05	0.00	0.00	0.00	0.00
V2O3	0.44	0.20	0.29	0.05	0.01	0.02	0.01	0.01	0.00
Total	92.82	92.47	91.67	94.14	92.90	92.18	93.15	90.76	91.77

wt%	Mgt 10	Mgt 11	Mgt 12	Mgt 13
SiO2	0.07	1.88	1.33	0.37
Al2O3	0.08	0.02	0.03	0.16
FeO	90.81	90.97	91.06	92.10
Cr2O3	0.00	0.00	0.00	0.00
TiO2	0.00	0.00	0.01	0.00
NiO	0.11	0.09	0.08	0.23
MnO	0.00	0.08	0.00	0.08
MgO	0.00	0.03	0.05	0.13
CaO	0.04	0.09	0.08	0.09
K2O	0.03	0.01	0.03	0.00
Cl	0.00	0.03	0.00	0.00
F	0.27	0.27	0.25	0.28
SO3	0.02	0.00	0.00	0.00
V2O3	0.06	0.00	0.01	0.05
Total	91.36	93.34	92.82	93.42

ANEXO II– supplementary U-Pb analyses.

Sample/ spot #	[U] ppm	[Th] ppm	[Pb] ppm	Th/U meas	²⁰⁶Pb/²⁰⁴Pb measured	f₂₀₆%	²⁰⁷Pb ²³⁵U
n5814_(3A)_z1c	309.8	329.1	285.5	1.06	40430	0.05	19.17872
n5814_(3A)_z1r	307.3	77.8	204.7	0.25	22077	0.08	14.13745
n5814_(3A)_z2r	360.4	278.9	282.3	0.77	29284	0.06	15.15861
n5814_(3A)_z2c	697.7	369.6	423.1	0.53	27448	0.07	12.07761
n5814_(3A)_z3r	304.2	77.0	204.4	0.25	69312	0.03	14.05750
n5814_(3A)_z4c	2217.5	3793.3	1447.1	1.71	12876	0.15	10.21230
n5814_(3A)_z5c	553.2	237.4	390.0	0.43	17729	0.11	14.75552
n5814_(3A)_z6c	257.7	180.5	190.3	0.70	6249	0.30	15.83758
n5814_(3A)_z6r	350.4	112.4	239.8	0.32	21398	0.09	14.48609
n5814_(3A)_z7c	11655.9	62203.4	4594.8	5.34	1198	1.56	2.93771
n5814_(3A)_z7r	400.8	114.3	282.5	0.29	93054	0.02	15.21905
n5814_(3A)_z8c	750.2	308.3	388.7	0.41	14548	0.13	10.21323
n5814_(3A)_z9c	796.9	361.2	387.1	0.45	8177	0.23	9.52027
n5814_(3A)_z9r	4261.6	3347.7	1440.8	0.79	3939	0.47	5.20426
n5814_(3A)_z10c	637.3	399.0	470.4	0.63	64444	0.03	14.85358
n5814_(3A)_z10r	475.4	223.5	350.5	0.47	53122	0.04	15.22643
n5814_(3A)_z11c	670.4	1934.6	427.1	2.89	7625	0.25	8.00295
n5814_(3A)_z11r	1306.1	714.0	494.9	0.55	10530	0.18	6.60164
n5814_(3A)_z12c	539.4	106.4	316.7	0.20	25104	0.07	13.37922
n5814_(3A)_z12r	378.4	131.1	271.8	0.35	26936	0.07	15.22045
n5815_(11B)_z1c	613.0	419.6	212.0	0.68	22838	0.08	6.17332
n5815_(11B)_z1r	377.7	323.4	202.8	0.86	34660	0.05	9.93035
n5815_(11B)_z2c	1023.8	7249.2	316.3	7.08	2078	0.90	4.47278
n5815_(11B)_z2r	583.4	808.0	332.4	1.38	26237	0.07	8.44618
n5815_(11B)_z3r	1273.2	949.8	299.3	0.75	13595	0.14	3.29662
n5815_(11B)_z3c	530.5	1041.8	402.7	1.96	33747	0.06	10.50916
n5815_(11B)_z4r	557.6	675.6	307.1	1.21	26679	0.07	9.17460
n5815_(11B)_z4c	414.9	441.2	316.0	1.06	52067	0.04	13.20387
n5815_(11B)_z5r	453.9	336.5	228.0	0.74	49536	0.04	9.01234
n5815_(11B)_z6r	289.3	132.5	149.4	0.46	26897	0.07	9.85786
n5815_(11B)_z6c	207.8	235.2	142.4	1.13	29667	0.06	11.35523
n5815_(11B)_z7c	78.6	37.3	54.1	0.47	19945	0.09	13.53831
n5815_(11B)_z7r	542.6	255.9	182.1	0.47	5645	0.33	5.86184
n5815_(11B)_z8r	1032.4	880.7	308.3	0.85	15178	0.12	4.60418
n5815_(11B)_z8c	443.8	701.9	300.8	1.58	20055	0.09	9.79068
n5815_(11B)_z9c	717.9	336.1	216.2	0.47	10707	0.17	5.19082
n5815_(11B)_z9r	227.1	106.1	77.1	0.47	9376	0.20	6.35404
n5815_(11B)_z10r	156.9	65.8	109.1	0.42	37168	0.05	13.70795
n5815_(11B)_z10c	353.7	450.9	228.7	1.27	29686	0.06	10.30401
n5815_(11B)_z11r	179.6	164.1	116.8	0.91	30908	0.06	11.61718
n5815_(11B)_z11c	148.2	119.7	110.1	0.81	81269	0.02	13.53210

$\pm\sigma$ %	^{206}Pb ^{238}U	$\pm\sigma$ %	ρ	^{208}Pb ^{232}Th	$\pm\sigma$ %	^{207}Pb ^{206}Pb	$\pm\sigma$	^{207}Pb ^{235}U
1.58	0.60303	1.52283	0.96	0.168846	3.1	3056.7	7.0	3050.8
0.92	0.52573	0.87537	0.95	0.149654	2.5	2785.1	4.7	2759.0
0.92	0.54774	0.87572	0.96	0.162347	2.4	2832.0	4.4	2825.3
0.89	0.45190	0.84137	0.95	0.126208	2.4	2775.0	4.6	2610.5
0.94	0.53364	0.88103	0.94	0.144222	2.6	2751.3	5.3	2753.6
1.04	0.39226	1.00243	0.97	0.108879	2.4	2731.9	4.4	2454.2
1.72	0.52943	1.70081	0.99	0.159603	3.6	2843.5	4.5	2799.6
1.41	0.52805	1.38161	0.98	0.136619	2.7	2962.5	4.7	2867.0
0.93	0.53119	0.86899	0.94	0.150035	2.5	2808.0	5.2	2782.1
7.82	0.20373	6.64967	0.85	0.031701	19.8	1707.0	75.8	1391.7
0.91	0.54954	0.87601	0.97	0.157700	2.4	2833.2	3.8	2829.0
2.58	0.40087	2.43864	0.94	0.105193	10.9	2696.2	14.0	2454.3
3.86	0.37419	3.67659	0.95	0.093729	8.2	2694.0	19.7	2389.5
2.15	0.24092	1.97024	0.92	0.075655	3.4	2420.0	14.5	1853.3
0.89	0.53541	0.85837	0.97	0.151793	2.7	2836.0	3.6	2805.9
0.85	0.55341	0.82782	0.97	0.156101	2.4	2822.5	3.5	2829.5
3.72	0.32755	3.54459	0.95	0.087150	4.6	2626.8	19.0	2231.4
4.27	0.28765	3.97529	0.93	0.079387	4.7	2522.3	26.1	2059.6
0.93	0.46438	0.87370	0.94	0.129980	2.8	2897.5	5.0	2706.8
0.96	0.55527	0.85947	0.90	0.152328	2.5	2816.4	6.8	2829.1
4.83	0.25179	4.82299	1.00	0.071931	6.1	2632.6	4.9	2000.7
1.24	0.39396	1.19972	0.97	0.082795	2.7	2678.6	5.2	2428.3
3.20	0.20777	2.98327	0.93	0.009708	18.1	2414.2	19.8	1725.9
0.96	0.35038	0.88709	0.93	0.114133	3.0	2604.4	6.1	2280.2
1.21	0.17046	1.15440	0.95	0.054550	2.6	2230.5	6.3	1480.3
0.98	0.40934	0.95020	0.97	0.139261	2.4	2708.9	4.0	2480.7
1.67	0.36264	1.65171	0.99	0.100390	11.0	2684.6	4.2	2355.6
1.55	0.50764	1.51844	0.98	0.148800	2.7	2730.4	5.1	2694.3
1.92	0.35911	1.89967	0.99	0.104968	3.2	2671.3	4.7	2339.3
1.74	0.38906	1.71040	0.98	0.121496	3.7	2687.2	5.5	2421.6
1.44	0.44189	1.38675	0.96	0.142182	2.9	2710.4	6.2	2552.8
1.26	0.52449	1.12461	0.89	0.139788	2.8	2717.8	9.5	2718.0
1.58	0.25370	1.51545	0.96	0.083431	3.0	2533.6	7.6	1955.6
2.71	0.20651	2.56191	0.95	0.068864	3.4	2473.5	14.7	1750.0
1.14	0.37986	1.10650	0.97	0.143500	3.3	2715.4	4.5	2415.3
5.95	0.21584	5.91140	0.99	0.101916	9.5	2600.5	11.3	1851.1
1.44	0.25150	1.35669	0.94	0.089480	3.0	2682.4	7.8	2025.9
1.02	0.52811	0.91327	0.90	0.162114	3.3	2727.0	7.5	2729.7
1.18	0.39989	1.13632	0.96	0.134991	2.6	2714.9	5.2	2462.5
1.11	0.44460	1.04100	0.94	0.132813	2.6	2737.9	6.4	2574.1
1.18	0.52260	1.10534	0.94	0.151498	2.8	2723.0	6.6	2717.5

$\pm\sigma$	^{206}Pb ^{238}U	$\pm\sigma$	^{208}Pb ^{232}Th	$\pm\sigma$
15.4	3042.0	37.0	3153.4	90.1
8.8	2723.4	19.5	2818.8	65.6
8.8	2815.8	20.0	3040.8	68.9
8.4	2403.7	16.9	2402.3	54.8
8.9	2756.8	19.8	2723.1	64.9
9.6	2133.3	18.2	2088.9	47.9
16.5	2739.1	38.1	2993.0	101.3
13.6	2733.2	30.9	2588.3	65.9
8.8	2746.5	19.5	2825.5	66.0
61.0	1195.3	73.0	630.8	122.4
8.7	2823.2	20.1	2959.8	66.9
24.2	2173.1	45.1	2021.6	208.1
36.1	2049.1	64.9	1810.9	142.3
18.5	1391.5	24.7	1474.1	47.7
8.5	2764.2	19.3	2856.4	72.4
8.2	2839.3	19.0	2931.9	65.4
34.2	1826.5	56.6	1688.9	74.3
38.3	1629.8	57.5	1544.1	69.9
8.8	2458.9	17.9	2469.9	63.9
9.2	2847.1	19.8	2865.8	66.0
43.1	1447.7	62.8	1404.0	82.3
11.5	2141.2	21.9	1607.8	41.8
26.9	1216.9	33.2	195.3	35.1
8.7	1936.4	14.9	2184.5	63.0
9.5	1014.6	10.8	1073.6	27.5
9.1	2211.9	17.8	2635.3	59.3
15.4	1994.7	28.4	1933.6	201.1
14.7	2646.6	33.0	2803.8	71.5
17.7	1978.0	32.4	2017.5	61.8
16.2	2118.5	31.0	2317.6	81.9
13.5	2359.1	27.5	2687.0	71.7
12.0	2718.2	25.0	2644.6	70.2
13.8	1457.5	19.8	1619.7	47.3
22.8	1210.2	28.3	1346.1	44.3
10.6	2075.6	19.7	2710.3	84.5
52.0	1259.9	68.0	1961.6	176.9
12.7	1446.2	17.6	1732.2	49.6
9.7	2733.5	20.4	3036.7	91.5
11.0	2168.5	21.0	2559.4	61.8
10.4	2371.2	20.7	2520.5	60.6
11.2	2710.2	24.5	2851.2	75.2